University of Alberta

Library Release Form

Name of Author: Xun Qi

Title of Thesis: Simulation and Laboratory Measurements of Velocity and Attenuation in Viscoelastic Body: A Frequency Dependent Study with Respect to Viscosities

Degree: Master of Science

Year this Degree Granted: 2008

_____

Signature

University of Alberta

Simulation and Laboratory Measurements of Velocity and Attenuation in Viscoelastic Body: A Frequency Dependent Study with Respect to Viscosities

by

Xun Qi

A thesis submitted to the Faculty of Graduate Studies and Research
in partial fulfillment of the requirements for the degree of

Master of Science
in
Geophysics

Department of Physics

Edmonton, Alberta
Spring 2008

University of Alberta

Faculty of Graduate Studies and Research

The undersigned certify that they have read, and recommend to the Faculty of Graduate Studies and Research for acceptance, a thesis entitled **Simulation and Laboratory Measurements of Velocity and Attenuation in Viscoelastic Body: A frequency dependent study with respect to viscosities** submitted by **Xun Qi** in partial fulfillment of the requirements for the degree of **Master of Science**.

_____

Dr. D. R. Schmitt (Supervisor)

_____

Dr. J. R. Beamish

_____

Dr. V. A. Kravchinsky

_____

Dr. T. G. Joseph

Date:

In memory of my 4-year old hard drive that appears dead two days before the defense.

One learns no matter what ways he is travelling on, university among them.

One consolatory essence among those devastating ones of time passed by lies in the removal of the barriers between man and the sunshine.

Abstract

Attenuation in the upper crust is a complex problem and a full understanding of intrinsic attenuation remains problematic, particularly in earth materials that are saturated with highly viscous liquids such as magma or bitumen. In literature, attenuation mechanisms have focused primarily on fluid displacements. Less emphasis has been placed on the potential absorption within the fluids themselves.

To gain insight into what might be expected in observation, first presented here are reviews of deformation behaviors, theories of elasticity, viscoelasticity and wave propagation, concepts and mechanisms of seismic attenuation / dispersion, laboratory techniques and previous measurements. Focus is put on the dynamic behaviors of waves in bulk viscosity incorporated viscoelastic models via relaxation theory.

Frequency dependent simulations were performed to seismic attenuation and viscoelastic models with focus on the effects of both shear and bulk viscosities on the P and S wave velocities and attenuation.

Optimized ultrasonic techniques were employed to measure oil sand and sandstone samples. In particular, a specialized apparatus that allows length change monitoring on weakly consolidated samples is developed. Both longitudinal and shear wave speeds were measured and the pressure dependency of velocities is discussed in the end.

This work closes with conclusions from both the simulation and the laboratory as well as recommendations for future research. However, the study of properties and characteristics of highly viscous liquids saturated materials is an ongoing topic that requires continuous endeavors.

Acknowledgements

First, I want to thank Douglas Schmitt for his supervision.

Secondly, I would also like to thank Tiewei He, Len Tober, Tony Walford and other workshop staff for their technical assistance and guidance in the lab.

This work was funded by National Science and Engineering Research Council (NSERC) of Canada through Dr. Schmitt's Discovery grant and with industrially leveraged funding obtained from the NSERC Collaborative Research and Development grant to the Consortium of Heavy Oil Research by University Scientists (CHORUS) at the University of Calgary. The work of Joan Embleton and Matthew Fay in obtaining samples for this project is greatly appreciated.

Table of Contents

List of Figures

List of Tables

Nomenclature

σ_P	the proportional limit
σ_Y	the elastic limit or yield stress
σ_S	permanent strain
σ_u	ultimate strength
σ_f	the stress at fracture
$\sigma_1 - \sigma_3$	deviatoric stress
σ_3'	effective confining pressure
$\overline{D}$	the ratio of deviatoric stress to its value at failure
A(x,t)	amplitude of a mechanical wave
ω	the angular frequency
α	the attenuation coefficient or crack aspect ratio
A_0	the initial amplitude
x	distance from the origin
k', k_r	the real part of the wavenumber
k*	complex wavenumber
E	energy stored
ΔE	energy dissipated
Q	quality factor
V, c, c_p	Phase velocity
Mr	the real part of modulus
Mi	the imaginary part
ϕ	phase angle or porosity
ω_c	characteristic frequency

η	shear viscosity (first coefficient of viscosity)
k	permeability
ρ	density
K	frame (bulk) modulus
f_c	the resonant frequency
L or l	length of the sample
V_p	P wave velocity
V_s	S wave velocity
Q_P	P wave quality factor
Q_S	S wave quality factor
Zp	P wave acoustic impedance
t_p, t_s	P or S wave travel time
C_0, C_1, C_2, C_3	coefficients for position sensors
d	travel distance in the position sensors
σ_{ij}, σ_i	stress force applied on different faces of a infinitesimal cube
ε_{ij}, ε_i	dimensionless normalized strain
c_{ij}	elastic constants
λ, μ	Lamé constants
E	Young's modulus
v	Poisson's ratio
S_o	amplitude of plane wave
K, G (μ)	Bulk and shear moduli
η	dynamic shear viscosity
u_i, u_{kk}	flow velocity
$\tilde{\sigma}_{ij}$	viscosity induced stress
η^o	Second coefficient of viscosity

$\overline{p}$	mean pressure
ζ	bulk viscosity
α_λ	attenuation coefficients per wavelength
ω_v	reference frequency
$\tau\ \tau_v$	relaxation time
f(t)	time function
F(ω)	fourier transform of f(t)
f(ω)	complex function
$f_1(\omega)$	real part of f(ω)
$f_2(\omega)$	imaginary part of f(ω)
H	Representation for Hilbert transform
G^n	viscoelastic compliance
ε	strain amplitude
ε_0	the maximum strain amplitude
s	transform of $t-t'$
σ*	complex stress
ε*	complex strain
G*	complex shear modulus
η^*	complex shear viscosity
η'	the real part of complex shear viscosity
η''	the imaginary part of complex shear viscosity
G'	the storage modulus;
G"	the loss modulus;
τ_s	shear relaxation time

G_∞	reference modulus at infinite frequency
τ_v	the bulk relaxation time
K_0	the relaxed modulus when $\omega = 0$
K_∞	bulk modulus at infinite frequency.
M*	Modulus, equals K*+4/3 G*
$\alpha_{\lambda p/\lambda s}$	P or S wave attenuation coefficient per wavelength
c_∞	phase velocity at infinite frequency
ω_r	reference frequency
c_r	Phase velocity at the reference frequency ω_r
Q_r	Q at the reference frequency ω_r
γ	an empirical number
a a_2 a_3	coefficients of seismic attenuation models
τ_ε , τ_σ	relaxation time for stress and strain
β	exponential parameter
T	temperature
ζ	bulk viscosity
K_v	anelastic modulus
p	pressure
R	bulk / shear viscosity ratio, or resistance, or reflection coefficient
Δt	travel time in sample
t_1	travel time in buffers
t_2	travel time in both buffers and sample
$\Delta\phi$	phase difference from two waveforms

Δt_{phase}	phase lag time
$\mathrm{V}_{\text{phase}}$	phase velocity
$S(\omega)$	amplitude spectrum of the outgoing pulse
$D(\omega)$	amplitude response spectrum of the receiver
m_d	is dry mass of the sample
V_s	the solid matrix volume of the rock
ρ_g	grain density or skeletal density
ρ_b	bulk density
V_e	the envelope volume
φ	bulk porosity
V_p	the pore and any other void volume
D	the pore diameter
γ	the surface tension of mercury
θ	θ is the contact angle of mercury
$V_{Hg}(P)$	the cumulative volume of mercury

Chapter 1
Introduction

1.1 Motivation

Attenuation in the upper crust is a complex problem and a full understanding of intrinsic attenuation remains problematic. This is particularly true in earth materials that are saturated with highly viscous liquids such as magma or bitumen. In fluid saturated materials, attenuation mechanisms have focused primarily on global and local types of fluid displacements. That is, the mechanisms have assumed that attenuation was produced only by fluid motions relative to the solids. Less emphasis has been placed on the potential mechanism for absorption within the fluids themselves. In this thesis, we first carry out an exploration of the influence of attenuation on the evolution of elastic waves propagating through viscoelastic materials, the purpose of this is to gain some insight into what might be expected to be observed in both field and laboratory tests. As such, the evolution of elastic waveforms propagating through absorbing materials is studied. We note that no attempt is made here to derive new theoretical models that would describe the mechanism of attenuation in heavy oil saturated materials; the modeling here is to show only the evolution of the wave forms through general attenuating media in order to place some constraints on the influence of attenuation to gain better understanding of the linkages between attenuation and velocity dispersion. The second part of this work consists primarily of the description of the development of a specialized ultrasonic testing apparatus that allows one to obtain measurement at ultrasonic frequencies of both longitudinal and shear wave speeds on weakly consolidated earth materials.

1.2 Chapter Descriptions

This thesis is divided into nine chapters. Chapter 1 is motivation and this description of what it is in each chapter.

In Chapter 2, a review of deformation behaviors of materials is presented as an opening. The concepts and mechanisms of seismic attenuation and dispersion are briefly reviewed, followed by laboratory techniques and review of measurements. The knowledge gaps in the literature are then summed up in the end of this chapter.

In order to address uprising problems, basic theories of elasticity, viscoelasticity and wave propagation are reviewed in Chapter 3, with the emphasis on commonly ignored bulk viscosity. Viscoelastic models are also reviewed in the end of this chapter.

In Chapter 4, theoretical concerns on dynamic behaviors of waves are presented. The aforementioned viscoelastic models are upgraded into dynamic case with both viscosities incorporated via relaxation theory.

In Chapter 5, frequency dependent simulations are first performed with 5 seismic attenuation models and soon expanded to viscoelastic models with focus on the effects of both shear and bulk viscosities on the P and S wave velocities and attenuation.

Following Chapter 5 is the laboratory configuration and procedure that was applied to measure oil sand and sandstone samples. This chapter (Chapter 6) introduces the ultrasonic techniques that are commonly employed in the lab and modifications made to handle the problems in measuring viscoelastic materials such as oil sand.

Chapter 7 is about material characterization of these samples. It covers the geological background of the samples, SEM imaging, densities and mercury porosimetry.

Chapter 8 shows the results from ultrasonic measurements and discusses the pressure dependency of velocities as well as the length change effect.

The last chapter, Chapter 9, is a summary of what has been studied in this

work and conclusions from both the simulation and the laboratory. It closes this thesis with recommendations for future research.

Chapter 2

Previous Studies of Dispersion and Attenuation

This chapter consists of a background review discussion of seismic attenuation and dispersion. First, however, a brief review of expected material properties followed by the physical mechanisms thought to be important in influencing wave propagation in earth materials are presented.

2.1 Deformation Behaviour of Materials

In this section, the general deformation behaviour of materials is briefly reviewed in order to set the stage for a better understanding of the literature review to follow. The mathematical background that phenomenologically describes this behaviour will be presented in the next chapter.

A generalized stress-strain plot for a solid material is shown in Figure 2.1a, it is important to note that real materials can have quite different stress-strain curves and that the one shown in Figure 2a is primarily for purposes of illustration. At sufficiently low deviatoric stress levels, Hooke's law (i.e. linear elasticity) is assumed to describe material behaviour. The σ–ε curve will be a straight line (Figure 2.1a) [1] up to the *proportional limit* σ_P above which the deformation deviates from linear. This zone is the nonlinearly elastic zone in which deformation remains elastic in the sense that it is reversible. Above a certain stress level referred to as the *elastic limit* or *yield stress* σ_Y, however, the material is permanently strained ε_S and the material is said to be in the *plastic regime*. The yield stress designates the point after which, the elastic regime gives way to inelastic, which is usually the case for large amplitude strain change such as tectonic movements (Ranalli, 1987). The deformation in this domain is partially

[1] Note that we are in this contribution ignoring nonlinear elastic materials which have a whole additional range of properties that can be considered.

reversible, and the non-recovered portion depends on the loss mechanism. Continued application of stress leads to the peak stress, or *ultimate strength* σ_u after which the sample fails by fracturing. Materials that behave in this manner are said to be within the *brittle* regime.

Other materials can exhibit quite different behaviour as illustrated in Figure 2.1b. This hypothetical material also has the elastic regions but instead of deforming plastically to failure will continue to deform, or *creep*, with no additional stress. The resultant viscous flow keeps the material within the *ductile* regime. The deformation in this regime is irreversible and permanent, but still continuous. In the ductile flow regime, the response of the materials to a constant stress is creep flow, which is commonly observed on rocks and minerals with oil or brine saturation at high temperature (Nicolas, 1986).

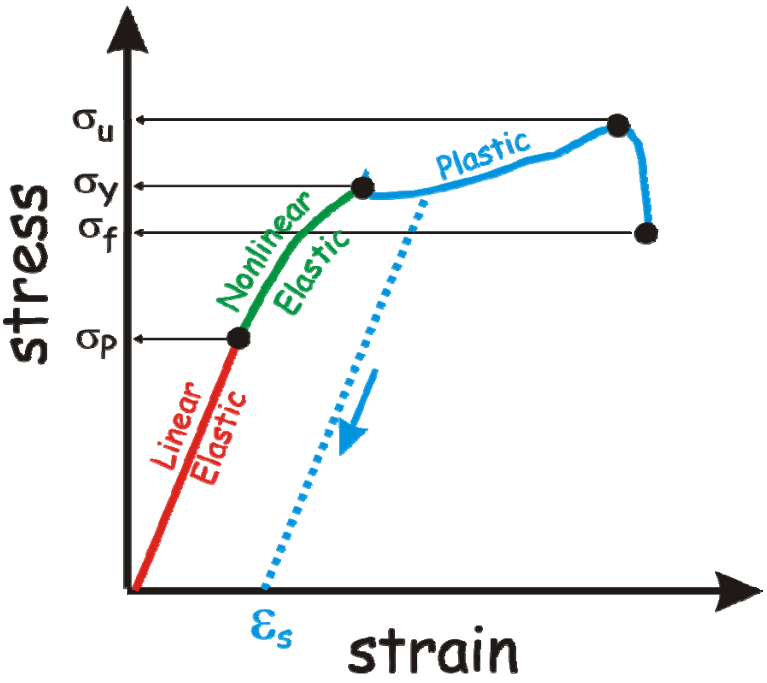

Figure 2.1a Deformation regimes of materials – from elastic to brittle

σ_P *is proportional limit*; σ_Y *is yield stress*; σ_u *is ultimate stress, and* σ_f *is the stress at fracture*

(Figure courtesy of D. Schmitt from Geophysics 332 Lecture Notes)

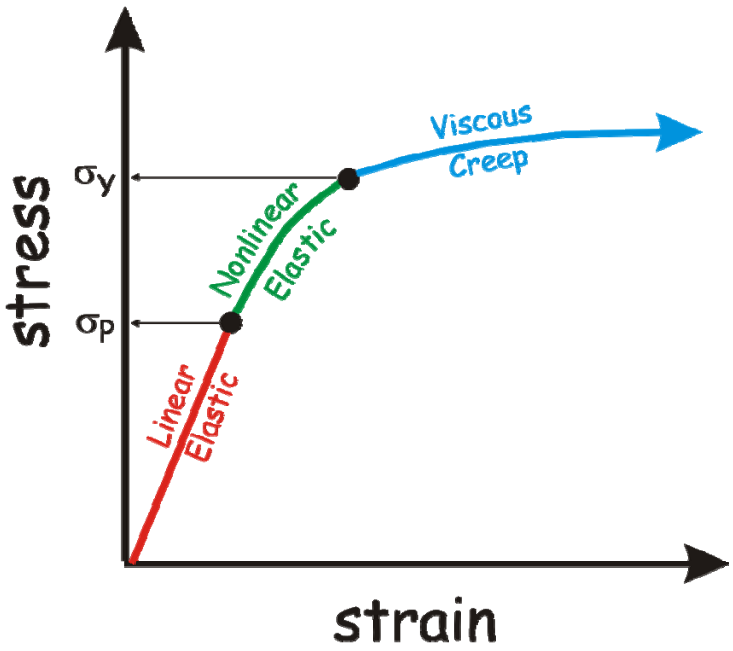

Figure 2.1b Deformation regimes of materials – from elastic to ductile
(Figure courtesy of D. Schmitt from Geophysics 332 Lecture Notes)

It is interesting to look at the behaviour of a real material to show how its deformation can be influenced by both temperature and pressure. Figure 2.2 is a classic graph of the strain versus the deviatoric compressive stress applied to a marble at a variety of increasing temperatures (Griggs et al., 1960). At room temperature (25ºC), the marble is highly brittle and fails by fracturing. At 300ºC the deformation displays clearly the linear and nonlinear elastic and the plastic regimes prior to brittle failure. At even higher temperatures the marble creeps without fracture.

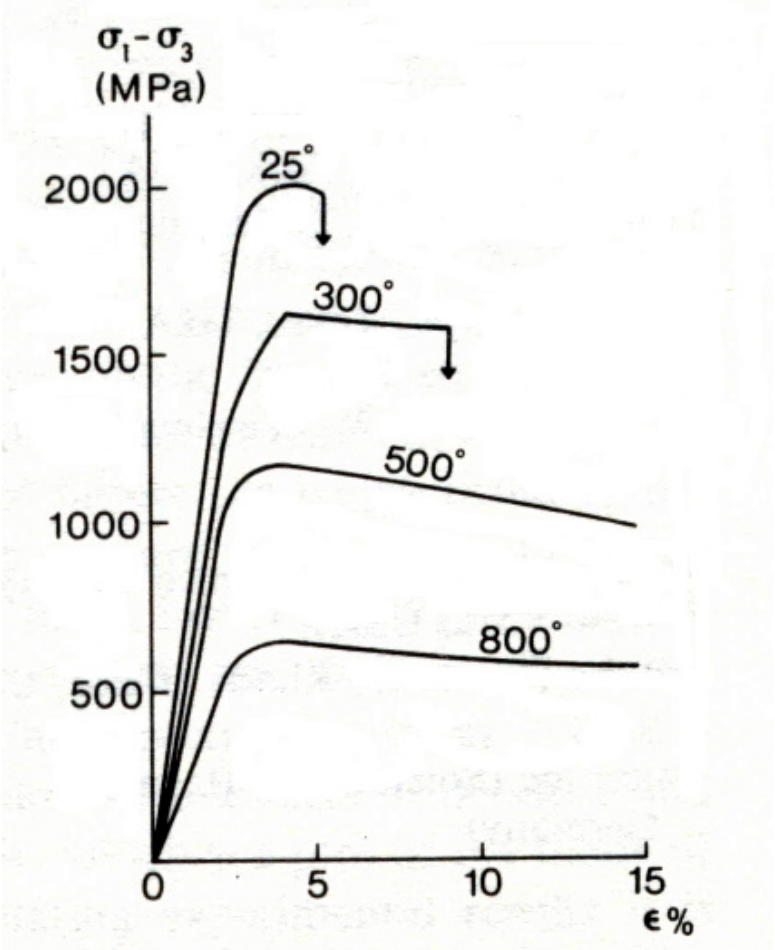

Figure 2.2 Example of deviatoric stress versus axial strain on cores of Yule marble at temperatures of 25ºC, 300ºC, 500ºC, and 800ºC. (Figure reproduced from Griggs et al. (1960) with permission of Geological Society of American Memoir).

It is also interesting to examine the behaviour of a material that primarily creeps. Figure 2.3 (Viyanant et al., 2007) shows measured stress-strain curves on recycled asphalt: a mixture of heavy hydrocarbons and rock gravel which in many ways will have some characteristics shared with natural heavy oil sands. Although there is interesting confining stress dependency to the strains, the most important observation is that the material continues to creep at all stress levels. This figure, however, conceals the additional important time-dependency of the deformation, which appears in Figure 2.4.

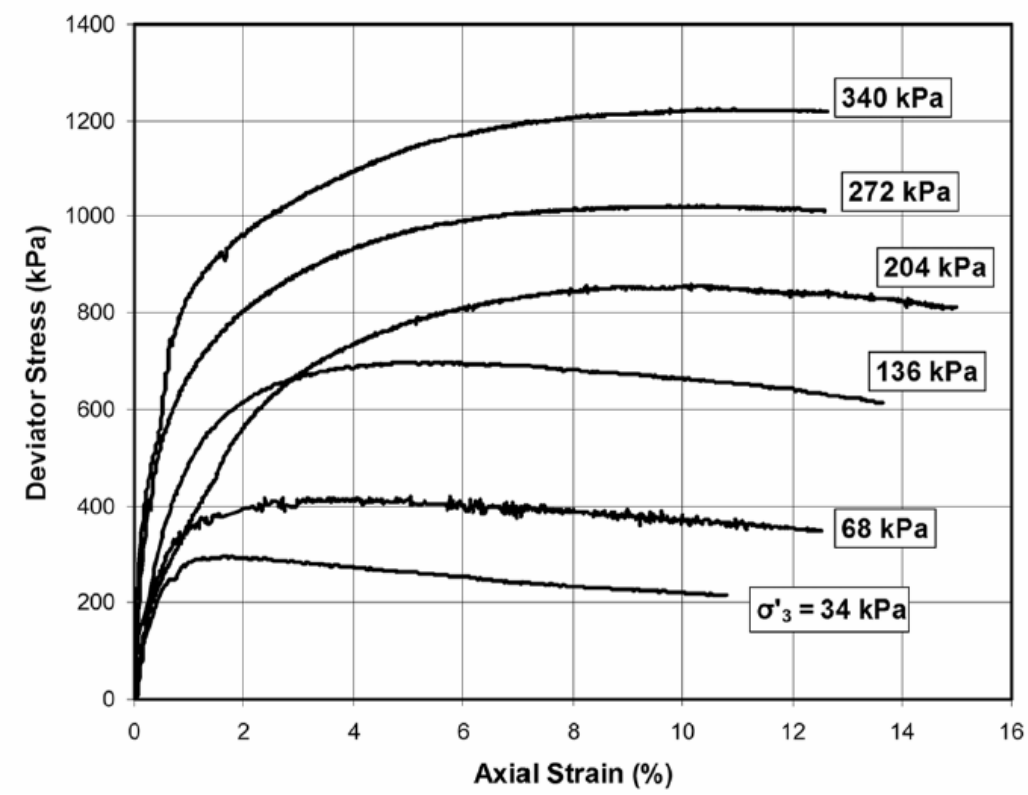

Figure 2.3 Deviatoric stress versus axial strain on recycled asphalt cylinders. The reported deviatoric stress is $\sigma_1 - \sigma_3$ (at room temperature, constant effective confining pressure σ_3' lasts at least one week or until rupture occurs). In this plot the conventions are that a positive stress is compressive and a positive strain indicates lengthening. Figure reproduced from Viyanant et al. (2007) with permission of the Canadian Geotechnical Journal.

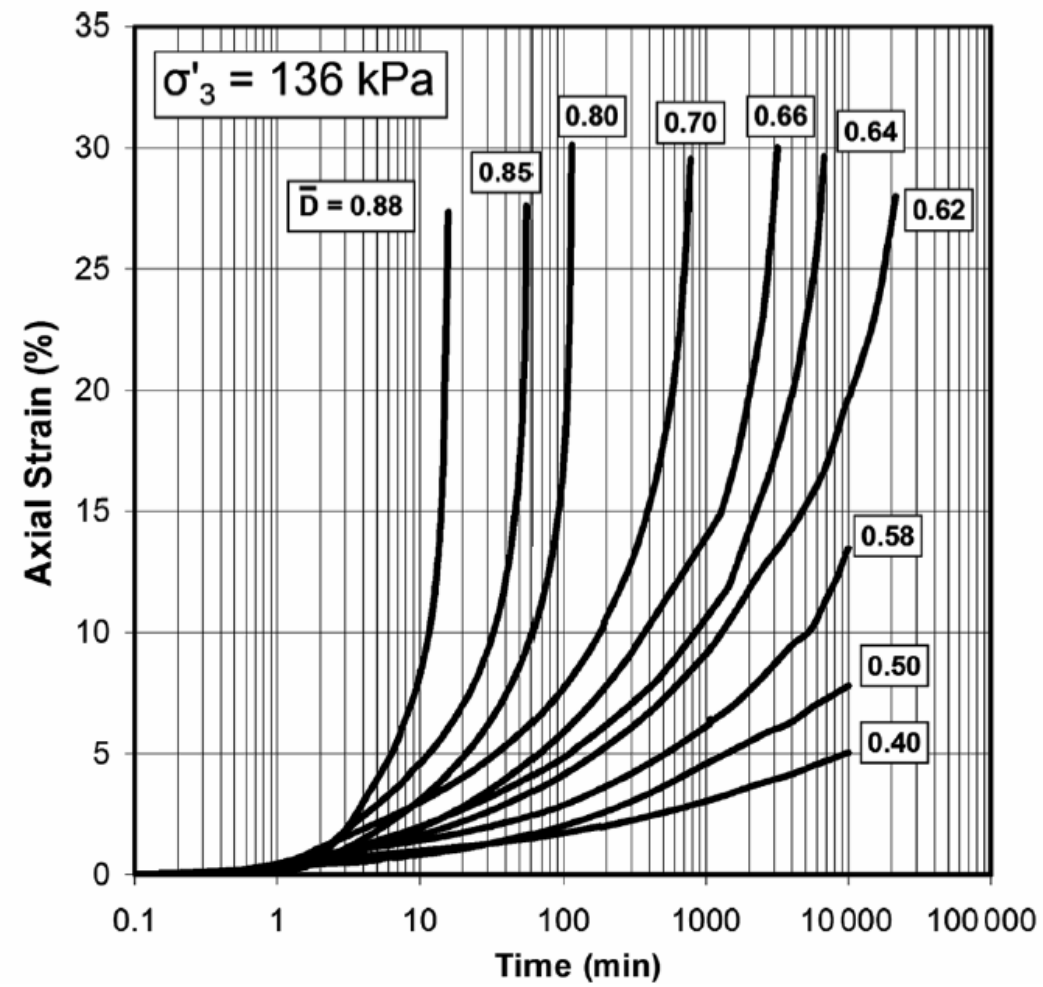

Figure 2.4 Axial strain versus time (logarithmic scale) for recycled asphalt at a constant effective confining pressure of σ_3'= 136 kPa and a variety of deviatoric stresses $\sigma_1 - \sigma_3$. $\overline{D}$ is the ratio of deviatoric stress to its value at failure. Figure reproduced from Viyanant et al. (2007) with permission of the Canadian Geotechnical Journal.

2.2 Definitions

Ideally, when a wave traveling through elastic media, the wave form will be maintained, that is to say, energy is not lost into other forms. But in reality, all materials have faults or loss mechanisms in micro-structure, therefore, as a wave propagates, its energy is absorbed and its intensity (or consequently its amplitude *A(x,t)* that is more easily accessible for measurement) decays with time and with propagation distance *x* according to: (for a harmonic plane wave of a given frequency ω and phase velocity *c*)

$$A(x,t) = A_o e^{-\alpha x} e^{i(\omega t - k_r x)} = A_o e^{i(\omega t - k^* x)} \qquad 2.1$$

where α is the attenuation coefficient (in units of m^{-1}or sometimes *nepers/m*), A_0 is the initial amplitude (usually in *m*), ω is the angular frequency (*radians/sec*), *x* is distance from the origin (in *m*), $k_r = \omega/c$ is the real part of wavenumber (in *radians/m*), and *t* is the time (in seconds). As indicated, Equation 2.1 may also be written with a complex wavenumber $k^* = k_r - i\alpha$.

The attenuation coefficient α, or sometimes simply the attenuation, is a frequency dependent quantity and is, by itself, not that meaningful unless placed in its specific calculation. As such, the attenuation is often given in terms of the quality factor Q. By introducing Q, the dimensionless quality factor, the system's energy loss can be more easily conceptualized. O'Connell and Budiansky (1978) discussed various definitions of Q and the relations to constitutive equations. Generally, from an energy balance perspective, Q is the 2π times the ratio of the energy stored (E) to that dissipated (Δ E) per cycle:

$$Q = \frac{2\pi E}{\Delta E} \qquad 2.2$$

As such, a high value of Q indicates low attenuation. As Equation 2.2 indicates, the direct definition of Q has no frequency term within it and so the relative propensity for a given wave to be absorbed may be more easily visualized.

From a wave propagation point of view, Q represents the number of oscillations required for a freely oscillating system's energy to fall to 1 / $e^{2\pi}$, which may be written for the most general situation (Wang and Guo, 2004) that includes severe attenuation:

$$Q = \frac{\omega}{2\alpha V}\left(1 - \frac{\alpha^2 V^2}{\omega^2}\right) \qquad 2.3$$

but is more usually given as

$$Q(\omega) = \frac{\omega}{2\alpha(\omega)V(\omega)} \qquad 2.4$$

Or from rheological point of view, Q is the real part of modulus (Mr) versus the imaginary part (Mi) (White, 1965):

$$Q = \frac{Mr}{Mi} = \frac{1}{\tan(\phi)} \qquad 2.5$$

where, ϕ is the phase angle.

Q is generally assumed to be constant over the bandwidth of a given seismic experiment, although it is not clear that this should always be true particularly in cases of rocks saturated with viscous fluids (Jones, 1986).

2.3 Review of Mechanisms

Before examining attenuation and velocity in detail, it is useful to first comment that these two aspects of mechanical wave propagation are really intimately tied to one another. That is, if there is attenuation (a lossy process), there must be dispersion and *vice versa*. A propagating signal will not be *causal* without this restriction meaning that components of the wave would nonphysically arrive before they should based on their velocity (e.g. Aki and Richards, 1980). Mechanical waves do arrive causually and hence the waves must be both dispersive and attenuative to some degree; indeed workers in other research fields have attempted to obtain attenuation from dispersion curves using adaptations of the Kramers-König mathematical relationships (Waters and Hoffmeister, 2005), and although this appears to have been successful, the band-limited nature of most

ultrasonic data (as opposed to the full band to infinite frequencies) causes some problems in the analysis of data. In the geophysical literature, a great deal of theoretical effort has been expended to try to maintain causality while keeping attenuation constant or nearly so through "constant Q" assumptions.

Attenuation phenomenon is commonly observed in earth materials all over the globe. Mechanisms that lead to attenuation can be divided into two categories (Stein and Wysession, 2003):

1. extrinsic attenuation, or
2. intrinsic attenuation

The first category, extrinsic attenuation, includes geometric spreading, scattering and multi-pathing. Geometric spreading results from the unavoidable spreading of the wavefront energy over an increasingly large area as the wave propagates away from the source. Scattering is formed when wave interacts with heterogeneity at many scales in the media and thus gets scattered in all directions. Multi-pathing could also be considered as a form of scattering and it results from the refractions and reflections. These phenomenons are all extrinsic, which means energy is not irreversibly absorbed as heat but instead is diverted to other directions and, from the perspective of the receiver, results in a weakening and temporal broadening of the first arriving signal. This type of attenuation is not considered further here.

Intrinsic attenuation, however, is inelastic and wave energy is actually lost into other forms such as heat. The focus of this work focuses on intrinsic attenuation as this is where the issues of dispersion appear. To characterize intrinsic attenuation, researchers have proposed a number of theories, and listed below are some of the well known ones:

1. Frictional dissipation

The frictional dissipation mechanism (Walsh, 1966) attributes seismic attenuation to the relative motion between grain-grain boundaries and crack surfaces (e.g. thin ellipsoidal cracks). It gives a constant Q with frequency, which is common in crustal rocks. This frictional sliding mechanism explains the dependence of

attenuation on pressure in a straightforward way. However, its validity is under question. Mavko (1979) showed that the amplitude dependency is inherent, and data concerning this issue (Winkler et al., 1979) indicates that at low strain amplitude, friction does not make a considerable contribution (e.g. seismic exploration), while high strain amplitude as in the lab with ultrasonic measurements, it dominates the overall effect. Furthermore, friction mechanisms can be nonlinear and the application of this mechanism does not incorporate saturation.

2. Biot theory

Biot theory (Biot, 1956a, b) deals with the dynamic response of a linear porous solid containing compressible fluid. It considers inertial flow and the relative motion between the solid rock frame and the pore fluid. In-phase motion will give a fast wave, while off-phase motion yields a slow wave. Because this mechanism depends fundamentally on bulk properties, it's known as the global flow mechanism. The margin of Biot theory lies in inter and intra crack flows (Dvorkin et al., 1995; Mavko and Nur, 1975).

3. Squirt flow

Squirt flow (Mavko and Nur, 1975; O'Connell and Budiansky, 1978; Dvorkin, et al., 1995) is proposed to make up the gap that is left over by Biot theory: inter crack flow. This mechanism contributes most to attenuation at 100Hz – 1Mhz. Since the Biot and the squirt mechanisms focus mainly on attenuation and dispersion due to pore fluid-rock frame interaction, researchers have proposed certain theories that try to incorporate both (Dvorkin et al., 1995), but the validity is not proved.

Regarding the interaction between pore fluid and rock frame interaction, different mechanisms work for different frequency bands: the squirt mechanism is valid for all frequency bands when viscosity is high, but only works for seismic to sonic when viscosity is low (Wolf et al., 2001; Bazle et al., 2004). The Biot mechanism is valid only at ultrasonic band and sufficiently low viscosity. The

Biot mechanism gives a characteristic frequency that distinguishes the high from the low frequency ranges:

$$\omega_c = \frac{\eta\phi}{k\rho} \qquad 2.6$$

where η is viscosity, ϕ is porosity, k is permeability and ρ is density.

The squirt flow gives a characteristic frequency of:

$$\omega_c = \frac{K\alpha^3}{\eta} \qquad 2.7$$

where K is frame modulus and α is crack aspect ratio. Compare the two characteristic frequencies, the role of viscosity is heightened as whether these mechanisms work at different frequency in the lab or the fields.

Indeed, the role of viscosity in these formulations is quite different as the Biot and the squirt flow theories are directly and inversely proportional, respectively, to the shear viscosity.

4. Relaxation

All phenomena that are termed as "relaxation" (Walsh, 1968; 1969) are in nature, re-equilibrium processes at the molecular scale that result in a time lag. It is commonly used in the field of rheology. Early use of relaxation theory attributes attenuation to shear motions at pore-fluid boundaries and later ones focus on moduli relaxation (Green and Cooper, 1993).

Other mechanisms are also proposed in the literature, include the shearing flow of the fluid layer (Riesz, 1981), gas-pocket squeezing (White, 1975), enhanced inter-crack flow (Mavko and Nur, 1979), stress induced diffusion of absorbed volatile (Tittmann et al., 1980) and energy absorbed in systems undergoing phase change (Spetzler and Anderson, 1968). The many varieties of attenuation mechanisms highlight the complexity of the phenomenon and it is commonly accepted that a single mechanism does not explain the observation fully.

As today's exploration is switching from conventional reservoirs to

unconventional reservoirs (bitumen, heavy oil, oilsands), attention is drawn to attenuation and dispersion in highly viscous liquids. Recent measurements (Batzle et al., 2004) have shown that as the viscosity of bitumen decreases, shear wave propagation is severely impeded, and the velocities of the waves are also reduced. At low viscosity, bitumen is modeled as a Newtonian fluid (Wolf et al. 2006), while at high viscosity, it is considered as a viscoelastic material. Measurements were made and the results support this assumption (Wolf and Mavko, 2005). Under this scenario, shear wave can propagate through bitumen at low temperature, which provides data interpreters another way to characterize reservoirs. The relation of temperature and viscosity can be modeled according to existing documentation (e.g. Beggs and Robinson, 1975, shown in the figure below).

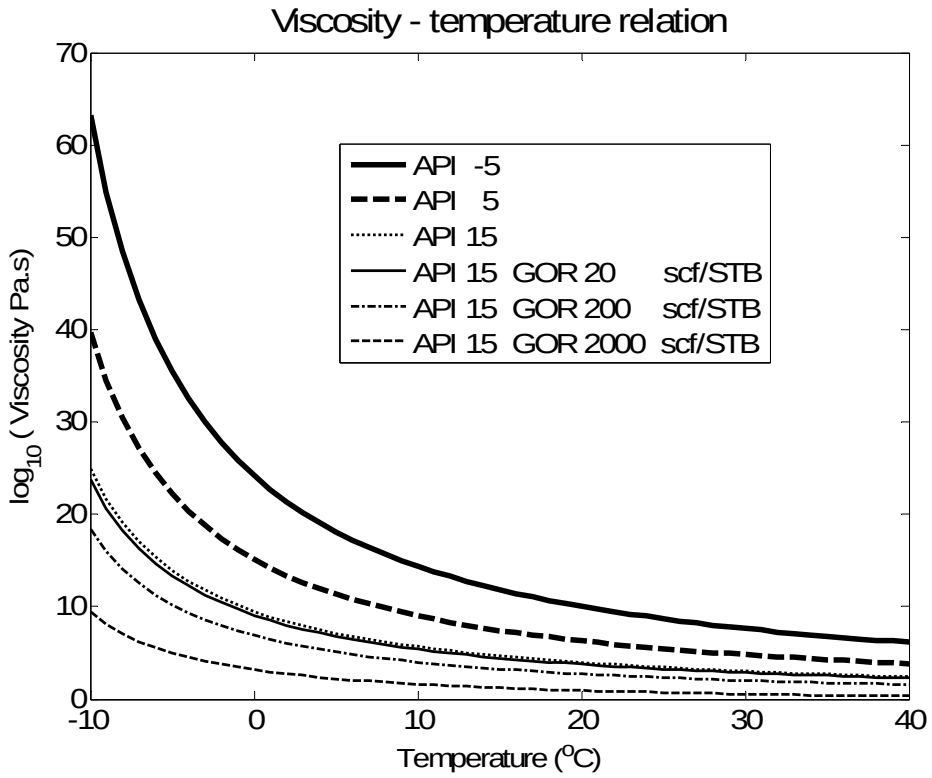

Figure 2.5 Beggs and Robinson's (1975) viscosity - temperature relation for bitumen

2.4 Laboratory Measurement Methods

As mentioned before, both in the laboratory and the field, waveforms, the amplitudes and the spectra of seismic/ultrasonic waves are strongly affected by extrinsic causes in addition to intrinsic attenuation. Therefore, in most cases, to accurately measure intrinsic attenuation, these effects are usually corrected before further study on intrinsic attenuation is taken on.

Attenuation measurements can be carried out by several methods. In the laboratory, commonly used methods include (Zener, 1948; Kolsky, 1953; Schreiber et al., 1973):

1. Free vibration
2. Forced vibration
3. Wave propagation
4. Observation of stress and strain curves

The choice of which method to use is mainly up to the frequency band that is under study. The first two approaches, free and forced vibration work for 100 Hz to 100 kHz; while wave propagation works for over 100 kHz and usually higher. Stress and strain curve observations work for frequencies below 1 Hz.

1. Free vibration

The free vibration technique makes use of the amplitude decay of successive cycles of free vibrations. Usually, a rod of rock is suspended vertically so that a mass with a large moment of inertia can be attached to its lower end, then an initial stress is applied, and the system is allowed to vibrate freely. The vibrating frequency is a function of the rock properties and the moment of inertia of the mass. The rate of decay of the amplitude is attributed to energy loss. This method is also used to determine the elastic constant and attenuation of metals and composite materials at high temperatures and very low (approximately 1 Hz) frequencies (Kingery, 1959; Jackson, 1969). However, it is difficult to fabricate long cylindrical rock sample with the uniform cross sections in the lab. Moreover, the initial stress must be low so that the sample does not fracture.

2. Forced vibration

A more common method is the forced longitudinal or torsional vibration of long bars, therefore it is also named resonant bar method. This method is based on standing waves. For longitudinal and torsional waves, the wave velocity is given by:

$$V = \lambda f_c = \frac{2lf_c}{n}, n = 1, 2, 3, ... \quad 2.8$$

where f_c is the resonant frequency of mode n and l is the length of the sample.

Relationships between Young's modulus and resonant frequency for longitudinal vibrations, between shear modulus and resonant frequency for torsional vibrations are derived by Spinner and Tefft (1961). These relationships are summarized by Schreiber et al (1973). If the system can be turned off easily, the subsequent decay of amplitude is used to calculate Q.

While resonant methods are easily implemented, there are also some limitations. One major concern in resonant technique is the radiation loss into surrounding medium, which should be substracted from the measured values, particularly in longitudinal tests. Browne and Pattison (1957) analyzed this problem and indicate that such effects are negligible for low Q materials in ambient air conditions, but could be substantial for high Q materials. Another problem is the use of jacket. It alters the resonant frequency thus the observed values are for the average of the sample and jacket.

3. Wave propagation

The wave propagation method in the past a couple of decades are of particular interest because the loss parameters measured this way could be compared to those obtained from the field. This approach assumes that amplitude of seismic waves decay exponentially with distance or time and the extrinsic loss can be corrected. However, among different extrinsic loss mechanisms such as beam spreading, side wall reflection, mode conversion, transducer loss and the wedging problem, only limited number of effects can be corrected for experimentally,

leaving the rest to be estimated empirically (Truell et al, 1969).

In practice, wave propagation can be carried out in two ways: by pulse-echo and through-going (transmission). The former looks into the amplitude decay of multiple reflections from a free surface, usually the other end of the sample. Provided that the system is linear and amplitude can be obtained directly, the attenuation coefficient can be calculated from:

$$\alpha = \frac{1}{2l} In[A(1)/A(2)] \qquad 2.9$$

where l is sample length, $A(1)$ and $A(2)$ are two successive echoes.

For highly attenuating samples, a reference material (usually aluminum for its low attenuating property and is tested prior to the real sample) can be used with signal of the same frequency. Then two echoes from sample and reference material are compared to calculate attenuation coefficients. However, since the minimum travel path is twice the sample length, which would greatly impair the signal quality in highly attenuating samples, thus the use of pulse-echo method is limited to high-Q samples such as single crystals. Another drawback of pulse-echo is when the system is under pressure, energy loss to pressurized surrounding media is usually not negligible. Whereas under atmosphere pressure, this technique has been used successfully on some fine-grained limestone by Peselnick and Zietz (1959).

The through-going method is mostly suited in pressure vessels with jacketed or saturated samples, such as oil sands. In practice, transducer pairs are installed at both ends of the sample, depending on the transducer size and the sample diameter, different loss correction may be employed. For samples of diameter larger than transducer size, side wall effects are negligible, while for samples of small diameter but long length, inverse-length beam spreading may be assumed.

Attenuation is calculated from response of an initial pulse by taking the spectral ratio decomposition, which is a common technique used in seismology. It eliminates many problems associated with wave propagation methods, such as spreading. As is favored by many lab researchers, through-going method is employed in this study. As the analysis method, spectral decomposition will be

discussed later in Chapter 6.

4. Stress and strain curves

Attenuation can also be measured from hysterisis in stress-strain curves in loading and unloading tests, provided the cycle frequency is removed from the system's resonant frequency (Brennan and Stacey, 1977; Pelselnick et al., 1979). This technique takes account of the loading and unloading paths. The area between these paths in stress-strain space reveals the energy dissipated and this information then allows for calculation of Q by dividing maximum work done by this energy loss. This technique, theoretically speaking, offers a promising way of obtaining Q for small samples under high pressure and temperature at seismic frequencies and over a wide range of stain amplitudes. However, the ideally required pure shear and dilatational stresses are not easy to obtain. Torsional shear and uniaxial stress are usually present. Secondly, the response of the system is a function of the driving stress; if the linearity of the attenuation mechanism is to be extracted, then very low distortion sine waves must be employed. This requirement limits the stress-strain curve technique in the application of measuring dynamic strain.

2.5 Review of Measurements

Because attenuation is a comprehensive phenomenon combining geometry spreading, scattering, multipathing, and intrinsic attenuation, its accurate measurement is a difficult task. To estimate the intrinsic attenuation, one has to correct for extrinsic causes. For instance, Green and Wang (1991) proposed a formula to correct shear wave diffraction loss for plane-polarized transducers when Kirchoff limit ka is small where k is wave number and a is the source and receiver radius. Different but effective treatments are needed to eliminate extrinsic effects or at least to correct or estimate their effects.

A vast number of measurements have been carried out in the past a few decades on dry and saturated rocks or man-made materials presenting similar

properties. Research focus first rests on dry and saturated porous media, and then shifts to the liquid parts that are trapped within. In some cases, the system can roughly be viewed as a viscoelastic system and thus the relaxation theory does a better job phenomenalogically explaining attenuation and velocity dispersion than others although it must be remembered that the viscoelastic models do not necessarily relate directly to the physical mechanisms that produce the attenuation.

Velocity and attenuation in partially molten rocks is modeled by interconnected tubes along grain edges (Mavko, 1980). It is found that at 20 kbar, a 0.05 melt fraction results in a 5% decrease in V_p and a 10% decrease in V_s. This model excludes the inelastic relaxation, thus Mavko indicates that considerable bulk attenuation is expected when relaxation is considered and shear attenuation appears to be dominated by viscous flow.

Toksoz et al. (1979) did through-going pulse measurements on dry and saturated sandstones. They report a linear relation between attenuation coefficient and frequency assuming a constant Q. Attenuation in the P wave is less than the S wave, at frequency range 0.1-1.5MHz. This linear relationship between attenuation coefficient and frequency is proposed in literature for many theoretical models such as the Kolsky (1956), Azimi (1968) and Cole-Cole (1941) models. However, for liquid saturated real samples, it is rarely reported as linear. And this relation found by Toksoz et al. may indicate that liquid within rock frames may have less impact than expected, but since many parameters act at the same time (viscosity, pressure, saturation level…), further study is needed to reveal the role of oil-like liquid in porous media regarding the behavior of ultrasonic waves.

Regarding oil sands, damping ratio[2] was measured by Hsu et. al. (1988) under axially applied confining pressure. They monitored cyclic strain variation as a function of deviatoric stress, and thus calculate damping ratio from the hysteresis. In this paper, they conclude that damping ratio is independent of deviatoric stress but increases with strain rate. Increasing confining pressure decreases the damping ratio. They also conclude that the density and the length of the sample do not affect the damping ratio significantly. The damping ratio found this way is between 0.25 and 0.45 under a strain rate of 0.01% /s.

In Tompkins et al.'s (2000) paper, 30 oceanic basalt samples were measured by pulse-echo ultrasonic techniques. They observed the dependence of Q and α on confining pressure. The quality factors they observed are low with Q_P 14-167 and QS 8-27. The Q_S/Q_P ratio is considered as an indicator of saturation in addition to V_P/V_S. They conclude that highly saturated samples have low Q_S/Q_P ratios (<0.4) but high V_P/V_S ratio (>1.75). In laboratory measurements, increasing importance is given to such observations because with the P wave alone, one is not able to characterize a system with so many uncertainties. A preferred way of featuring these systems is through both P and S wave information.

In recent literature, Wolf et al. (2006) point out that highly viscous pore fluid affects attenuation and velocity dispersion. They simulated intrinsic properties of pore fluids with Maxwell's model, and the results indicate that attenuation is frequency-dependent and different mechanisms account for different frequency band. The Biot and squirt theory work for low viscosity cases, but these effects are negligible for low permeability and high viscosity fluid. In this case, viscoelastic effects are likely to be the dominant factor. They suggest that the viscoelastic behaviour be measured on fluid and fluid-solid separately to yield light on the interaction mechanism.

With more and more research interest put on viscoelastic properties of earth materials, tests on such materials were made in many studies since the early 60s. For example, asphalt tested with steady state flow identified it as viscoelastic

[2] The damping ratio is defined by $\Delta D/(4\pi \Delta U)$, where ΔD is the dissipation energy and ΔU is the strain energy (Hsu et al. 1988).

body which displays Newtonian and non-Newtonian behaviors (Brodnyan, 1960). Regarding velocities of liquid oil, P and S wave velocities in a variety of oils were measured by Wang et al (1990) with an ultrasonic through-going method. They found that the acoustic velocities are greatly affected by temperature, pressure and density. For the 11 oils that were tested, the empirical equations predict the velocity relations better than more fundamental liquid-state theories that provide only qualitative trends. This indicates that more research needs to be done possibly from a viscoelastic approach to yield better models that predict liquid behaviors.

Among the large number of papers in literature, it is commonly accepted that no single mechanism has proven to dominate attenuation from seismic frequency to ultrasonic frequency. Mechanisms can be related and affect each other under conditions such as high pressure, at transient stage, or consolidation of oil when temperature drops. This obscures the results, and thus limits each individual study to a narrow range of conditions. However, several commonly believed points can be drawn from a bulk body of literature regarding attenuation and dispersion:

1. Liquid properties themselves may have an effect on attenuation and dispersion instead of or in addition to the Biot or squirt flow solid-fluid interactions (Zhang and Guo, 2000)
2. Traditional Navier-Stokes equation and shear viscosity fail to explain lab measurements on highly viscous materials, and more fundamental study on fluid properties and attenuation is needed.
3. Since fluids, and particularly highly viscous fluids, play increasingly important roles, the frequency-dependency becomes apparent and its limitation could result in quite different outcomes between the field and laboratory.
4. In addition to the P wave information, additional data on the S wave dispersion and attenuation would also be useful.

Chapter 3
Theoretical and Phenomenological Description

This chapter consists of an overview of the theory that may be used to describe wave propagation through elastic and viscoelastic materials, the behaviour of which was introduced in the previous chapter. The chapter begins with elastic and non-attenuating materials to introduce the concepts then leads through various phenomenological viscoelastic models. This information will then be used in the next chapter in some illustrative modeling of wave propagation through different materials.

3.1 Concepts of Stress and Strain

Deformation of earth materials is always an interesting topic especially as it deals with rocks physics, plate tectonics, and other processes. However, how the deformation is viewed will depend on a number of factors that includes the level of loading and the time scale over which deformation is observed. As such, the behavior of a material is said to be elastic, plastic, or visco-elastic. Classical stress and strain theory attempts to describe these deformations using tensors.

It is important to first define the stress; full mathematical treatments of this definition that consider stress as the limit of a force onto an infinitesimal area may be found in numerous texts (e.g. Malvern, 1969) and only an abbreviated version is given here. It is useful to consider a bound region within the stressed material with an infinitesimal cube. Under a static state of stress this material is not moving, i.e. it is at equilibrium and hence all the forces acting on its surface (ignoring body forces here) must be in balance. For simplicity, let the faces of the cube be aligned with a standard Cartesian co-ordinate system *x-y-z,* shown in Figure 3.1 below:

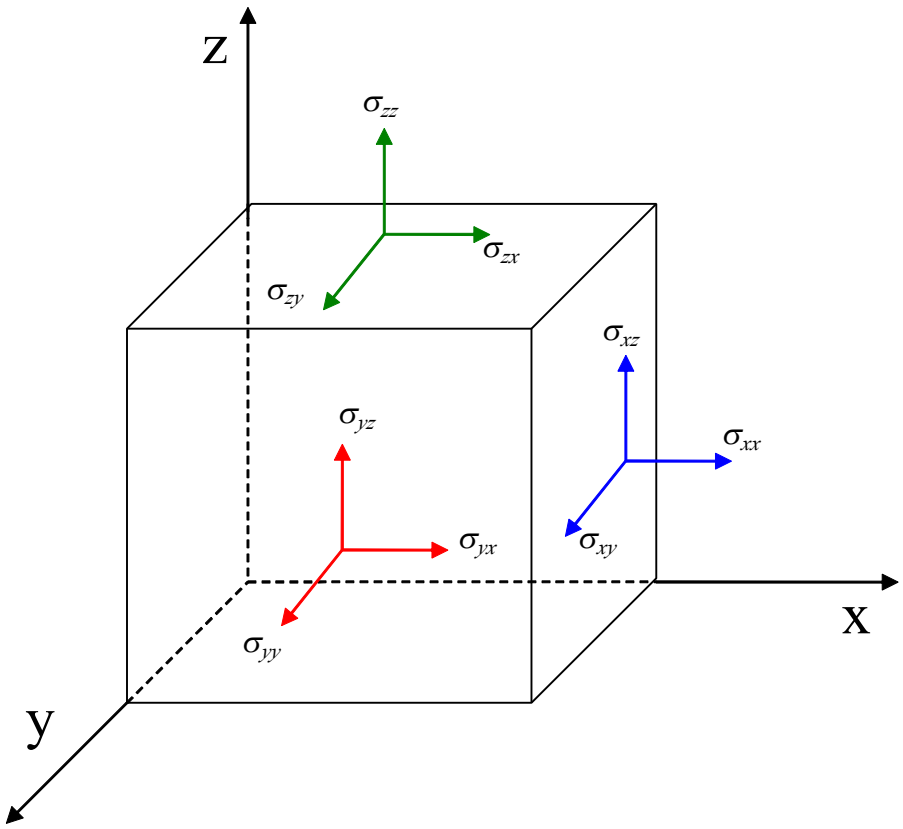

Figure 3.1 Stress vectors in x, y and z components

The elements of the force acting on each surface of this cube can be represented by three *stress* or *traction* vectors σ_{ij} (i, j = x, y, z). The indices *i* and *j* indicate the normal direction to the plane upon which the given stress acts and the direction in which the stress acts. This results a normal stress that acts perpendicular to the surface ($i = j$) and shear stresses that act parallel to the surfaces ($i \neq j$). Stress in a physical meaning, is the force acting on different faces of the cubical element towards different directions (Ferry, 1980). Therefore the unit of stress is the same as pressure, i.e. a force per unit area. Commonly used units in geophysical study are pascals (Pa = N/m^2) in SI units, bars (100 kPa) , or dyne/cm^2 (0.1 Pa)[1].

In a complete representation, 9 stress elements are needed to describe the status of a body, which makes stress a second order tensor. However, equilibrium requires that (e.g. Lay and Wallace, 1995):

$$\frac{\partial \sigma_{ij}}{\partial x_i} = 0$$
$$\sigma_{ij} = \sigma_{ji} \qquad i, j = 1, 2, 3. \tag{3.1}$$

where $i, j = 1, 2, 3$ are representative of $i, j = x, y, z$.

Upon the application of external or internal forces, a medium undergoes deformation in the form of both length changes and/or angular distortions. Within the frame of finite deformation, 'infinitesimal' change (usually taken to be less than $10^{-5} \sim 10^{-4}$ in a normalized manner, Lay and Wallace, 1995) is usually assumed in elasticity. For a cubic cell deforming in three directions, the final shape is determined by the displacement of all points in the body. Instead of detailing the displacement field directly, the strain tensor is introduced to characterize deformation. Essentially, the strain ε_{ij} represents a dimensionless normalized measure of the displacement.

[1] Many parts of the petroleum industry remain resistive to the SI system; the lbs/in^2 (or psi) remains a common unit used, 1 psi = 6,894.76 Pa.

$$\varepsilon_{ij} = \frac{1}{2}\left(\frac{\partial u_i}{\partial x_j} + \frac{\partial u_j}{\partial x_i} \right) \qquad i, j = 1, 2, 3. \tag{3.2}$$

where u_i represents the components of displacement (with i, j =1, 2, 3 representing the x, y, z components, respectively) of displacement vector and the x_i represent an axis in the Cartesian reference system. Similar to stress, both normal and shear strains may be defined which represent changes in size and shape, respectively. Also, the strains are symmetric with $\varepsilon_{ij} = \varepsilon_{ji}$ so that there are only six independent strain components.

The symmetry of the stresses and the strains allows for a simplified notation, apparently first developed by Voigt, which includes only one subscript to be employed with

$$\begin{aligned} &\varepsilon_1 = \varepsilon_{11} \qquad \varepsilon_2 = \varepsilon_{22} \qquad \varepsilon_3 = \varepsilon_{33} \\ &\varepsilon_4 = 2\varepsilon_{23} \qquad \varepsilon_5 = 2\varepsilon_{13} \qquad \varepsilon_6 = 2\varepsilon_{12} \end{aligned} \tag{3.3}$$

Similar nomenclature applies to stress tensor:

$$\begin{aligned} &\sigma_1 = \sigma_{11} \qquad \sigma_2 = \sigma_{22} \qquad \sigma_3 = \sigma_{33} \\ &\sigma_4 = \sigma_{23} \qquad \sigma_5 = \sigma_{13} \qquad \sigma_6 = \sigma_{12} \end{aligned} \tag{3.4}$$

3.2 Hookean Elastic Materials

The simplest mechanical material will have a linearly elastic response in which stress is linearly related to the strain (Lay and Wallace, 1995). When the stress is removed, the strain is restored along the same path to the initial level as discussed in Chapter 2; this linear relationship is referred to as Hooke's law. In the most general case of a triclinic solid (i.e. the least symmetric material) 21 independent elastic parameters are required to give Hooke's law; these 21 constants may be represented in a symmetric 6 X 6 matrix such that Hooke's Law (Bhatia, 1986; Lay and Wallace, 1995; Aki and Richards, 1980):

$$\begin{bmatrix}\sigma_1\\ \sigma_2\\ \sigma_3\\ \sigma_4\\ \sigma_5\\ \sigma_6\end{bmatrix} = \begin{bmatrix} c_{11} & c_{12} & c_{13} & c_{14} & c_{15} & c_{16}\\ c_{12} & c_{22} & c_{23} & c_{24} & c_{25} & c_{26}\\ c_{13} & c_{23} & c_{33} & c_{34} & c_{35} & c_{36}\\ c_{14} & c_{24} & c_{34} & c_{44} & c_{45} & c_{46}\\ c_{15} & c_{25} & c_{35} & c_{45} & c_{55} & c_{56}\\ c_{16} & c_{26} & c_{36} & c_{46} & c_{56} & c_{66}\end{bmatrix}\begin{bmatrix}\varepsilon_1\\ \varepsilon_2\\ \varepsilon_3\\ \varepsilon_4\\ \varepsilon_5\\ \varepsilon_6\end{bmatrix} \qquad 3.5$$

where the individual c_{ij} are the elastic stiffnesses. For anisotropic media, $\frac{2c_{44}}{c_{11}-c_{12}}$ is often used to indicate the degree of anisotropy (Bhatia, 1986).

In this thesis, however, we assume a much simpler case of isotropy in which the elastic physical properties do not depend on the direction from which the material is viewed. An isotropic material can be considered to have infinite symmetry and as such less information is required to describe the material's behavior. The elastic matrix can be further reduced to only 2 independent 'Lamé constants' $\lambda = c_{12}$ and $\mu = c_{44}$ in the following form (Bhatia, 1986):

$$c_{ij} = \begin{bmatrix} \lambda+2\mu & \lambda & \lambda & 0 & 0 & 0\\ \lambda & \lambda+2\mu & \lambda & 0 & 0 & 0\\ \lambda & \lambda & \lambda+2\mu & 0 & 0 & 0\\ 0 & 0 & 0 & \mu & 0 & 0\\ 0 & 0 & 0 & 0 & \mu & 0\\ 0 & 0 & 0 & 0 & 0 & \mu\end{bmatrix}$$

$$= \begin{bmatrix} c_{12}+2c_{44} & c_{12} & c_{12} & 0 & 0 & 0\\ c_{12} & c_{12}+2c_{44} & c_{12} & 0 & 0 & 0\\ c_{12} & c_{12} & c_{12}+2c_{44} & 0 & 0 & 0\\ 0 & 0 & 0 & c_{44} & 0 & 0\\ 0 & 0 & 0 & 0 & c_{44} & 0\\ 0 & 0 & 0 & 0 & 0 & c_{44}\end{bmatrix} \qquad 3.6$$

where $c_{11} = c_{22} = c_{33} = \lambda + 2\mu$

$c_{12} = c_{13} = c_{23} = \lambda$

$c_{44} = c_{55} = c_{66} = \mu$

or in a more succinct Einstein notation[2] form

$$\sigma_{ij} = 2\mu\varepsilon_{ij} + \lambda\varepsilon_{kk}\delta_{ij} \qquad i,j = 1,2,3. \tag{3.7}$$

where δ_{ij} is the Kronecker delta[3].

Alternatively, one may write strain as a function of stress for this case as:

$$\varepsilon_{ij} = \frac{1+\nu}{E}\sigma_{ij} - \frac{\nu}{E}\delta_{ij}\sigma_{kk} \qquad i,j,k = 1,2,3. \tag{3.8}$$

where E is the Young's modulus (ratio of the normal stress with the resulting normal strain in the same direction) and Poisson's ratio (the negative of the ratio between the strain perpendicular to the normal strain and the normal strain).

Hooke's law links the applied stress to the instantaneous elastic strain via the elastic stiffnesses that are material dependent. However, Hooke's law by itself does not provide the variation of the displacement field with time; and the equation of motion (EOM) must be used as is described in the next section.

3.3 Elastic Waves in Solids

Detailed description of wave propagation in elastic media can be found in any text book on elasticity theory (Bhatia, 1986) or advanced seismology (e.g. Aki and Richards, 1980; Lay and Wallace, 1995; Shearer, 1999; Stein and Wysession, 2003) and much of the details do not need to be described here. This section aims to include some basic concepts that are beneficial to later discussion.

As is well known, solid elastic media possess rigidity, therefore both compressional (P) and shear (S) wave can propagate. The analysis of propagation law begins with fundamental stress and strain relation stated above. A mono-frequency plane wave traveling through an isotropic media in x direction will have a harmonic particle displacement amplitude *S(x,t):*

---

[2] The Einstein notation is a convention for simplifying long expressions particularly in linear algebra. The convention. The appearance of an index variable (the *i,j,k* above) twice in a term means that all the similar terms with all possible values are summed. In the case here the indices 1, 2, and 3 represent the three spatial dimensions.

[3] The Kronecker $\delta_{ij} = 1$ when $i = j$ and 0 when $i \neq j$. Named after the German mathematician L. Kronecker (1823-1891).

$$S(x,t) = S_o e^{j(\omega t - kx)} \tag{3.9}$$

where ω is angular frequency and $k = 2\pi/\lambda$ is wave number with λ the wavelength, and S_o is amplitude which normally can be the maximum absolute value of the particle displacement from its equilibrium position.

The wave equation for isotropic media can be obtained by substituting Hooke's law (Equation 3.5) into the equation of motion (Bhatia, 1986), employing the definition of strain in terms of displacement, and applying some mathematical identities with the final result:

$$\rho \frac{\partial \mathbb{S}^2}{\partial t^2} = (c_{12} + 2c_{44})\nabla^2 \mathbb{S} = (\lambda + 2\mu)\nabla^2 \mathbb{S} \tag{3.10}$$

$$\rho \frac{\partial \mathbb{S}^2}{\partial t^2} = c_{44}\nabla^2 \mathbb{S} = \mu \nabla^2 \mathbb{S} \tag{3.11}$$

where ρ is the density, c_{12} and c_{44} are the two independent elastic stiffnesses.

The above two equations are wave equations for P and S wave with solutions for the wave speeds of:

$$V_p^2 = = (c_{12} + 2c_{44})/\rho = (\lambda + 2\mu)/\rho \tag{3.12}$$

for the compressional wave speed and

$$V_s^2 = c_{44}/\rho = \mu/\rho \tag{3.13}$$

for the shear wave speed. It is important to reiterate that these equations do not account for dispersion, or perhaps more directly the elastic moduli here are constant and independent of frequency.

In rock physics and seismology, wave velocities are usually expressed in the form of bulk modulus K and shear modulus μ[4]. Note that any elastic isotropic solid requires only two elastic parameters for a full description, these can be for example the stiffnesses c_{12} and c_{44}, the Lamé parameters λ and μ, or other

[4] The shear modulus has two commonly used symbols: G and μ, with latter the same as one of the Lamé parameters. Later discussion in this work prefers G in the distinguishing appearance.

parameters with more direct physical meaning such as the bulk modulus K and the shear modulus μ.

The bulk modulus of a substance essentially measures the substance's resistance to uniform compression. It is defined as the pressure increase needed to produce a decrease in volume:

$$K = -\mathrm{V}\frac{\partial p}{\partial V} \tag{3.14}$$

where p is pressure, V is volume, and $\partial p/\partial V$ denotes the partial derivative of pressure with respect to volume. The inverse of the bulk modulus gives a substance's compressibility.

The shear modulus, G, or μ, sometimes referred to as the modulus of rigidity, is defined as the ratio of shear stress to the shear strain

$$G = \mu = \frac{\sigma_{ij}}{\varepsilon_{ij}}, i \neq j \tag{3.15}$$

where σ_{ij} is shear stress and ε_{ij} is the associated shear strain.

Bulk and shear moduli are usually measured in GPa (giga-pascals) or ksi (thousands of pounds per square inch). In order to substitute elastic constants, the bulk and shear moduli are related to them as follows:

$$\begin{aligned} K &= \mathrm{c}_{12} + \frac{2}{3}\mathrm{c}_{44} = \lambda + \frac{2}{3}\mu \\ G &= \mathrm{c}_{44} = \mu \end{aligned} \tag{3.16}$$

Therefore, solutions of wave equations give rise to P and S velocities in the form below (Bhatia, 1986):

$$\begin{aligned} V_p^2 &= \left(K + \frac{4}{3}G \right) / \rho \\ V_s^2 &= G / \rho \end{aligned} \tag{3.17}$$

Obviously, both velocities are inversely proportional to the square root of density. The S wave is also influenced by the shear modulus G while the P wave is influenced by both bulk and shear modulus. It is important to note that for a perfect fluid $G = 0$, the fluid does not support a shear stress and hence no shear

wave can propagate. In this situation too, the compressional wave velocity reduces to $(K/\rho)^{1/2}$.

For perfect fluids, the equation of motion, the wave equation and the velocity are obtained under the following assumptions:

1. Viscosity is zero (see next section).
2. No heat is transferred in or out of the element volume during propagation of the acoustic waves (i.e. the wave propagation is said to be adiabatic).
3. The state of an element can be described by two independent parameters: the pressure difference P and the mass density ρ.

Under such assumptions, pressure and density changes take place reversibly. Therefore pressure wave can propagate in such media with no attenuation.

The next sections carry through this review for the viscoelastic media.

3.4 Lossy Viscoelastic Materials – Shear Viscosity

The term "rheology" involves the deformation and the movement of matter, such as liquid, fluid-saturated or molten materials. In common usage, it is a general term that covers the flow characteristics of materials under conditions of pressure, temperature, and time scale. In the geosciences, the temperature, the pressure and the strain rate are required to describe the nature of deformation in most earth minerals (Ranalli, 1987). In such materials, the energy of deformation is dissipated due to viscous flow, and the material does not allow for elastic storage of energy at least at sufficiently long time scales. Another way to say this is that the material does not support a shear stress. This differs from the case of elasticity where no energy is dissipated by deformation and energy may be stored in a stressed system.

However, between these end member cases of elasticity where energy is stored and viscosity where energy is dissipated, there exist some materials that have characteristics of both. Such materials will behave elastically with an instantaneous strain upon application of a rapid load which is then followed by viscous flow. Such material is referred to as viscoelastic and some examples of viscoelastic behavior were presented in the previous chapter.

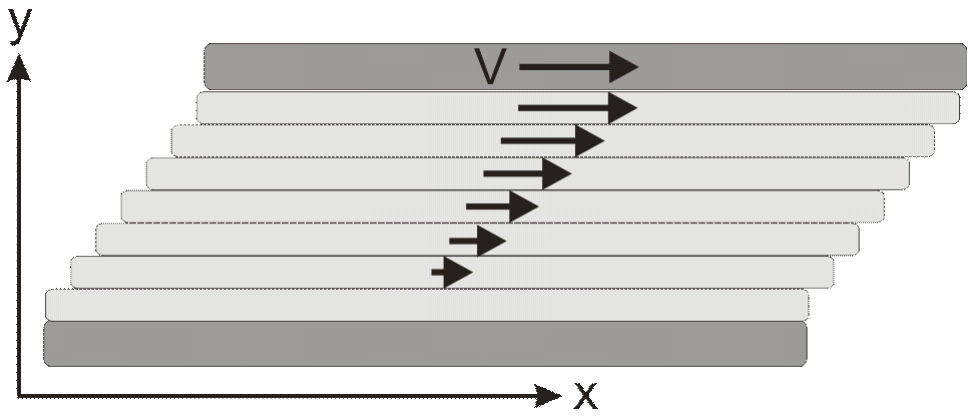

Figure 3.2 Classic representation of Newtonian shear viscosity. Upper plate move to the right with speed V while lower plate is immobile. Each 'lamina' of fluid, parallel to the plates, moves at an increasing speed relative to the lower plate. Figure courtesy of D. Schmitt from Geophysics 332 Lecture Notes.

The concept of the deformation of a viscous material in shear is typically introduced by considering motions of the 'fluid' between two plates a distance *d* apart and moving relative parallel to one another at a relative speed *V*. The primary bulk motion of the fluid will be in the x direction with the different lamina traveling at speeds intermediate between the motionless bottom plate and the moving top plate. Resistance to this motion is caused by the additional and random thermal motions of the fluid molecules between the lamina, each motion of which results in a transfer of momentum which is manifest in both by a dissipation of energy and by a shear stress

$$\sigma_{xy} = \eta \frac{\partial V}{\partial y} = \eta \dot{\varepsilon}_{xy} \qquad 3.18$$

where the gradient of the velocity $\partial V/\partial y = \dot{\varepsilon}$ is the strain rate (s^{-1}) and η is the dynamic shear viscosity ($Pa \cdot s$). At this point, the physical meaning of shear viscosity is the ratio between shear stress and resultant strain rate.

In some cases, as the applied stress increases, the strain rate remains approximately a constant after a transient stage (Figure 3.3a). This is called the

steady-state flow, in which linearity maintains over the interested range, therefore, a constant shear viscosity that independents from stress is anticipated. The corresponding strain rate depends on the applied stress as well as temperature in most cases. This phenomenon is commonly observed in fluids such as water, and they are named Newtonian fluids in general. (Ferry, 1980; Christensen, 1982; Ranalli, 1987).

In other cases, stress-strain rate relation is not linear, and the creep in such cases is called *transient flow*. Quite often, the strain rate increases faster than stress and viscosity decreases with increasing stress. Such fluids are called non-Newtonian fluids (e.g. non-drip paints, silicate poly-crystals (Ranalli, 1987)) The flow is called *power-law flow*, (Figure 3.3b), because stress-strain rate relation can be described by a power law (Ferry, 1980; Christensen, 1982; Ranalli, 1987):

$$\dot{\varepsilon} \propto \sigma^{n} \qquad 3.19$$

where the exponent *n* depends mainly on the property of the material. Usually an empirical value is used, with lab measurements as verification. Power law flow has a strong dependence on temperature while only a relatively weak dependence on pressure.

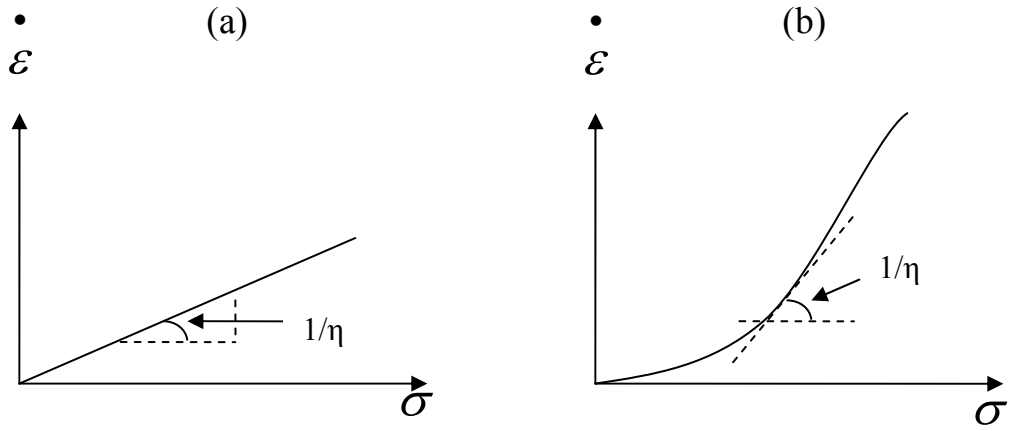

Figure 3.3 Different flow regimes: (a) steady state flow, viscosity is a constant at all stress levels; (b) power law flow, viscosity decreases as stress increases.

To sum up the deformation regimes, the elastic, viscoelastic and rheological response of materials can be categorized into four categories (Webb, 1997):

(1) instantaneous, recoverable, elastic deformation;

(2) time-dependent, partially recoverable, transient deformation (plastic)

(3) time-dependent, non-recoverable, viscous linear deformation

(4) time-dependent, non-recoverable, viscous power law deformation

In the next sections, mechanical wave propagation and attenuation through such materials will be examined in order to study the effect of frequency.

3.5 Wave propagation in Viscous Materials

Unlike solids, a shear wave does not propagate in perfect fluids because the shear viscosity η is zero. This is assumed in some theories that deal with fluids substitution (Gassmann, 1951 for instance). However, for real liquids, η is actually not zero, and it is a strong function of temperature. Table 3.1 shows the shear viscosity of some earth materials:

Table 3.1 Shear viscosity of earth materials*

Material	Order of shear viscosity (Pa.s)	Temperature (^{o} C)
water	10^{-3}	20
molten basalt	10^{2}~10^{4}	1100-1400
pitch	10^{9}	15
glacier ice	$1.2x10^{13}$	\
mantle	10^{20}~10^{22}	\

*Data from Ranalli (1987)

For such fluids, the equation of motion needs to be adapted by adding a viscosity term. We begin by examining an incompressible Newtonian fluid, if the shear viscosity is considered, the concepts of stress and strain definitions in elasticity can be borrowed to address this problem but now with:

$$\sigma_{ij} = -p\delta_{ij} + 2\eta \dot{\varepsilon}_{ij} \qquad i,j = 1,2,3. \tag{3.20}$$

where the first term p is the equidirectional or hydrostatic pressure, and the second is the shear viscosity induced stress. Substituting this stress with the new viscosity term into Euler's equation, the equation of motion can be simplified to the *Navier-Stokes* equation (Liggett, 1994):

$$\rho \frac{Du_i}{Dt} = -\rho g \frac{\partial h}{\partial x_i} - \frac{\partial p}{\partial x_i} + \frac{1}{3}\eta \frac{\partial}{\partial x_i}\frac{\partial u_j}{\partial x_j} + \eta \frac{\partial^2 u_i}{\partial x_j \partial x_j} \qquad 3.21$$

where D/Dt is material derivative (see Malvern, 1979), h is elevation and g is the acceleration of gravity. This form of the Navier-Stokes equation describes the motion of an *incompressible* fluid substance in steady state, such as liquids. The physical meaning is that changes in momentum in infinitesimal volumes of fluid are simply the sum of dissipative viscous forces (similar to friction), the changes in pressure, and including a body for where appropriate that is gravity, and other forces acting inside the fluid. It is another application of Newton's second law. As indicated, the shear viscosity in this equation can be a function of temperature, decreasing with temperature for liquids, and increasing with temperature for gases (Kundu, 1990).

There are practical situations in which viscoelastic media may be subjected to transverse oscillation. Such waves exist but are very highly attenuated in lower viscosity fluids; Bhatia (1986) refers to them as viscous waves. Consider a transverse harmonic wave propagating in x_1 direction, with particle velocity S_2 in x_2 direction.

$$S_2 = S_2^0 \exp\{i(\omega t - k x_1)\}, \qquad \mathbb{S} = \mathbb{S}(0, S_2, 0) \qquad 3.22$$

By substituting it into the equation of motion, one obtains:

$$\rho \frac{\partial^2 S_2}{\partial t^2} = \eta \frac{\partial}{\partial t}\left(\frac{\partial^2 S_2}{\partial x_1^2}\right) \qquad 3.23$$

The solution (substituting Equation 3.22 into 3.23) of this equation leads to a complex wave number:

$$k^* = k_1 - i\alpha \qquad 3.24$$

where $k_1 = \alpha = \sqrt{\rho\omega / 2\eta}$. This means that the shear wave velocity would be:

$$V_S^2 = \left(\frac{\omega^2}{k_1^2}\right) = \frac{2\eta\omega}{\rho} \qquad 3.25$$

and with the quality factor that is simply Q → 0 (see Chapter 2) indicating a high degree of overdamping. In practice, it would be difficult or impossible to measure such a wave.

It is interesting to note, however, that various workers are using reflectivity techniques to determine the shear wave properties of complex fluids such as heavy oils (Han et al., 2005).

This equation means: 1) shear wave is able to propagate in liquids if shear viscosity is not zero although they are highly and rapidly attenuated; 2) as viscosity increases, shear wave velocity increases; 3) wave velocity has a natural dependency on frequency - high frequency component travels faster than low frequency.

Of more practical interest, however, is the attenuation and propagation of compressional waves in viscous fluids.

3.6 Wave Propagation in Compressible Fluids

As discussed in previous section, for viscous flow which is usually the case in organic liquids, the contribution from viscous forces is not negligible. Moreover, by introducing a shear viscosity, it is still not adequate to describe the phenomenon in the lab. As a consequence, the fundamental mechanism of attenuation in viscoelastic media needs to be reviewed with criticism. Recall in the last two chapters, the characterization of fluids differ from solids mainly in the introduction of viscosity, the role of viscosity is to be investigated in detail within this chapter.

Similar to what was done to shear viscous flow, a stress tensor can be written in terms of a hydrostatic pressure p and a viscosity stress tensor $\tilde{\sigma}_{ij}$ (Bhatia, 1967):

$$\sigma_{ij} = -p\delta_{ij} + \tilde{\sigma}_{ij} \qquad i, j = 1, 2, 3. \tag{3.26}$$

Recalling the expression of stress in an isotropic solid that is worth rewriting:

$$\sigma_{ij} = \lambda \varepsilon_{kk} \delta_{ij} + 2\mu \varepsilon_{ij} \tag{3.7}$$

$\tilde{\sigma}_{ij}$, the viscosity induced stress tensor, can also be rewritten in an analogous format:

$$\tilde{\sigma}_{ij} = \eta^o u_{kk}\delta_{ij} + 2\eta u_{ij} \tag{3.27}$$

where $u_{ij} = \frac{1}{2}\left(\frac{\partial u_i}{\partial x_j} + \frac{\partial u_j}{\partial x_i}\right)$, $U(u_i, u_j, u_k)$ is the flow velocity vector, giving $u_{kk} = divU$. η and η^o are called the first (shear) and second coefficients of viscosity.

Therefore, Equation 3.26 can be rewritten as:

$$\sigma_{ij} = -p\delta_{ij} + \eta^o divU\delta_{ij} + 2\eta u_{ij} \tag{3.28}$$

Let $i = j$, this equation is reduced to:

$$\sigma_{11} + \sigma_{22} + \sigma_{33} = -3p + 3\eta^o divU + 2\eta divU \tag{3.29}$$

To express the results by mean pressure yields:

$$\bar{p} = -\frac{1}{3}(\sigma_{11} + \sigma_{22} + \sigma_{33}) = p - \left(\eta^o + \frac{2}{3}\eta\right)divU \tag{3.30}$$

At this point, it is convenient to define the *bulk* or *volume viscosity*:

$$\zeta = \eta^o + \frac{2}{3}\eta \tag{3.31}$$

Substitute it back in Equation 3.30 produces an interesting equation:

$$\bar{p} = p - \zeta divU = p + \frac{\zeta}{\rho}\frac{D\rho}{Dt} \tag{3.32}$$

or

$$p - \bar{p} = \zeta divU = -\frac{\zeta}{\rho}\frac{D\rho}{Dt} \tag{3.33}$$

Comparing $\zeta = \eta^o + \frac{2}{3}\eta$ with the bulk modulus in solid elasticity $K = \lambda + \frac{2}{3}\mu$, a liquid's viscous properties are defined by two parameters, namely the already discussed shear viscosity η and now a bulk viscosity ζ. For hypothetical incompressible liquids, $divU = 0$, therefore ζ does not have any effect. But for the more general case of compressible liquids (or even a mixture of an incompressible liquid with highly compressible gas bubbles), ζ would correspond to the irrecoverable dissipation of deviation in pressure from the hydrostatic pressure, which is clearly shown in Equation 3.33.

With this newly defined bulk viscosity, the Navier-Stokes equation 3.21 can be upgraded to (Bhatia, 1967)

$$\frac{\partial^2 u_i}{\partial t^2} = \frac{\delta P}{\delta \rho}\frac{\partial}{\partial x_i}\left(\frac{\partial u_j}{\partial x_j}\right) + \frac{1}{\rho_0}\frac{\partial}{\partial t}\left\{\eta \nabla^2 u_i + \left(\frac{1}{3}\eta + \zeta\right)\frac{\partial}{\partial x_i}\left(\frac{\partial u_j}{\partial x_j}\right)\right\} \qquad 3.34$$

where the symbols have the same physical meanings as in equation 3.21 but with an additional bulk viscosity ζ. This bulk viscosity term at the end of this equation takes the volume change induced attenuation into account, hence it replaces the conventional Navier-Stokes equation, when compressible fluids are studied.

3.7 Wave propagation and Attenuation Associated with Bulk Viscosity

When it comes to fluid and attenuation, the damping mechanism in nature introduces a complex wave number and velocity as stated in Equation 3.24

$$v^* = \frac{\omega}{k^*} \qquad 3.35$$

where $k^* = k' - i\alpha$

It is convenient to define amplitude attenuation per wavelength α as:

$$\alpha_\lambda = \frac{2\pi\alpha}{k'} \qquad 3.36$$

If one integrates viscosities into the wave equation (replacing pressure in Equation 3.34) and assumes a plane harmonic wave solution $e^{i(\omega t - kx)}$, an attenuation-dispersion relation can be reached with a reference frequency ω_v (Bhatia, 1967):

$$\omega_v = \frac{K_s}{\zeta + \frac{4}{3}\eta} \qquad 3.37$$

where K_s is the bulk modulus under isentropic conditions.

The phase velocity and attenuation coefficient can be deduced:

$$v^2(\omega) = \frac{2K_s}{\rho}\frac{1 + (\omega/\omega_v)^2}{1 + \sqrt{1 + (\omega/\omega_v)^2}} \qquad 3.38$$

$$\alpha_\lambda(\omega) = \frac{\rho\pi}{K_s} \frac{\omega/\omega_\nu}{1+(\omega/\omega_\nu)^2} \nu^2 \qquad 3.39$$

where ρ is density of the medium in absence of the wave and ω_ν is the reference frequency. The above equations are Bhatia's attenuation and dispersion relations.

Back to the question proposed in section 3.3, can the attenuation be accounted for by both shear and bulk viscosities? The answer is still negative so far, because when frequency is not much smaller than characteristic frequency, the assumption that the stress tensor arising from the viscous forces depends only on the first space derivatives of the particle velocity. As a result, stress is no longer a linear function of these derivatives. The road to an acceptable explanation of lab measurements is only one step forward, and the theoretical work requires further effort to reach a practical level.

3.8 Viscoelastic Models

As noted in the previous section, theories of wave propagation in which moduli are assumed to be frequency independent constants, do not satisfactorily account for the attenuation phenomenon involved with viscous fluids. By introducing bulk viscosity and upgrading the Navier-Stokes equation, the stress tensor is supplemented, but is still not adequate to describe the complex physics lying behind. Since a further supplement of higher order of approximation to stress tensor from a purely theoretical point of view is too complicated to carry out at this point, another approach is adapted here to deal with the highly viscous materials.

Elastic and viscous properties of viscoelastic materials can be represented by springs and dashpots, respectively. A spring is a flexible elastic object used to store mechanical energy (resistant to displacement). There is no phase lag between stress and strain and the ratio between them is the Young's modulus. A dashpot is a viscous object, a damper which resists motion via viscous friction. It absorbs energy and hence, produces a phase lag between the applied stress and

effected strain. The applied stress on a dashpot is proportional to the strain rate, with shear viscosity as coefficient.

When complex materials are involved, researchers use certain combination of the two to symbolize the system. In such systems, *linearity* is present when the creep response and the load are separable, which is usually the case in small amplitude deformations (Nicolas, 1986). The two simplest cases used in illustration are the Maxwell and the Kelvin-Voigt's models. Such models are widely used in the study of characterizing homogeneous media via viscoelasticity (Ferry, 1980; Christensen, 1982). These models are based on combinations of a perfectly elastic component, represented by a perfectly elastic spring with a modulus G and a perfectly viscous component denoted by a dashpot characterized by a shear viscosity η.

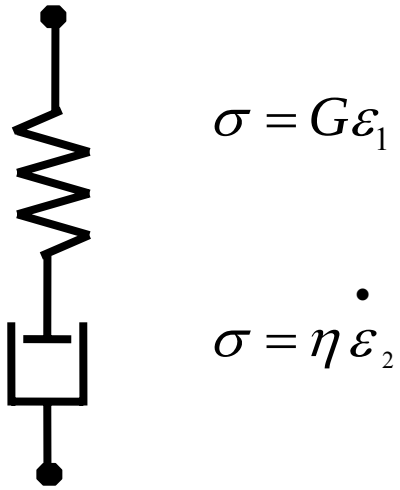

Figure 3.4 Maxwell's model represented by a perfectly elastic spring with a modulus G and a perfectly viscous component denoted by a dashpot characterized by a shear viscosity η, in series.

Maxwell's model (Figure 3.4) is composed of a spring (with modulus G) and a dashpot (with viscosity η) arranged in series. In this case application of a total stress across the system results in strains ε_1 and ε_2 in the elastic and the viscous components, respectively, while they too are subject to the same total stress σ. The following equations hold (Beyer, 1969; Ferry, 1980; Christensen, 1982):

$$\sigma = G\varepsilon_1 = \eta \dot{\varepsilon}_2 \tag{3.40}$$

$$\dot{\varepsilon} = \dot{\varepsilon}_1 + \dot{\varepsilon}_2 = \frac{\dot{\sigma}}{G} + \frac{\sigma}{\eta} \tag{3.41}$$

Above equation can be rewritten as:

$$\dot{\sigma} + \frac{\sigma}{\tau} = -\frac{\eta}{\tau}\dot{\varepsilon} \tag{3.42}$$

with the simplification $\tau = \frac{\eta}{G}$ which is the *relaxation time* of the Maxwell's model.

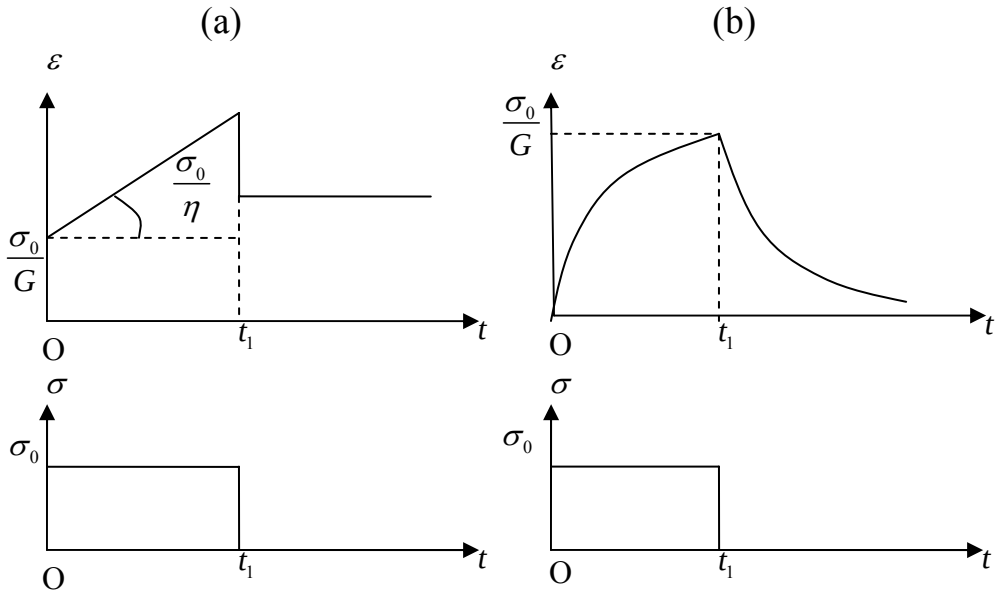

Figure 3.5 Creep test of (a) Maxwell and (b) Kelvin-Voigt's models

A *creep test* can be applied to Maxwell's model to illustrate the creep behavior (Figure 3.5a). A step function shaped stress is applied to the model at t = 0, and released at t_1. Substitute this stress into Equation 3.42, the solution is:

$$\varepsilon(t) = \frac{\sigma_0}{G} + \frac{\sigma_0}{\eta} t \qquad 3.43$$

This solution is also shown in the figure, at the moment of application of stress, the elastic element acts immediately, therefore an instant strain $\frac{\sigma_0}{G}$ is formed at t = 0. After t = 0, the viscous element is in play, and thus a linear creep is observed with a constant strain rate $\frac{\sigma_0}{\eta}$. At $t = t_1$, when the stress is released, the strain drops by $\frac{\sigma_0}{G}$ immediately and thereafter, remains at a constant value. The roles of elastic and viscous elements are clearly demonstrated in this creep test.

One can also imagine a *relaxation test* on Maxwell's model in which a constant strain is instead maintained; in this situation the stress decreases

(relaxes) exponentially as time increases. Substituting the strain in Equation 3.42 yields:

$$\sigma = \sigma_0 \exp\left(-\frac{t}{\tau}\right) \qquad 3.44$$

This equation also illustrates the physical meaning of the relaxation time τ. It is the time it takes for the stress to relax to 1/e of the initial level. The relaxation time is a unique characteristic of a static viscoelastic system.

The other illustrative viscoelastic model is the Kelvin-Voigt model that is composed of a spring (with modulus G) and dashpot (with viscosity η) in parallel (Figure 3.6).

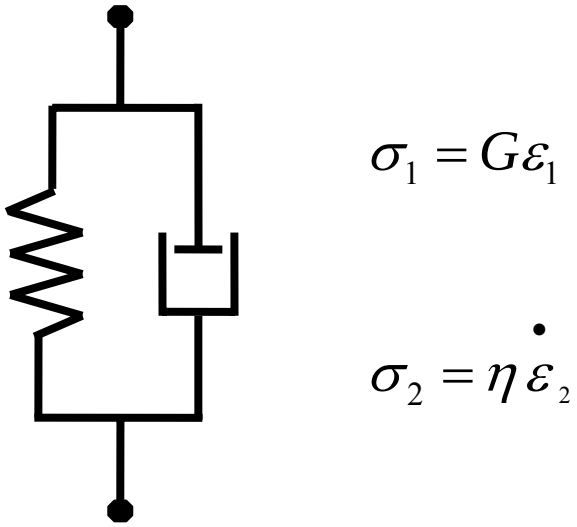

Figure 3.6 Kelvin-Voigt model represented by a perfectly elastic spring with a modulus G and a perfectly viscous component denoted by a dashpot characterized by a shear viscosity η, in paralell.

The constitutive equation can be obtained in a similar way as for Maxwell's model but in this case the stress is distributed across the two elements while they both must have the same strain and:

$$\sigma = \sigma_1 + \sigma_2 = G\varepsilon_1 + \eta\dot{\varepsilon}_2 \tag{3.45}$$

$$\dot{\varepsilon}_1 = \frac{\dot{\sigma}_1}{G} = \dot{\varepsilon}_2 = \frac{\sigma_2}{\eta} \tag{3.46}$$

where, η is viscosity and $\tau_v = \frac{\eta}{G}$, is the relaxation time.

When Kelvin-Voigt model is under creep test, the strain creep is shown in Figure 3.5b with the solution:

$$\varepsilon = \frac{\sigma_0}{G}\left[1 - \exp\left(-\frac{t}{\tau_v}\right)\right] \tag{3.47}$$

where τ_v is relaxation time for Kelvin-Voigt model. The relaxation time of the Maxwell and the Kelvin-Voigt models is a unique parameter that features the system, as it is defined by two parameters that characterize the two elements, and together with frequency, they set up certain limits to the viscoelastic system.

Chapter 4

Relaxation and Dynamic Spectroscopy

In previous chapters, the static property and wave behavior of a viscoelastic system are discussed. With traditional wave propagation in which moduli are assumed to be frequency independent, the phenomenon observed in the lab is different from that predicted by Navier Stokes equation. By introducing bulk viscosity, the stress tensor is supplemented, but still, not adequate to describe the complex physics lying behind. Since a further supplement to stress tensor from a purely theoretical point of view is too complicated to carry out at this point, another approach is adapted here to deal with the highly viscous materials in which interests are consistently growing both in the lab and the fields. The fundamental idea of this approach is the assumption that moduli are frequency-dependent. When harmonic waves are involved, the moduli and viscosities will take on a complex form in the frequency domain. This approach is employed in literature and some of the simulation satisfies the data from the lab. Before applying the complex parameters to the work in this thesis, it is beneficial to introduce Fourier transform and relevant concepts in the first section below.

4.1 Fourier Transform between Time and Frequency Domains

The Fourier transform, named after French mathematician Joseph Fourier[1], is a linear transformation that maps a time domain real function to frequency domain (in mathematics, domains do not require specific physical meanings). It works in such a way that a real time domain function is decomposed into continuous spectra in frequency domain, and can be resembled back to the same function in time domain if an inverse transformation is performed.

The time domain function and the Fourier transformed frequency domain function are called Fourier transform pairs in general, which are given by:

$$F(\omega) = \int_{-\infty}^{\infty} f(t)\exp(-i\omega t)dt$$
$$f(t) = \frac{1}{2\pi}\int_{-\infty}^{\infty} F(\omega)\exp(i\omega t)d\omega \qquad 4.1$$

where ω is angular frequency and t is time. Fourier transform can be viewed as an application of Hilbert transform[2] in mathematics.

There is a certain rule that links the Fourier transform pairs in mathematics, which is implicit. While in physics, it has a practical concern. In 1920s, Krönig and Kramers (1926) pointed out that, the real part of the electromagnetic index of refraction could be related to the Hilbert transform of the imaginary part. It is termed later as the well-known *Krönig-Kramers relation*, which is widely employed in other fields such as ultrasonic and biomedical measurements.

---

[1] **Jean Baptiste Joseph Fourier** (March 21, 1768 - May 16, 1830) was a French mathematician and physicist who is best known for Fourier series, which was first applied to study the heat flow. The Fourier transform established thereafter is also named in his honor. Fourier's contribution also includes the discovery of greenhouse effect in 1824.

[2] The **Hilbert transform** is named after the mathematician David Hilbert (January 23, 1862 – February 14, 1943). In the time domain, it is defined by a convolution between the Hilbert transformer $1/\pi t$ and a function f(t). The basic property of the Hilbert transform is the $\pi/2$ phase shift between the transform pair.

A general expression of Krönig-Kramers relation can be shown for a complex function f(ω), with real part $f_1(\omega)$ and imaginary part $f_2(\omega)$:

$$f(\omega) = f_1(\omega) + i f_2(\omega) \tag{4.2}$$

The relation between f_1 and f_2 can be written as:

$$f_1(\omega) = \frac{2}{\pi}\int_0^\infty \frac{\omega' f_2(\omega')}{\omega^2 - \omega'^2} d\omega'$$
$$f_2(\omega) = -\frac{2\omega}{\pi}\int_0^\infty \frac{f_1(\omega')}{\omega^2 - \omega'^2} d\omega' \tag{4.3}$$

The Krönig-Kramers relation features the bond between physical quantities that are fundamentally expressed through Hilbert transforms in a general understanding. Therefore, the real and imaginary parts of Fourier transform (Equation 4.1) are not independent of each other. The fact that real and imaginary parts of Fourier transform are linked to one another indicates that there is certain physical explanation lying behind.

Regarding the focus in this work, the dispersion and attenuation in lossy media are dependent on one another with respect to *causality*, which means a signal can not be received before it actually arrives.

To satisfy these relations in propagating waves, Nussenzveig (1972) showed that velocity and attenuation coefficient must be related via the Hilbert transform:

$$\frac{\omega}{c_p(\omega)} = \frac{\omega}{c_\infty} + H\{\alpha(\omega)\}$$
$$\frac{\alpha(\omega) - \alpha(0)}{\omega} = -H\left\{\frac{1}{c_p(\omega)} - \frac{1}{c_\infty}\right\} \tag{4.4}$$

where c_∞ is phase velocity at infinite frequency, and H stands for the Hilbert transform operator. It can be viewed as an application of Fourier transform and Krönig-Kramers relation.

4.2 Introducing Complex Stress, Strain and Moduli

In order to study the frequency-dependent properties of viscoelastic system, one could write the dilatational (n = 1) and deviatoric (n = 2) part of the stress and strain relations of isotropic media as:

$$\begin{aligned} &\sigma_{ij}(t) = \int_{-\infty}^{t} G^{n}(t-t')\dot{\varepsilon}_{ij}(t')dt' \\ &n=1 \quad i=j; \\ &n=2 \quad i\neq j. \end{aligned} \tag{4.5}$$

where G^n is a compliance that describes the system's viscoelastic behavior and this equation is usually called the *constitutive equation*. The physical interpretation of this equation is that the current stress is determined by the superposition of the responses to the complete spectrum of increments of strain.

In cases such as harmonic wave propagation, properties of viscoelastic materials could be different from static case due to dynamic loading. Suppose a sinusoidal strain of a viscoelastic media is resulted from a sinusoidal stress, which are usually written in exponential form in dynamic case (Beyer, 1969; Ferry, 1980):

$$\varepsilon(t) = \varepsilon_0 \exp(i\omega t) \tag{4.6}$$

where ε_0 is the maximum strain amplitude and ω is angular frequency.

Take Fourier transform of time domain stress (with Equation 4.6 substituted into Equation 4.5), a complex stress is given by:

$$\sigma_{ij}^{*}(\omega) = \int_{-\infty}^{\infty}\left[\int_{-\infty}^{t} G^{n}(t-t')\dot{\varepsilon}_{ij}(t')dt'\right]\exp(-i\omega t)dt \tag{4.7}$$

If $\exp(-i\omega t)$ is applied to the term inside the brackets, and further simplify it with $s = t - t'$, the following form of complex stress is obtained:

$$\sigma_{ij}^{*}(\omega)=\left[\int_{-\infty}^{\infty}G^{n}(s)\exp(-i\omega s)ds\right]\varepsilon_{0}t \tag{4.8}$$

Since the term in brackets is the Fourier transform of G(t) and the term outside the brackets is the Fourier transform of strain in Equation 4.6, then we can express stress and strain relation in frequency domain with a complex modulus G^{*}_{n}:

$$\sigma_{ij}^{*}(\omega)=G_{n}^{*}(\omega)\varepsilon_{ij}^{*}(\omega) \tag{4.9}$$

So far, the time domain stress and strain relation is converted into frequency domain.

In order to show further relations of the modulus, one can substitute harmonic strain (Equation 4.6) into constitutive equation (Equation 4.5), and separate the cosine and sine terms:

$$G_{n}^{*}(\omega)=\omega\int_{0}^{\infty}G^{n}(s)\sin(\omega s)ds+i\omega\int_{0}^{\infty}G^{n}(s)\cos(\omega s)ds \tag{4.10}$$

Thus the real and imaginary parts of complex modulus are:

$$\begin{aligned}G'(\omega)&=\omega\int_{0}^{\infty}G^{n}(s)\sin(\omega s)ds\\ G''(\omega)&=\omega\int_{0}^{\infty}G^{n}(s)\cos(\omega s)ds\end{aligned} \tag{4.11}$$

The physical quantity can be obtained by taking the real part of the complex quantity. In practical dynamic cases, since signals are composed of a variety of frequencies, it is convenient to express quantities and equations in a complex form, which will be assumed in later discussion.

Similar to the definition in time domain, the complex shear viscosity can be defined by the ratio of stress and strain rate, but now in frequency domain:

$$\eta^{*}(\omega)=\frac{\sigma^{*}(\omega)}{\dot{\varepsilon}^{*}(\omega)} \tag{4.12}$$

Compared to the definition of modulus (rewritten of Equation 4.9):

$$G^*(\omega) = \frac{\sigma^*(\omega)}{\varepsilon^*(\omega)} \tag{4.13}$$

The relation between shear modulus and shear viscosity can be obtained by employing simple Fourier transformation properties:

$$\eta^*(\omega) = \int_0^\infty G(s) e^{-i\omega s} ds = \frac{G^*(\omega)}{i\omega} \tag{4.14}$$

One can also write the above quantities in real and imaginary parts:

$$\begin{aligned} G^*(\omega) &= G'(\omega) + iG''(\omega) \\ \eta^*(\omega) &= \eta'(\omega) - i\eta''(\omega) \end{aligned} \tag{4.15}$$

Hence, following relations can be deduced:

$$\begin{aligned} G'(\omega) &= \omega\eta''(\omega) \\ G''(\omega) &= \omega\eta'(\omega) \end{aligned} \tag{4.16}$$

By definition, η', the real part of complex shear viscosity, denotes the viscous response of the material, therefore G", which is related to η', is called the loss modulus; while η'' denotes the elastic response and related G' is called the storage modulus.

Upon the establishment of complex notation, the complex shear modulus of Maxwell's model can be obtained: (Beyer, 1969):

$$G^*(\omega) = G'(\omega) + iG''(\omega) = G_\infty \left(\frac{\omega^2 \tau_s^2}{1 + \omega^2 \tau_s^2} + i \frac{\omega \tau_s}{1 + \omega^2 \tau_s^2} \right) \tag{4.17}$$

with relaxation time:

$$\tau_s = \frac{\eta}{G_\infty} \tag{4.18}$$

which characterizes such viscoelastic system to a large extent.

Substitute Equation 4.17 into Equation 4.14, the relation between complex

shear viscosity and complex shear modulus of Maxwell's model is given by:

$$\eta^*(\omega) = \eta'(\omega) + i\eta''(\omega) = \frac{G^*(\omega)}{i\omega} = G_\infty \tau_v \left[\frac{1}{1+\omega^2\tau_v^2} - i\frac{\omega\tau_v}{1+\omega^2\tau_v^2} \right] \quad 4.19$$

As the shear viscosity is related to Maxwell's model in previous section, bulk viscosity and bulk modulus can also be related to Kelvin-Voigt model. As derived by the same author (Beyer, 1969), one could do a Fourier transform and reaches the following relation:

$$K^*(\omega) = K'(\omega) + iK''(\omega) = K_0 + (K_\infty - K_0)\left(\frac{\omega^2\tau_v^2}{1+\omega^2\tau_v^2} + i\frac{\omega\tau_v}{1+\omega^2\tau_v^2} \right) \quad 4.20$$

where K_0 is the relaxed modulus when $\omega = 0$, the unrelaxed modulus K_∞ denotes bulk modulus at infinite frequency. τ_v is the bulk relaxation time of the material:

$$\tau_v = \frac{\zeta}{K_\infty - K_0} \quad 4.21$$

And substituting Equation 4.20 to 4.14 yields the relation of bulk viscosity:

$$\zeta^*(\omega) = \zeta'(\omega) + i\zeta''(\omega) = \frac{K^*(\omega)}{i\omega} = \frac{(K_\infty - K_0)\tau_v}{1+\omega^2\tau_v^2} - i\left(\frac{K_0}{\omega} + \frac{(K_\infty - K_0)\omega\tau_v^2}{1+\omega^2\tau_v^2} \right) \quad 4.22$$

4.3 Attenuation from a Relaxation Approach

In analog to Equation 3.17, it is convenient to define a complex modulus with bulk and shear influence additive:

$$M^* = K^* + \frac{4}{3}G^* = M' + iM'' \tag{4.23}$$

Then, the compressional wave velocity and attenuation coefficient are defined by (Bhatia, 1967):

$$V_p^2 = M'/\rho$$
$$\alpha_{\lambda p} = M''\pi/\left(\rho V_p^2\right) \tag{4.24}$$

Similarly, shear wave and attenuation coefficients are defined by:

$$V_s^2 = G'/\rho$$
$$\alpha_{\lambda s} = G''\pi/\left(\rho V_s^2\right) \tag{4.25}$$

At low viscosity, where $\omega\tau_s << 1$, the above formula can be reduced to the relation we saw before:

$$V_s^2 = 2\omega G_\infty \tau_s/\rho = 2\omega\eta/\rho \qquad \alpha_{\lambda s} = 2\pi \tag{4.26}$$

While at high viscosity, where $\omega\tau_s >> 1$, shear wave velocity and attenuation law can be reduced to:

$$V_s^2 = G_\infty/\rho \qquad \alpha_{\lambda s} \approx \pi/\left(\omega\tau_s\right) \tag{4.27}$$

It indicates that the attenuation is small at high frequency due to the liquid's solid like properties, and the phase velocity is maintained constant throughout all frequencies.

Chapter 5

Illustrative Simulations of Attenuation

In this chapter, some illustrative of the effects of attenuation and dispersion are examined. The first section deals with commonly employed attenuation models in seismology. The second section looks at the attenuation in visco-elastic models including the bulk viscosity.

5.1 Seismic Attenuation Models

As stated in section 2.4, a number of mechanisms have been proposed in literature to address attenuation and dispersion in earth materials. However, these specifically developed attenuation / dispersion mechanisms often give way to empirical formulations in many cases because the viscous effects overlap in frequencies and this undermines the validity of the individual mechanisms. A common feature of the many proposed formulations in this area is that most of them fall in a nearly linear relation between the attenuation coefficient and the frequency (seismic band).

In cases where harmonic waves are involved (see Chapter 4), the elastic moduli are no longer constants but become time convolution operators (Ben-Menahem and Singh, 1981; Fabrizio and Morro, 1992; Gurtin and Herrera, 1965; Carcione, 2001). After applying a Fourier transform with respect to time, the elastic moduli become complex functions of frequency. This results in a complex propagation velocity (or wave number) which gives rise to attenuation and dispersion:

$$k^*(\omega) = \frac{\omega}{c^*(\omega)} = \frac{\omega}{c_p(\omega)} - i\alpha(\omega) \qquad 5.1$$

where k* is the complex wave number, c_p is phase velocity, α is the attenuation coefficient per meter, and ω is the angular frequency.

In order to study attenuation and dispersion, a first understanding of how they influence propagating waveforms is useful. After that, one can go further to study how a waveform evolves as it propagates away from the source, and how the phase and amplitude spectra look appear.

For the sake of illustration, listed below are several theoretical models that are commonly used in modeling solid earth materials. All the models assume causality[1] except for Kolsky's (Kolsky, 1956; Futterman, 1962). Although a real pulse propagating in an attenuating medium must be causal (Futterman, 1962), non-causal mathematics does not limit the use of Kolsky's model. The models used here include Kolsky's, Azimi's and Cole-Cole's (1941). Compared to other models which are constrained tightly by memory variables (c_∞, a, a_3, etc.), the Cole-Cole model is more adaptable because one is given the freedom to choose different exponentials according to different situations.

These models are described:

Kolsky (*Kolsky, 1956*; *Futterman, 1962*)

Kolsky's model assumes strict linear relation between the attenuation coefficient $\alpha(\omega)$ and frequency over the range of measurement. It is free to choose a reference frequency ω_r, following the phenomenological criterion that it should

[1] Causality refers to a system's response (or output, effects) and its cause. A causal system is a system whose output depends only on the current and previous input; it has nothing to do with "future" events (non-causal). In seismology, causality is usually referred to when dealing with travel time: a signal will not arrive before it arrives.

be small but nonzero. In the seismic industry, the dominant frequency is often chosen as ω_r.

$$\frac{1}{c_p(\omega)} = \frac{1}{c_r} + \frac{1}{\pi c_r Q_r} In\left|\frac{\omega_r}{\omega}\right|$$
$$\alpha(\omega) = \frac{|\omega|}{2c_r Q_r} \qquad 5.2$$

where c_r, Q_r are the values of the phase velocity and the approximate Q at the reference frequency ω_r

Power law model (Azimi's 1st model)

The power law model proposed by Strick (1967) and Azimi et al. (1968) assumes that the attenuation is proportional to $|\omega|^{\gamma}$, where γ is an empirical number that to be determined by experimental data. For $0 < \gamma < 1$ this model satisfies the Kramers-Krönig relations, which gives (with $\beta = 1 - \gamma$)

$$\frac{1}{c_p(\omega)} = \frac{1}{c_\infty} + \alpha|\omega|^{-\beta}\cot\left(\frac{\pi}{2}\beta\right)$$
$$\alpha(\omega) = a|\omega|^{-\beta} \qquad 0 < \beta < 1 \qquad 5.3$$

The power law will satisfy causality only for power exponents less than one. For exponents between 1 and 2, Cole and Cole model may be employed. This power law model is also called Azimi's first model.

Azimi's 2nd model (Azimi et al. , 1968)

$$\frac{1}{c_p(\omega)} = \frac{1}{c_\infty} - \frac{2a}{\pi}\frac{In\left(a_2|\omega|\right)}{1 - a_2^2\omega^2}$$
$$\alpha(\omega) = \frac{a|\omega|}{1 + a_2|\omega|} \qquad 5.4$$

where c_∞ being the phase velocity at infinite frequency, a and a_2 are two empirically derived parameters.

Azimi's 3rd model (Azimi et al. , 1968)

$$\frac{1}{c_p(\omega)} = \frac{1}{c_\infty} + \frac{a a_3 \sqrt{|\omega|}}{1 + a_3^2 |\omega|} - \frac{2a}{\pi} \frac{In(a_3^2 |\omega|)}{1 - a_3^4 \omega^2}$$
$$\alpha(\omega) = \frac{a|\omega|}{1 + a_3 \sqrt{|\omega|}} \qquad 5.5$$

where c_∞ being the phase velocity at infinite frequency, a and a_3 are two empirically derived parameters

Cole and Cole (1941):

Cole and Cole model was proposed for dielectrics in 1941, and adapted to viscoelastic media by Jones (1986). The complex modulus is expressed as:

$$M(\omega) = M_0 \frac{1 + (-i\omega\tau_\varepsilon)^\beta}{1 + (-i\omega\tau_\sigma)^\beta} \qquad 5.6$$

where β is exponential parameter which is less than 1, τ_ε , τ_σ are the relaxation times for stress and strain, respectively. For $\tau_\varepsilon = \tau_\sigma$ or $\beta = 0$, this corresponds to an elastic solid. For viscoelastic materials, $\tau_\varepsilon < \tau_\sigma$ is usually assumed, and $0 < \beta \leq 1$. Then the phase velocity and attenuation coefficient can be approximated as (*Casula and Carcione , 1992*):

$$\frac{1}{c_p(\omega)} \approx \frac{1}{c_0} \left[1 - \frac{\beta |\omega\tau_r|^\beta}{Q_c} \frac{\cos\left(\frac{\pi}{2}\beta\right) + |\omega\tau_r|^\beta}{1 + |\omega\tau_r|^{2\beta} + 2|\omega\tau_r|^\beta \cos\left(\frac{\pi}{2}\beta\right)} \right]$$
$$\alpha(\omega) \approx \frac{\beta |\omega\tau_r|^{1+\beta}}{c_0 Q_c \tau_r} \frac{\sin\left(\frac{\pi}{2}\beta\right)}{1 + |\omega\tau_r|^{2\beta} + 2|\omega\tau_r|^\beta \cos\left(\frac{\pi}{2}\beta\right)} \qquad 5.7$$

Simulation is done with these models to give an idea how different these models are from one another and how the attenuation / dispersion laws look like with respect to frequency. The parameter sets in use are listed below:

Table 5.1 Parameters Used in the Simulation via 5 Attenuation Models*

Models	Parameters			
	Reference velocity c_∞ (m/s)	Reference Q	Coefficient a	Miscellaneous
Kolsky	2632 (c_r)	100 (Q_r)	N/A	$\omega_r = 2\pi\times10^6$ (rads)
PowerLaw	2632	N/A	5×10^{-5}	$\beta = 0.228$
Azimi 2nd	2632	N/A	2.4×10^{-6}	$a_2 = 1\times10^{-7}$
Azimi 3rd	2632	N/A	2.5×10^{-6}	$a_3 = 2\times10^{-4}$
ColeCole	2410 (c)	0.9348 (Q_c)	N/A	$\beta_0 = 0.12$, $\tau = 1./(39500)$ (sec)

*Ursin and Toverud (2002)'s choice used as reference

Figure 5.1 is a plot of attenuated waveforms with above models, with individual waveforms in the left panel and plotted together (stack) in the right panel. The original signal is a delta function (spike) positioned at x = 0, with normalized amplitude 1 and these attenuated waveforms are modeled at position x = 2 m. As one can observe from this plot, the waveforms are more or less similar, with amplitude variation up to parameterization. The Kolsky model yields an early arrival, which does not comply with causality.

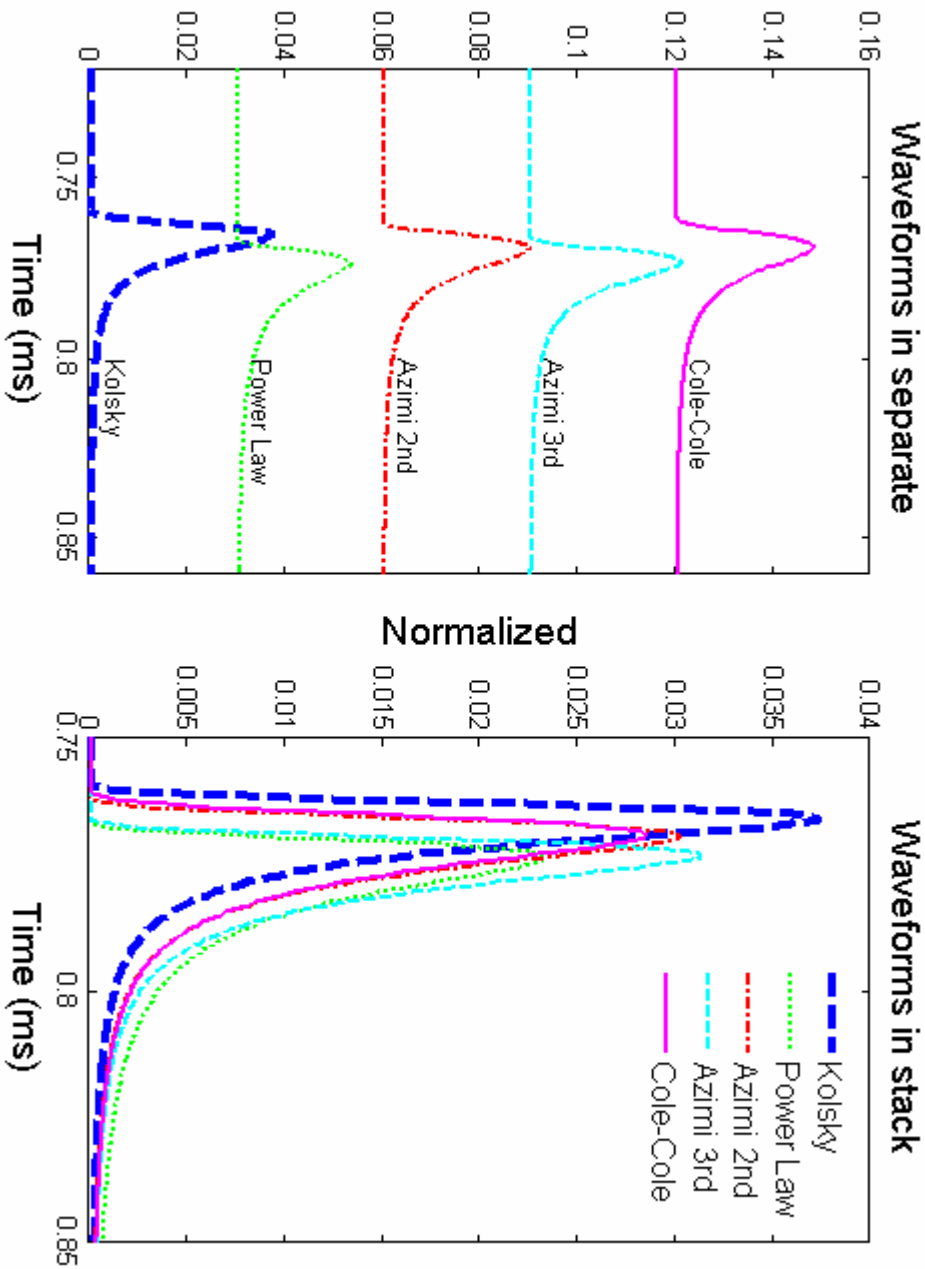

Figure 5.1 Attenuated waveforms based on different attenuation models (left panel: separate waveforms; right panel: stacked waveforms)

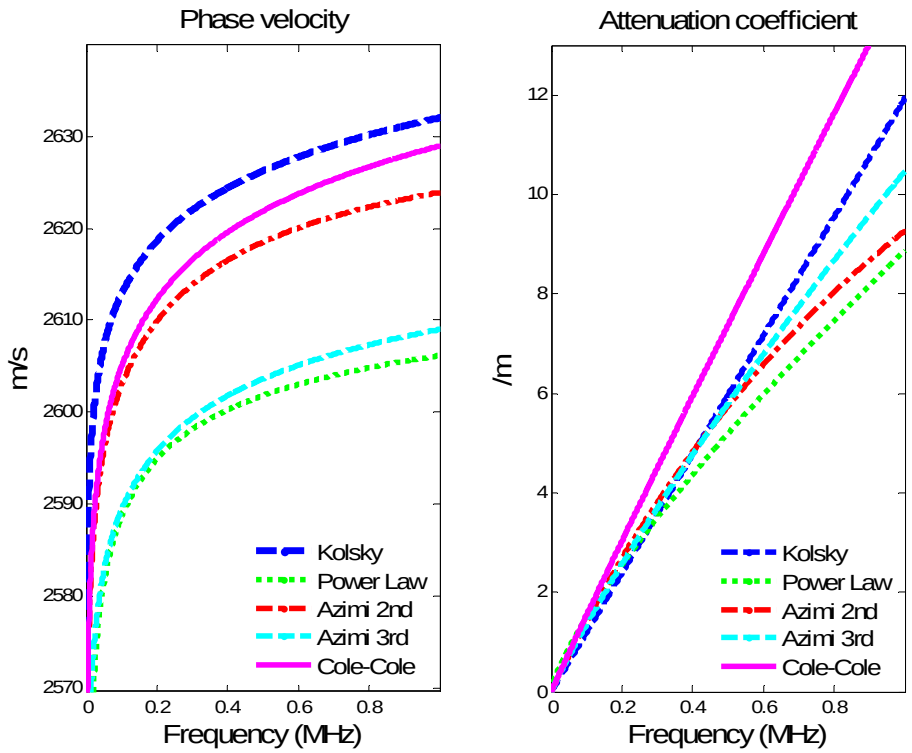

Figure 5.2 Phase velocity and attenuation coefficient of seismic attenuation models as functions of frequency

Figure 5.2 shows the attenuation and dispersion in the frequency domain up to ultrasonic frequency. At seismic ranges, all models behave similarly (Ursin and Toverud, 2002). But when frequency increases up to 1MHz, the difference is increasing. This means that these models may deviate from linear relation and wave behavior is therefore more complicated. Also can be observed is that, phase velocities approach a certain limit value as frequency increases, while attenuation coefficient increases nearly linear, with no sign of reaching any limit other than the Azimi and the power law models. This nearly linear relation between α and frequency means that Q is essentially constant. But for viscoelastic materials, such as melt glass, there could be a reference frequency beyond which the media would act like a solid, therefore the attenuation coefficient could be different.

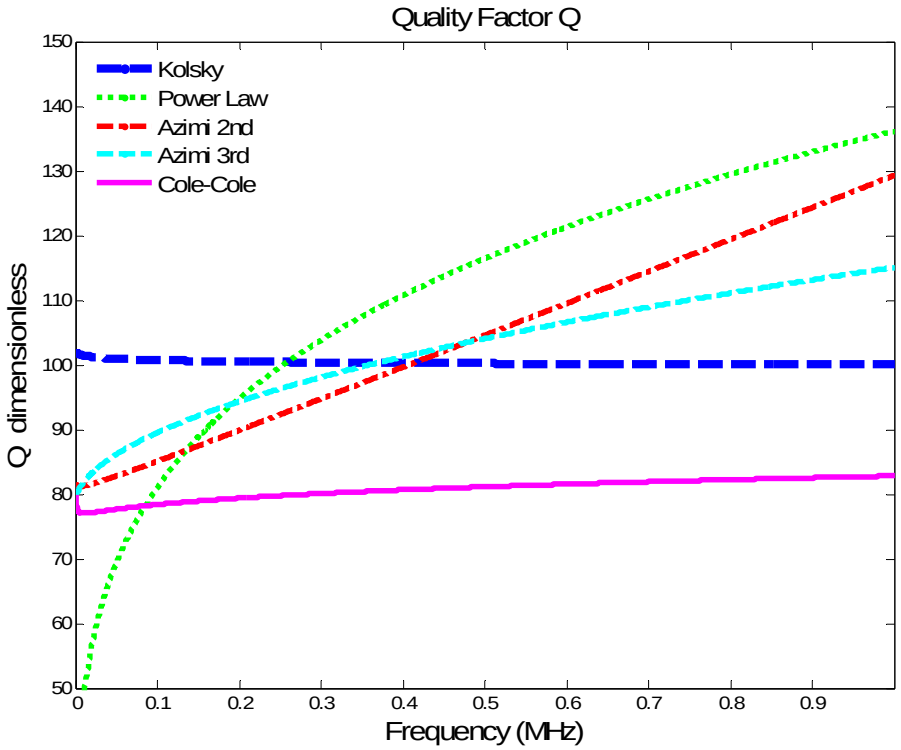

Figure 5.3 Q values of different seismic attenuation models

In Figure 5.3, Q values of these 5 models are calculated by Equation 2.4.

The Kolsky and Cole-Cole models indicate a nearly constant Q, while in Azimi's 2nd model Q is linear increasing. Azimi 3rd and the power law models show exponential increases. Nevertheless, Q values fall within 70 to 140 above 50 kHz. The Kolsky and Cole-Cole models indicate nearly frequency independent relations, while the remaining three indicate less attenuation at high frequency.

Since these models have little bond to physical parameters, it must be remembered that these are all phenomenological models that are useful for description but may have little link to real physical mechanisms of attenuation, the fitting between the model and real data is up to the selection of the memory variables, which yields little information regarding the microscopic properties of

rocks. Therefore, the application of these models to simulate a real case is limited to large scale, dry and macro-scopic study, such as in seismology, but helps little in the lab on specific core samples.

As point out by the same authors (Ursin and Toverud, 2002), the Standard Linear Solid model[2] behaves differently from the other models as the frequency goes to zero or infinity. This property may indicate the adaptability of viscoelastic models to model fluid saturated materials, as we see how frequency is involved in wave attenuation/dispersion from previous chapters.

Further simulation is carried out (Figure 5.4) to provide more insight on waveform evolution, phase velocity / dispersion, Q values, amplitude and power spectra. The purpose of this simulation is to obtain a preliminary idea of how attenuation-dispersion relation affects waveforms and how spectra vary with respect to frequency. Since several of the aforementioned models behave similarly in certain frequency bands, simulations are carried out on only one of them, which is Azimi's 2nd model. The corresponding attenuation law is applied to a step function (spike) which is originally positioned at x = 0, then the initial signal propagates along x axis and attenuated waveforms are modeled at different locations (x) from 0.3 meter to 3 meters in a step of 0.3 meter. This simulation imposes Azimi's 2nd attenuation / dispersion law (Figure 5.2，dot-dashed curves) to the initial spike, in which frequency is accounted up to 1 MHz. In Figure 5.4, waveforms are plotted in the time domain with original spike plotted in the sub-panel.

[2] Standard Linear Solid model is a viscoelastic model that consists of a spring in series of a parallel couple of another spring and a dashpot. Description of viscoelastic elements – spring and dashpot is detailed in Chapter 3.

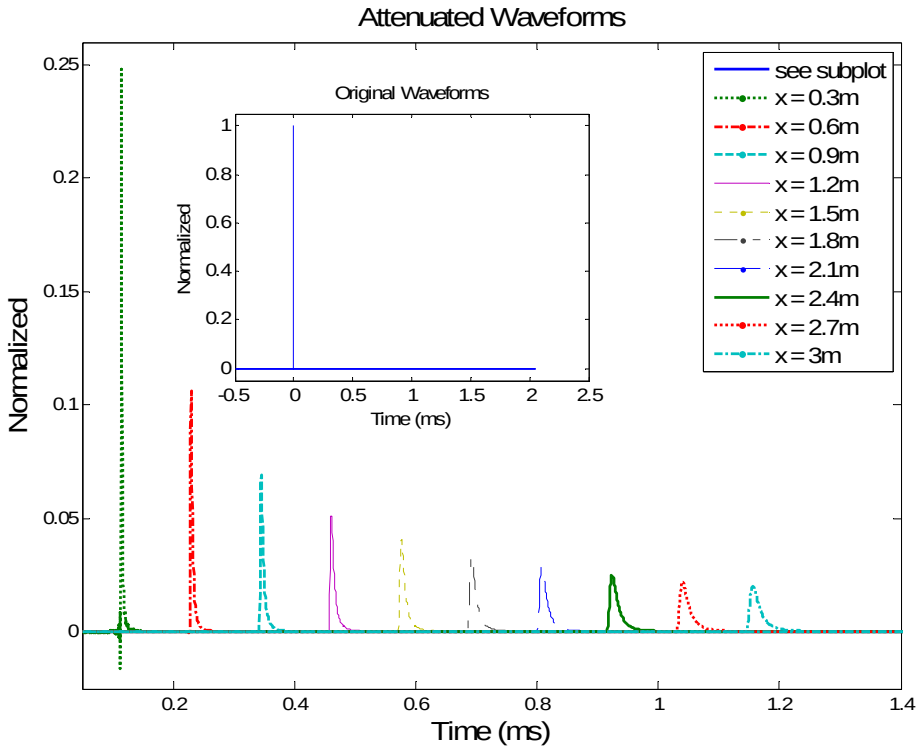

Figure 5.4 Propagating waveforms based on Azimi's 2nd attenuation law (original waveform is a spike located at x = 0 m. The remaining waveforms are modeled at different locations shown in the legend)

The chosen parameters are the same as given in Table 5.1. The waveforms in Figure 5.4 show clearly the dispersed pulse over a longer and longer time span as the distance shifts away from the source, and the amplitude decays in an exponential manner. Phase spectra and power spectra at each location are plotted in Figure 5.5.

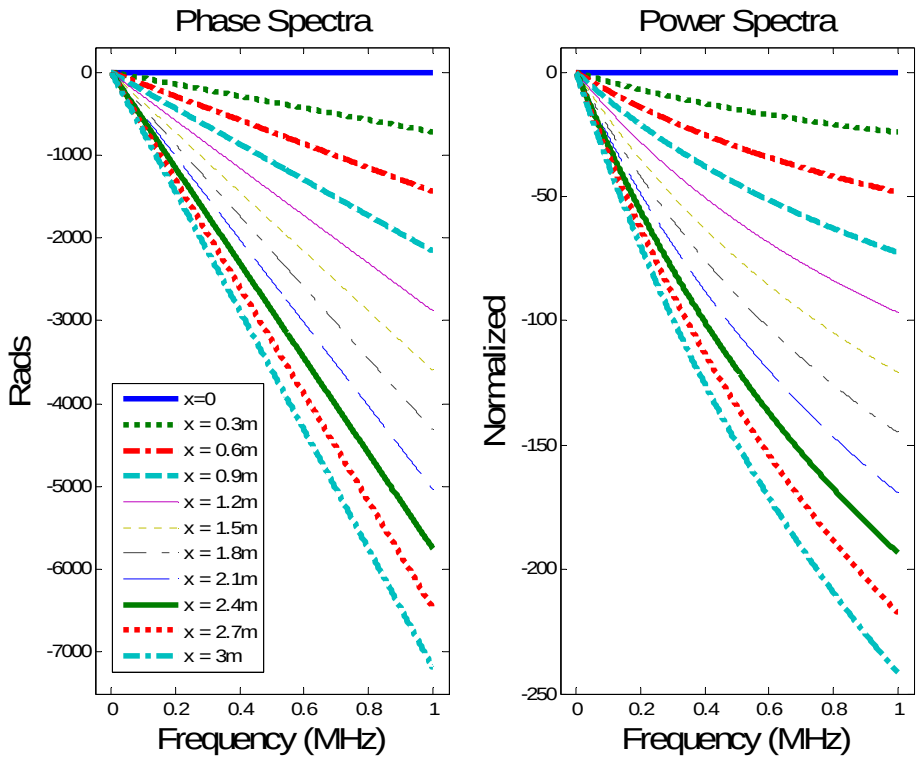

Figure 5.5 Phase and power spectra of a series of waveforms based on Azimi's 2nd attenuation law

Since the simulation is on ideal mathematical attenuation law, the power and phase of initial spike are maintained at zero for all frequencies. At distance other than the origin, the phase is nicely unwrapped and maintains a good linear relation with frequency, while the power spectra are in an exponential decay. This indicates that energy loss is significant at higher frequencies, where as the frequency approaches zero, the loss is at minimum.

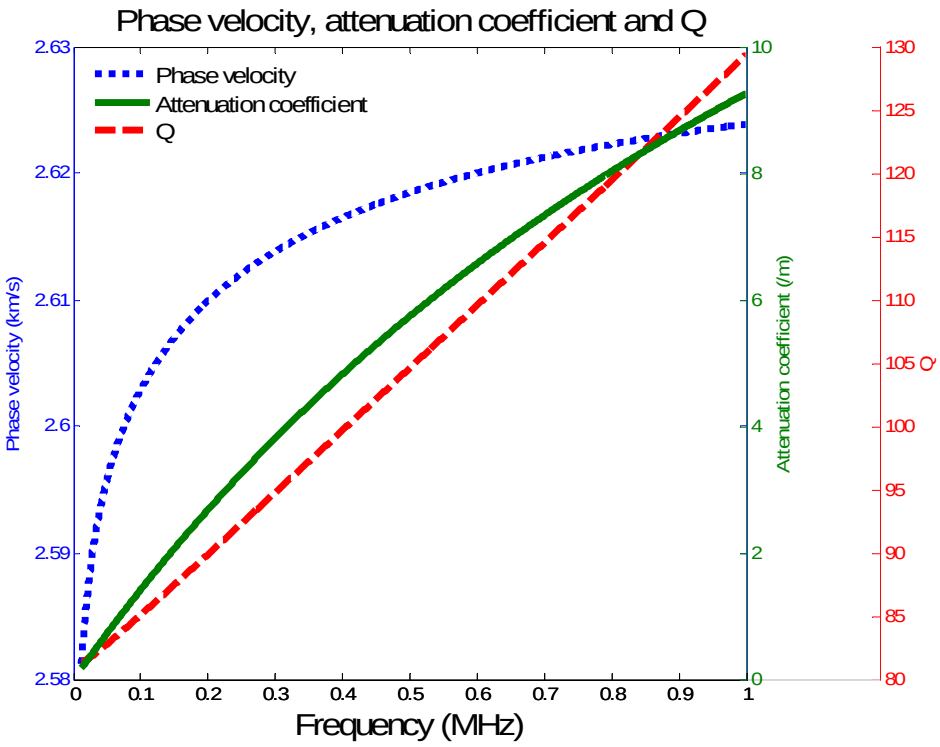

Figure 5.6 Phase velocity, attenuation coefficient and quality factor Q based on Azimi's 2nd attenuation law

In the above figure, the phase velocity, the attenuation coefficient and the quality factor Q are plotted together. Since a_2 is only 10^{-7}, a nearly linear relation is observed on the attenuation coefficient as discussed in previous paragraphs; an increasing velocity with less and less increasing rate is also found. This means higher frequencies travel faster than lower - for high frequencies above 200 kHz, the velocity variation is much less than at low frequencies, only a difference of less than 0.1% is observed in this case. This trend is common on Azimi's 2nd model if a small a_2 is assumed.

The quality factor Q is calculated simply by Equation 2.4 with the parameters employed in this simulation, a nearly linear increasing Q with frequency is shown and the maximum Q = 129 is reached at f = 1MHz. For the remainder of

frequencies, Q falls between 80 and 130. These results may represent some rock properties in the upper crust, however, one would expect lower Q values, higher attenuation coefficient and a much more variable phase velocity when fluid is present.

5.2 Viscosity Effect via Maxwell's Model

In this section, the mechanism of attenuation within the fluids themselves will be examined. Near perfect fluids can be represented by Maxwell's model (section 3.8) in ideal conditions (homogenous, Newtonian, laminar flow). Thus, the effects of viscosity are simulated with Maxwell's model to illustrate how shear viscosity affects attenuation and dispersion curves. As discussed in Chapter 4, one would expect a relaxing modulus (Equation 4.13) rather than a constant. Parameters used to model shear viscosity effects are listed in Table 5.2.

Table 5.2 Parameters chosen to model shear viscosity effects

Parameter	Symbol	Value
Temperature (℃)	T	15, 20, 25
Reference Shear modulus (GPa)	G_∞	1.00×10^{10}
Shear viscosity (Pa.s)	η	8.62×10^{5}, 6.59×10^{5}, 5.06×10^{5}*
Density (kg/m^3)	ρ	2600.1, 2599.8, 2599.5*

* Calculated from Beggs and Robinson's relation(1975)

Shear modulus, phase velocity, attenuation coefficient and 1/Q are calculated by Equation 4.18, Equation 4.26 and Equation 2.4; the results are shown in the following plot (Figure 5.7). The independent X axis is frequency in log scale, up to 1 MHz.

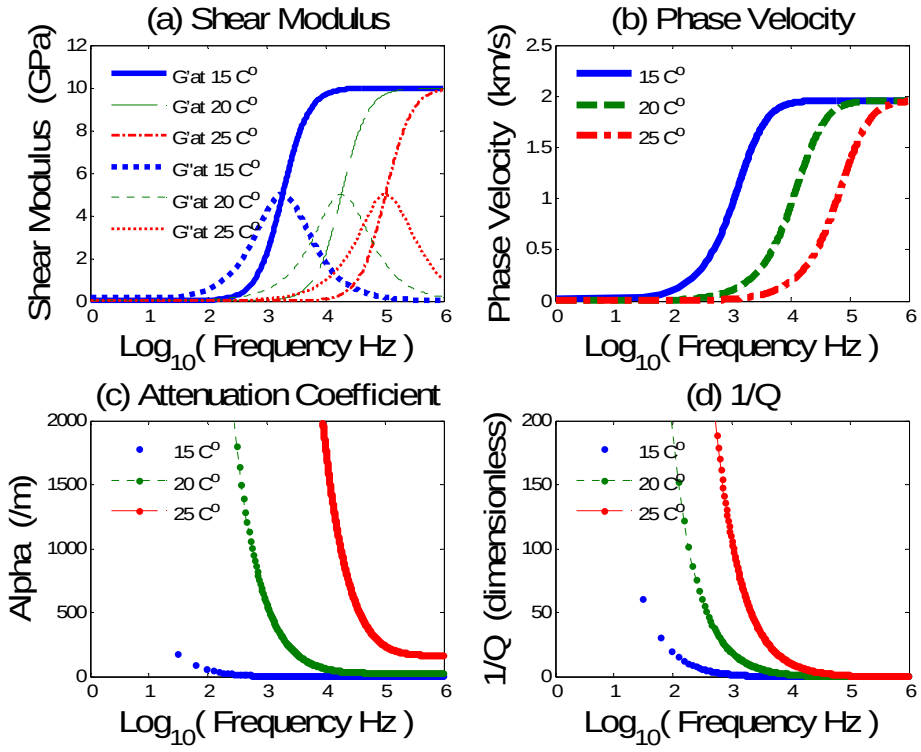

Figure 5.7 Effects of shear viscosity on shear modulus (a), phase velocity (b), attenuation coefficient (c) and Q (d) with shear viscosity 8.62×10^5 Pa.s at 15℃, 6.59×10^5 Pa.s at 20℃, 5.06×10^5 Pa.s at 25℃ (Beggs and Robinson's relation, 1975). X axis is frequency in log scale up to 1 MHz.

As is shown, the shear viscosity at temperatures of 15, 20, 25 ℃ in an oil are used to simulate the shear viscosity effect on the shear modulus, the phase velocity, the attenuation coefficient and Q. Unlike the simulation in the previous section, all four parameters display frequency-dependent relaxation. The phase velocity is no longer nearly constant over a wide frequency range, nor does the attenuation coefficient maintain a linear relation with frequency. Shown in Figure 5.7 a, at low temperature (high viscosity), take 15 ℃ for example, the real part of the shear modulus remains at a constant value over 1/3 of the whole frequency band (10^4~10^6 Hz), while the imaginary part essentially vanishes in the same band.

Such a modulus gives an almost constant velocity at the same frequency band (Figure 5.7 b), which is similar to an elastic case. Consequently, the attenuation coefficient is a small number at such frequencies (Figure 5.7 c) while 1/Q (attenuation) is small over this band, but is very high for low frequencies (Figure 5.7 d). The high attenuation at low frequencies complies with the common knowledge that the S wave does not propagate in liquids, but as indicated by this simulation, the S wave may propagate through at high viscosity and high frequency. As the temperature increases, the viscosity drops, and the frequency band of constant modulus is shortened, which undermines the propagation of the S wave.

By simulating with Maxwell's model, the effect of shear viscosity and the behaviors of dynamic waves (frequency dependency, relaxation) are illustrated. A lower shear viscosity shifts the shear modulus, the phase velocity, the attenuation coefficient, and 1/Q to higher frequency (more obvious in Figure 5.7 a,b). For each viscosity level, there exists a frequency band where the shear modulus, the phase velocity, the attenuation coefficient, and 1/Q remain essentially constant; and there is also a frequency band where these parameters display highly frequency dependent behaviors (10^2~10^4Hz, Figure 5.7 a,b). For the first two parameters, this band is limited (Figure 5.7 a,b), while for the last two parameters, this band is located at low frequency range (Figure 5.7 c,d). This may indicate that at certain temperature and pressure (thus a certain shear viscosity), high attenuation presents at low frequency (e.g. seismic band) while little attenuation at extremely high frequency (e.g ultrasonic band). This property is related and can be explained by the behaviors of elements in Maxwell's model. When the frequency is extremely high, only the elastic element dominates, and thus little attenuation is observed. In contrast, when the frequency drops to a low level, the viscous element dominates and the energy is lost due to viscous flow. It is also

worth pointing out that at frequency extremes, velocity and modulus have the same maximum and minimum regardless of the change in shear viscosity.

5.3 Bulk Viscosity Effect via Burger Model

In last section, the attenuation of a harmonic wave within fluids was examined via Maxwell's model with emphasis on the effects of the shear viscosity only. However, as discussed in Chapter 3, the bulk viscosity may also have effects on attenuation and dispersion. This section is devoted to examine the role of bulk viscosity by employing Burger's model of viscoelasticity (Green and Cooper, 1993).

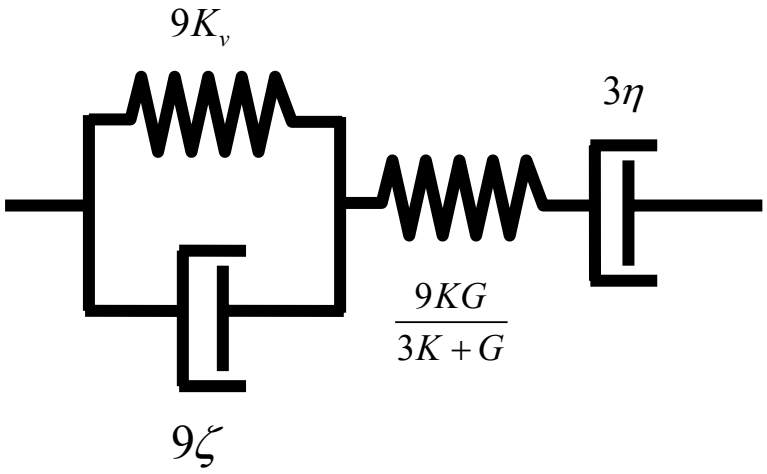

Figure 5.8 Burger model with four elements representing bulk （ζ）, shear （η） viscous response and elastic （K, G）, anelastic (K_v) response respectively. After Green and Cooper, 1993.

Compared to the Maxwell or the Kelvin-Voigt models, Burger's model is an integrated model which can include both shear and bulk mechanisms. Physical

parameters such as moduli and viscosities can be related to Burger model's elements. Figure 5.8 shows Green and Cooper (1993) derived results. They presented several viscoelastic models to study the size adjustment of melt-bearing triple-grain junction. In addition, an anelastic dilatation modulus K_v is introduced, which is associated to the total irrecoverable volume adjustment. The creep compliance of Burger's model is (Green and Cooper, 1993):

$$J(t) = \frac{3K + G}{9KG} + \frac{1}{3\eta}t + \frac{1}{9K_v}\left(1 - e^{-\frac{K_v}{\zeta}t}\right) \qquad 5.8$$

where K and G are the bulk and the shear modulus, K_v is the anelastic dilatation modulus, and η , ζ are the shear and the bulk viscosities respectively. To apply this model to earth materials, data on bulk viscosity and anelastic dilatation modulus are needed, but in most cases, these parameters are not adequately studied. Hence，simulation is carried out to shed light on future laboratory experiments.

In order to obtain a preliminary understanding of how bulk viscosity affects wave properties, dynamic simulations are performed on a wide variation of bulk and shear viscosity ratios. The relation between modulus, phase velocity and attenuation coefficient can be adapted from Equations 4.21, 4.25 and 2.4. The chosen parameters are listed in Table 5.3, which are estimated by Green and Cooper (1993) from flexure creep test.

From Figure 5.9 to Figure 5.12, bulk modulus K, phase velocity V_p, attenuation coefficient α_p and quality factor Q_p, as functions of frequency are plotted. Concerning S wave properties, a varying K_v or ζ does not affect V_s, Q_s nor $G^*(\omega)$, provided the values have realistic meanings.

Table 5.3 Parameters chosen to model bulk viscosity effects

Parameter	Symbol	Value
Temperature (℃)	T	1120*
Pressure (MPa)	P	13.8*
Bulk modulus (GPa)	K	9.08×10^{10}*
Anelastic modulus (GPa)	K_v	2.92×10^{8} *
Shear modulus (Gpa)	G	6.49×10^{10} *
Shear viscosity (Pa.s)	η	1.00×10^{12}
Bulk / shear viscosity ratio	R	10^{4}, 10^{2}, 1, 10^{-2}, 10^{-4}, 0
Density (kg/m^3)	ρ	3200 *

* Green and Cooper's choice (1993)

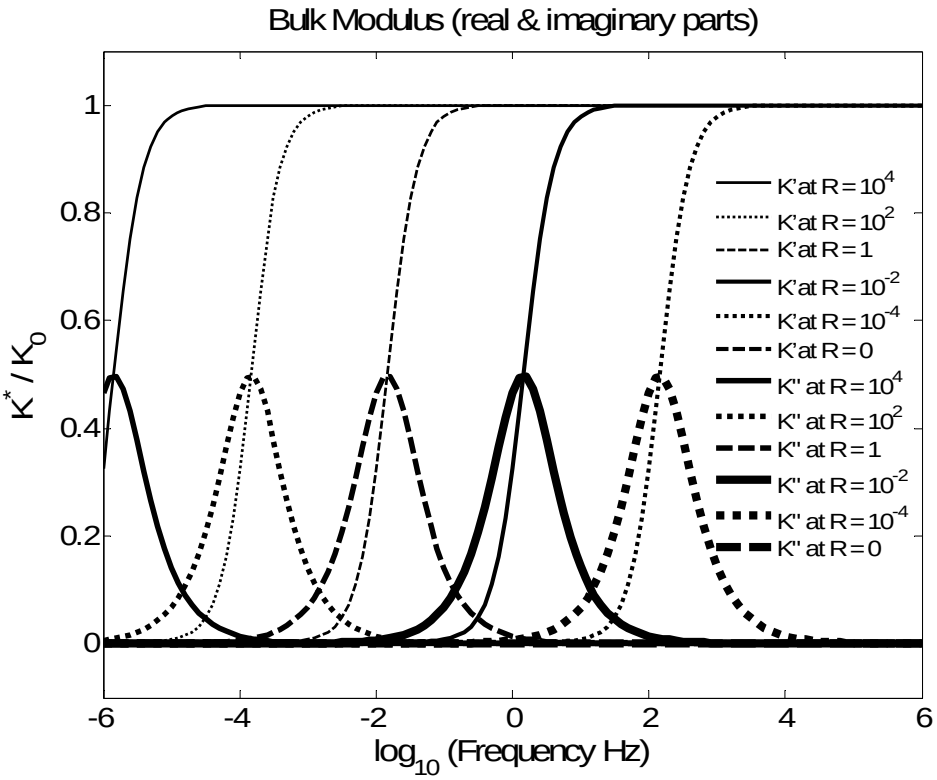

Figure 5.9 Effects of bulk viscosity on bulk modulus (real and imaginary parts of bulk modulus are normalized by maximum value K_0). Viscosity ratio R is simulated from 0 to 10^4.

As is shown in Figure 5.9, the bulk modulus dispersion relation displays a pattern similar to the shear modulus (previous section). A high R = ζ / η ratio shifts both the real and the imaginary parts of bulk modulus to lower frequency; or equivalently, broadening the regime over which the material behaves elastically (constant real part and a zero imaginary part). At a characteristic frequency $f_r = (K + K_v)/(2\pi\varsigma)$, the real and imaginary parts reach the same value: 0.5 K_0 (maximum of the imaginary part). This means half of the energy is stored while the other half is lost at this frequency. Below this characteristic frequency, the imaginary part is greater than the real part, and the viscous mechanism

dominates the system, which results in strong dispersion and attenuation.

A special case is when bulk viscosity is zero, then the imaginary part of bulk modulus will be zero for all frequencies, while the real part remains a small constant for all frequencies (not very obvious in Figure 5.9a). By simulation on different bulk / shear viscosity ratios, it is shown that the assumption of constant bulk modulus is applicable only if bulk viscosity is negligible, which is questionable in cases of molten materials or fluids saturation.

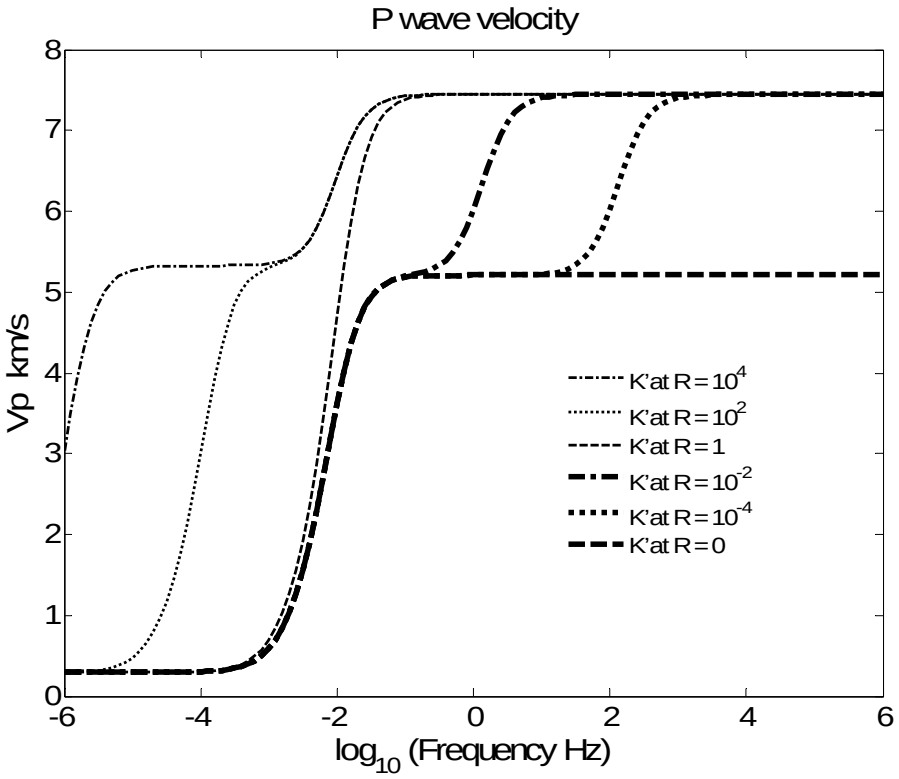

Figure 5.10 Effects of bulk viscosity on the P wave phase velocity. Viscosity ratio R is simulated from 0 to 10^4.

In Figure 5.10, the P wave velocity is calculated for the same ζ / η ratios. Unlike what we saw in V_s in section 5.2, V_p displays a dual relaxation pattern (between three constant V_p values) with exception of the cases when $\zeta = \eta$ and $\zeta = 0$, where, V_p is reduced to one relaxation shape like V_s. It is convenient to discuss V_p behavior if we divide the curve into the lower part and the upper part by the middle constant value of V_p. When $\zeta > \eta$, the upper part remains the same, while the lower part shifts to lower frequency as the viscosity ratio increases. When $\zeta < \eta$, the lower part remains the same, while the upper part

shifts to higher frequency as the viscosity ratio decreases. Both the low and high frequency limits remain at the same value of V_p for all viscosity ratios, with exception of $\zeta = 0$, in which case the high frequency limit remains at the middle constant V_p.

This simulation indicates that the P wave velocity values at a wide frequency range (particularly at high frequency) may have been underestimated due to the ignorance of bulk viscosity. Moreover, a dual-relaxation pattern is expected with bulk viscosity integrated model, which manifests the frequency dependency over a wide band. However, the bulk viscosity-free estimation coincides with bulk viscosity integrated estimation at very low frequencies.

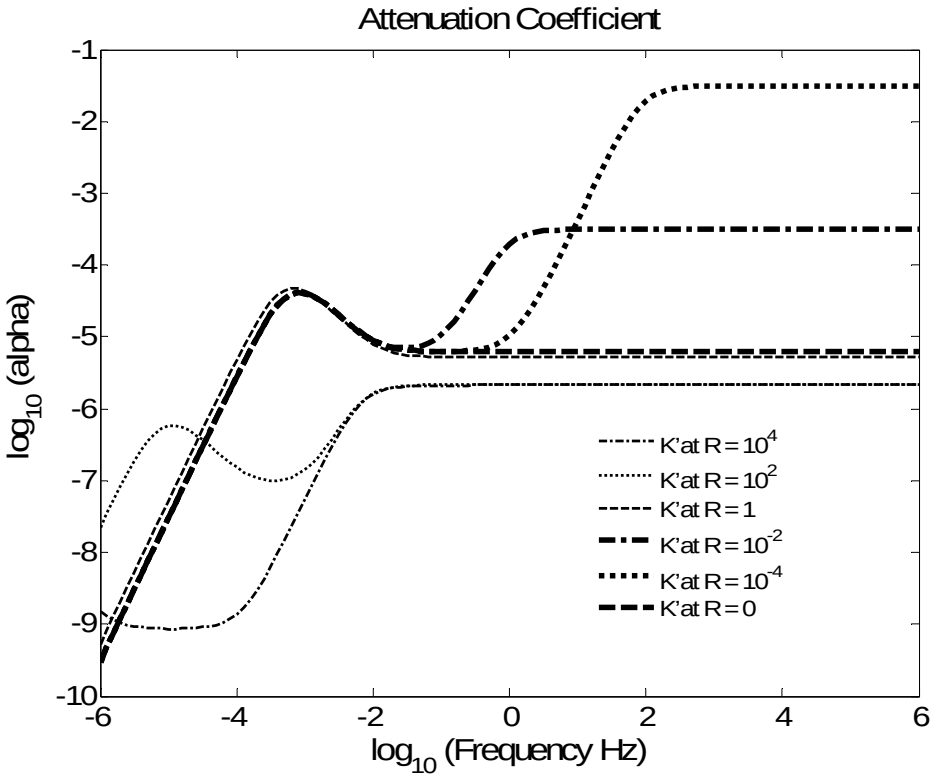

Figure 5.11 Effects of bulk viscosity on the attenuation coefficient. Viscosity ratio R is simulated from 0 to 10^4.

Unlike attenuation for the S wave, the attenuation coefficient of the P wave shows certain peaks at low frequencies (Figure 5.12). When ζ = 0, interesting trend is observed: the attenuation first increases with frequency until a peak value is reached. And then, it drops to a constant value at high frequencies. When the bulk viscosity is introduced, the high frequency plateau is boosted to a higher value, with a relaxing transition stage connecting the peak and the plateau. As bulk viscosity increases, the plateau is lowered, and extends to lower frequencies. When bulk viscosity value reaches that of the shear viscosity, a slightly larger attenuation than bulk viscosity free estimation is observed before reaching the peak, while it drops slightly below the zero bulk viscosity curve at high frequency

plateau. Allowing the bulk viscosity to increase to 10^2 and 10^4 times the shear viscosity, the plateau further drops to a lower value that is unvarying with frequency, while the attenuation peak extends to lower frequency with lower peak values.

Burger's model yields peak-plus-plateau attenuation characteristics, that varies significantly at low frequency, while maintaining a constant value at high frequencies. Up to the viscosity ratio, the attenuation coefficient at seismic band could be increasing ($R = 10^{-4}$) with frequency, or constant ($R > 1$), while in the ultrasonic band, the attenuation coefficient is expected to be a constant for all viscosity ratios.

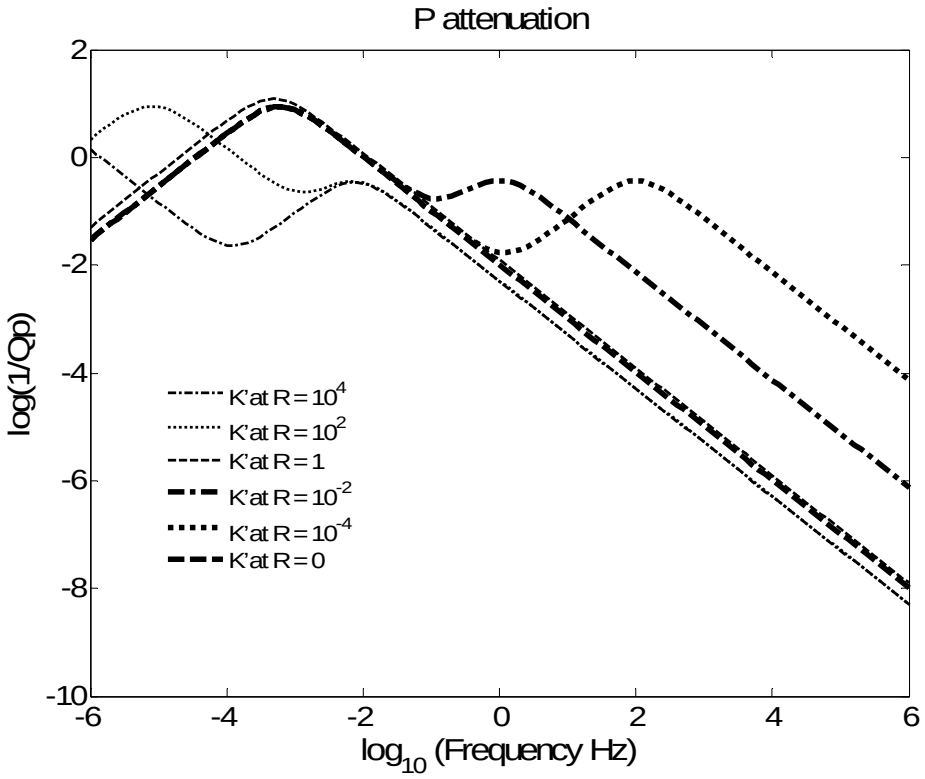

Figure 5.12 Effects of bulk viscosity on 1/Q (attenuation). Viscosity ratio R is simulated from 0 to 10^4.

A dual-peak pattern is observed in the P wave attenuation plot (Figure 5.11), where the attenuation curves can be divided into two peaks (primary peak and secondary peak), with the exception of the cases $\zeta = \eta$ and $\zeta = 0$, where only a single peak is shown. In the same manner that follows the way V_p was discussed, $\zeta = \eta$ is used as a reference. When $\zeta = 0$, 1/Q displays a single peak which is slightly less than the single peak at $\zeta = \eta$, indicating that the bulk viscosity free model underestimates the P wave attenuation. When $\zeta > \eta$, the primary peak of the curve shifts to lower frequency, while the secondary peak remains the same as bulk viscosity increases. When $\zeta < \eta$, the secondary peak

shifts to higher frequency, while the primary peak remains the same. These dual-peak attenuation curves indicate that two attenuation mechanisms dominate the wave behavior. This is reasonable because Burger model itself incorporates two supplementary models (both the Maxwell and the Kelvin-Voigt), each representing a different mechanism. A common feature is that the shear viscosity serves as a critical reference: whether the bulk viscosity is larger or smaller than shear viscosity determines the distribution of attenuation peaks in frequency domain. For the viscosity ratios modeled, the seismic band displays higher attenuation than ultrasonic band.

The following points can be concluded on the effect of including bulk viscosity on the P wave properties:

1. Bulk viscosity has considerable effects on the P wave attenuation and dispersion. The order of magnitude of bulk-shear viscosity ratio defines the attenuation / dispersion relation;
2. Regarding the dispersion and attenuation, the evolution of V_p and $1/ Q_p$ curves can be divided into two parts (corresponding to two relaxation mechanisms) with $\zeta = \eta$ serving as a reference. When bulk viscosity increases from a small non-zero value to η, one of the relaxation curves shifts to low frequency while the other relaxation curve remains; when the bulk viscosity continues to increase beyond η, the formerly constant relaxation curve shifts to even lower frequency, with the former varying relaxation curve remains unvaried.
3. In general, an increasing bulk viscosity shifts the bulk modulus to lower frequency and enhances V_p at high frequency band;
4. V_p and bulk modulus curves merge together at frequency extremes, while for α and $1/Q_p$, only part of the curves merge together at a certain frequency band

and certain viscosity ratios.

5. In case of the commonly ignored bulk viscosity, where $\zeta = 0$, this simulation illustrates that a zero bulk viscosity yields a single relaxation relation, and results in an underestimation of both V_p (thus dispersion) and the bulk modulus. Further, if ζ is assumed to be zero, then the P wave attenuation would be over- or under-estimated over wide frequency bands if $\zeta >> \eta$ or $\zeta << \eta$, respectively.

Chapter 6

Experimental Configuration and Procedure

In recent years, together with the development of unconventional reservoirs, the study of difficult unconventional core samples is highlighted. A particularly interesting material is oil sands, that is, weakly consolidated sands that are saturated with heavy and viscous oil or bitumen. These samples are mainly saturated with heavy oil or bitumen of high viscosity that hinders the flow of hydrocarbon. As drilling and production techniques advance, more and more properties and characteristics are required and this necessitates the laboratory study of wave propagation though such materials.

In this chapter, the details of a new experimental configuration, sample preparation and data acquisition are discussed. First, for two sandstone samples studied, a traditional method is employed. For a heavy oil saturated specific oil sand, a new test protocol that allows for substantial length changes during pressurization is proposed. This is necessary in order to reduce the error of the calculation of the wave speed on such materials.

6.1 Piezoelectric Transducers

Conventional laboratory measurements of P and S wave velocities in rocks make use of piezoelectric transducers. Shown in Figure 6.1 is a photo taken on a variety of P and S wave transducers. These transducers consist of longitudinally (P) and transversely (S) polarized piezoelectric (PZT) crystals, which are capable of converting electrical voltage into compressional and shear motion of mechanical waves (Cady, 1964).

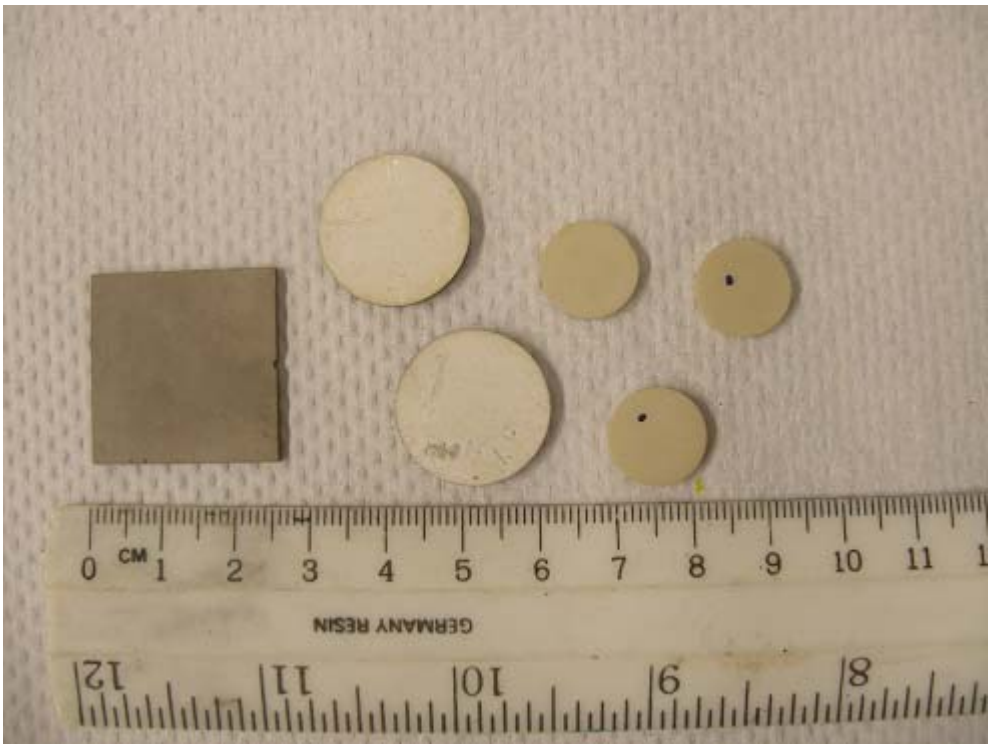

Figure 6.1 Varieties of ceramic piezoelectric transducers (P wave transducers in round shape and S in square)

Piezoelectricity is a phenomenon exhibited by many crystals, natural or man-made. These crystals have no center of symmetry and they take on an electric polarization upon the application of a stress. Conversely, an applied electric field on such materials (along certain axis) is capable of producing a proportional strain. This effect is sometimes referred as *electrostriction*, or simply inverse effect, while the former is called the *piezoelectric* (direct) effect (Cady, 1964). For both effects, the piezoelectric coefficients are the same, and linearity is often preserved. This results in the wide use of piezoelectric transducers in sensing dynamic pressure changes, changes in force and displacement (Burfoot, 1967).

Piezoelectric transducers can be made of natural crystals such as quartz or even from special polymers such as nylon. However, the bulk of the piezoelectric materials used for commercial sensing applications come from synthetic polycrystalline ferroelectric ceramics.

Transducers made from different materials display different frequency response. Commonly used piezoelectric transducers have a center frequency (resonant frequency) ranges from below 1Hz up to several MHz. And the displacement can be as small as μm. (Tressler, et.al., 1998)

Table 6.1 below lists the typical geometry of transducers used in this study:

Table 6.1 Dimensions of different transducers

Transducer type	Type specification	Thickness (mm)	Dimension (mm)
1	P wave 1 MHz	2.05	Φ19.85
2	S wave 1 MHz	1.00	17.07 x 17.07
3	P wave 850 KHz	1.96~1.98	Φ12.67
4	S wave 650 KHz	1.94	12.79 x 12.57

Shown in Figure 6.2 is the initial preparation of P and S transducers. A common practice is to paste (with silver paint) lead sheet at the bottom to ensure contact with sample and copper clip on the top with stress-release design (not shown). Both metals are electronically conductive, thus, they are soldered with wires as electrodes. The preparation of these transducers are crucial because too thick of a paste layer may result in a longer arrival which is hard to estimate; too little paste may result in the stripping of electrodes and failure of the experiment under pressure.

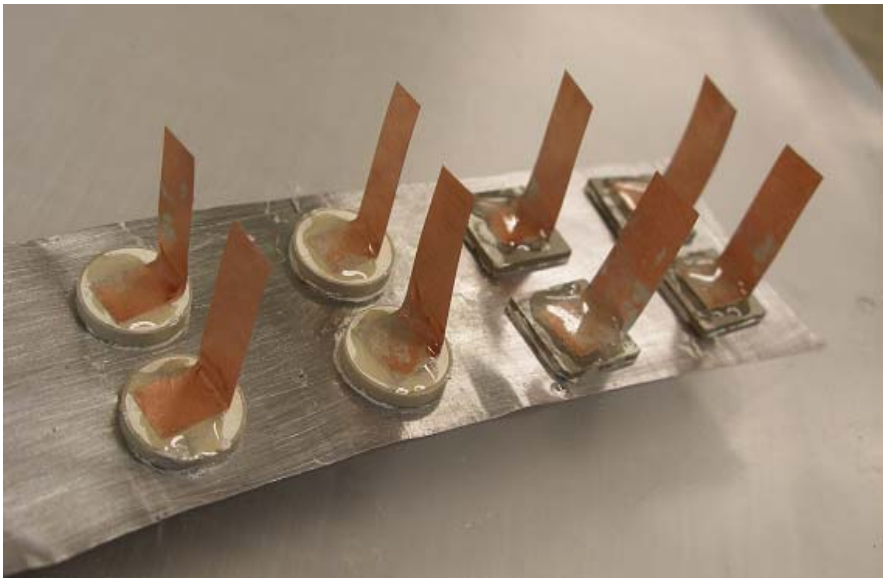

Figure 6.2 Construction of transducers (P wave transducers in round shape and S in square)

6.2 Pressurization System

A pressure vessel is used in the lab to perform experiments regarding confining pressure and/or pore pressure variation. The real pressure vessel (as well as pulser and oscilloscope) used in the lab is shown in Figure 6.3, while a schematic plot showing the entire system is presented in Figure 6.4.

Figure 6.3 Pressure vessel, pulser and oscilloscope

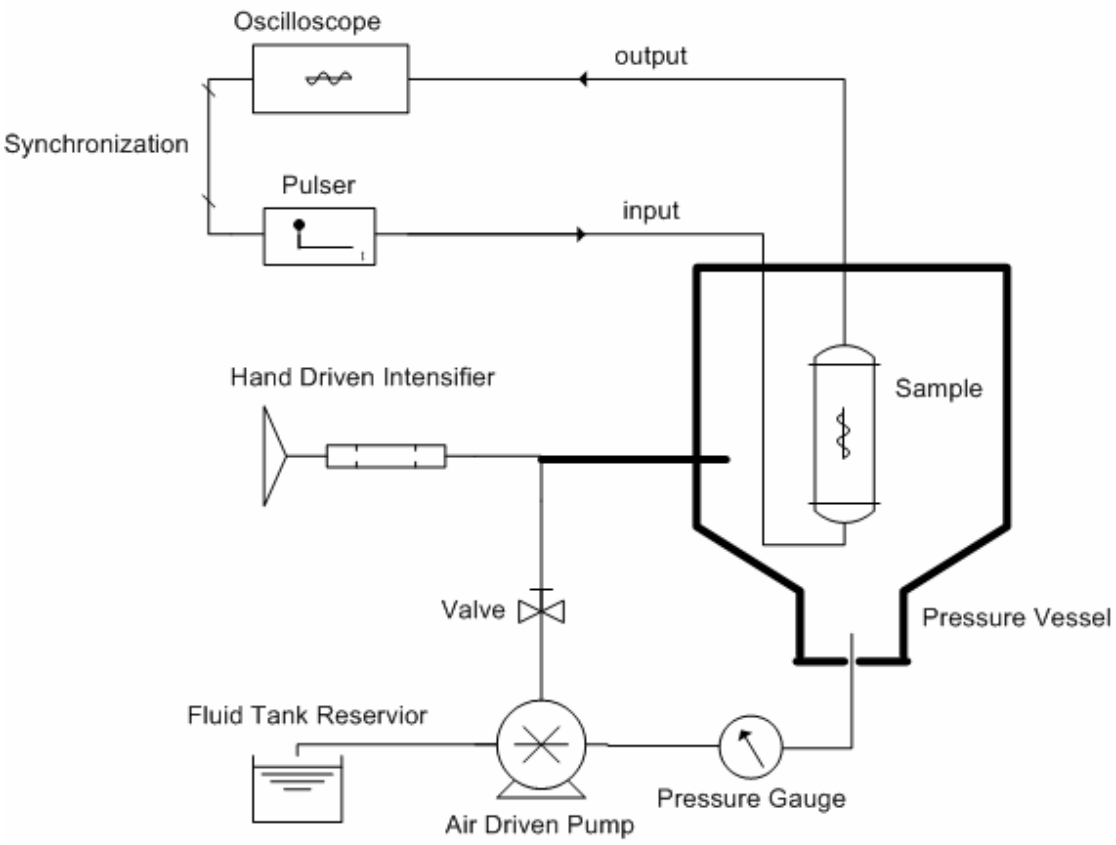

Figure 6.4 Pressure system scheme

This cylindrical pressure vessel is able to apply confining pressure up to 200 MPa. It is achieved by an air-driven hydraulic pump by forcing oil (76 lubricants®) from fluid tank reservoir into the pressure vessel, thus pressure is increased, with value displaying on pressure gauge. The specifically required pressure can then be finely adjusted with a hand driven intensifier to a precision of 0.25 MPa. There is an opening on the top of the vessel through which sample is put into the pressure vessel. The lid to this opening hosts 9 electronically conductive but isolated feed throughs, with one electrode connected to the pulser as input and another connected to the digital oscilloscope (Gagescope Model 400-586-203) to show and record the output signal. Inside the vessel, these two electrodes (connected to pulser and oscilloscope outside the vessel) are soldered to each end of the

sample's electrodes, thus the signal generated in the pulser can travel into the vessel, converted to mechanical oscillation by transmitters, mechanical waves through the sample, converted back to electric voltage by receivers, out of vessel and to finally be recorded on the oscilloscope. Two pairs of electrodes are required for either the P or the S wave, with one pair for input and another for output. Hence, if both waves are to be measured, a total of 8 wires are needed. The later optimized setup with stacked P and S transducers can save two wires (due to some shared electrodes), making a total of 6 feed-throughs required.

6.3 Ultrasonic Techniques and Conventional Velocity Determination

Conventional laboratory measurements of P and S wave velocities of rocks can be sorted into two categories: pulse echo and pulse through-going.

The pulse echo technique requires only one P or/and S wave transducers, as both transmitter(s) and receiver(s), while the pulse through-going requires a pair of each (Figure 6.5). With pulse echo, signal goes into the sample and reflects back at the 'open' interface between sample and air (or another suitable backing material) before it is received on the same transducer. A reflection is also produced at the sample-buffer interface with similar geometry. Then two waveforms and travel times are obtained for the velocity and attenuation calculation (Peselnick and Zietz, 1959).

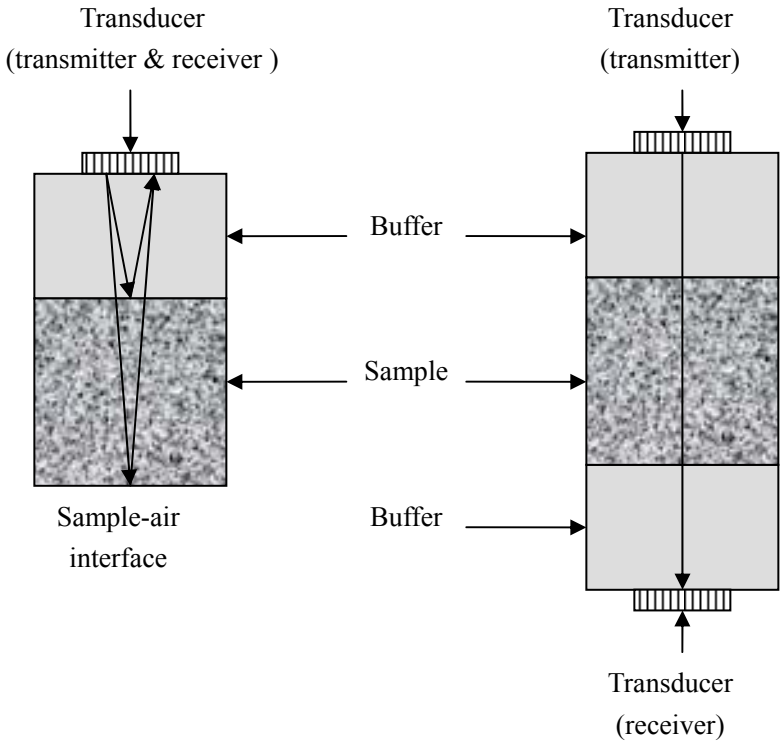

Figure 6.5 Pulse echo and pulse through-going techniques

The downside of pulse echo is that the minimum travel path is twice the sample length; if a long sample is tested, the signal quality is lower than the through-going. And another issue that undermines the pulse echo method is that the reflection coefficient is usually unknown; therefore, the energy loss due to refraction on the interfaces could make considerable difference. In order to serve the purpose of this study (attenuation in highly attenuating materials), the through-going technique was utilized to ensure best signal quality and reduce possible extrinsic attenuation.

Both techniques utilize certain length of buffer(s) in order that the arrival is distinguishable from the RF electromagnetic noise at early time due to the pulser. Another reason of using the buffer (usually in pulse-echo technique) is to get a

reference waveform in order that attenuation can be calculated (Figure 6.5 left). No matter how it is used, the buffers should be of very low attenuation; usually, buffers are made of metal such as aluminum, so that the original waveform is maintained as much as possible through the buffer. In pressurization tests, the buffers further sustain a planar surface between the specimen and transducers. This would prevent localized stress on transducers due to non-planar shape or deformation of the specimen as the confining pressure changes. This is crucial in the current study as the material itself will be highly compressible.

Common practice in the lab makes use of ultrasonic frequency transducers with center frequency at 1 MHz. A standard through-going test method is documented into an ASTM standard (ASTM D2845), and the setup of this work follows this procedure with adaptation made according to Molyneux and Schmitt (1999) and He and Schmitt (2006).

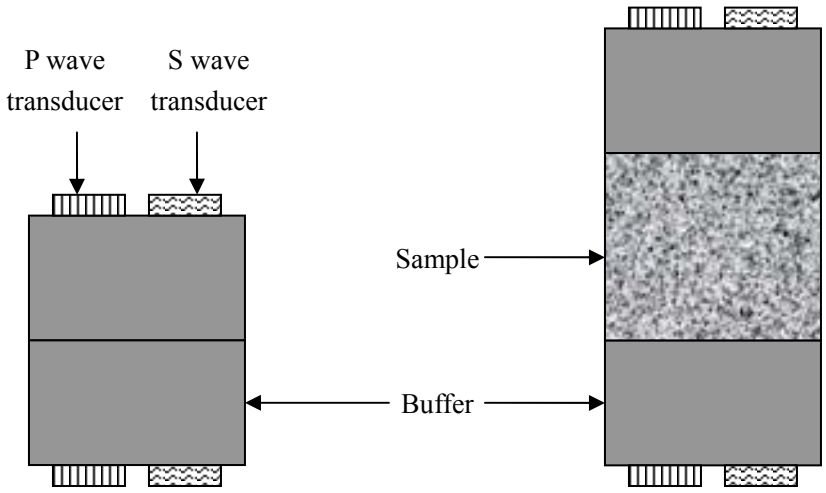

Figure 6.6 Scheme of calibration and measurement setup (separate P and S transducers)

The setup of the transducer-buffer-sample alignment is shown in Figure 6.6 (right hand side), P and S transducers are installed in separate locations. If the same wave path (usually the center of sample) is crucial, they can be installed in a stack (Figure 6.7, right hand side). The latter setup saves a few couple of feed throughs, but the problem of stacking is the introduction of more interfaces and therefore, more reflection within the transducer. Consequently, the received energy is expected to be lower for the stacked transducers. Stacking does not change the travel time significantly and in any event this is accounted for by calibrating the sensors (Figure 6.6, 6.7 left hand side). For attenuation, it is recommended to calculate parameters using a spectral decomposition method in which two waveforms obtained at different sample lengths or with one through a low attenuation material being a reference. This method will eliminate most problems introduced by stacking.

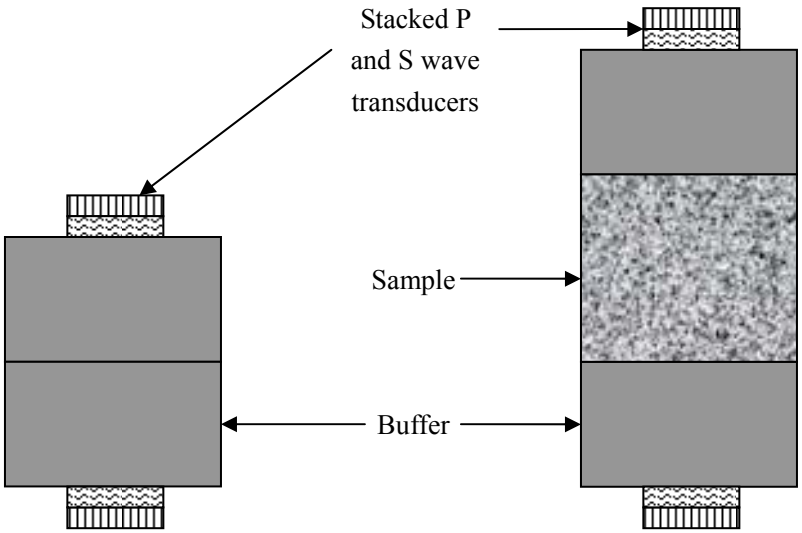

Figure 6.7 Scheme of calibration and measurement setup (stacked P and S transducers)

Figure 6.8 Conventional preparation of test samples (with P and S wave transducers stacked)

In order to calculate P and S wave velocities, the travel time of the generated pulse traveling through the buffer(s) must be accounted for. Assuming two end buffers (caps) are used (pulse through-going techniques), the buffer travel time t_1 is measured by placing buffers face to face (Figure 6.6, 6.7 left hand side), sending pulse through and picking the first extreme of the amplitude. Then, the sample is placed in between and the longer travel time t_2 through both of the buffers and the sample is measured in the same way. The travel time through the rock sample (Δt) is simply the difference $t_2 - t_1$. The velocity determined this way is the quotient of the sample length and the travel time:

$$V = L / \Delta t \tag{6.1}$$

where L is the length of the sample and sample travel time $\Delta t = t_2 - t_1$.

However, due to the potential of velocity dispersion, the components of the signal in different frequencies do not arrive at the same time, therefore velocities calculated this way are generally assumed to yield the speed of the predominant

frequency of the signal. Therefore, this undermines the accuracy of picking up the first extreme (either peak or trough) to determine the velocity. Instead, a more robust calculation called spectral decomposition is employed. Details of this method are discussed in the section 6.6.

The pulse through-going technique also has numerous potential concerns, such as alignment of transducers and the coupling between the buffer and the sample. These issues require some care in sample preparation.

One such factor that is often ignored is changes in the length of a sample during pressurization. Usually, ignoring this length change is not a problem as a 'typical' rock will shorten by less than 1% to the pressures measured and this error becomes part of the uncertainty of the measurement. However, in the current measurements on compressible sands, the length change can be significant. Therefore, in order to get an accurate reading of sample length, a new lab design is described in the next section.

6.4 New Velocity and Attenuation Measurements Equipments

The P wave velocity and attenuation were measured on highly attenuating glass bead samples by Molyneux and Schmitt (1999). They found that the standard technique to determine the wave arrival time by 'picking' the first break of the arriving wave is questionable, because the first arrival or peak may have potential dispersive delay. For viscoelastic (highly attenuating and dispersive) materials, picking up the first amplitude extremum results in an under-estimated velocity. More than that, velocities in viscoelastic materials are usually frequency-dependent, thus the velocity determined in a traditional way is limited to a narrow frequency band.

Moreover, the length of the sample will change as pressure varies. The traditional test protocol does not take this into account, which would result in over-estimated velocities.

With these problems in mind, a more robust algorithm is proposed to compute velocities as a function of frequency and a new apparatus is made to measure the length change of the sample during pressurization. Modifications of test techniques are also made to ensure good signal quality.

In this study, modification was made bearing the viscoelastic nature of the test materials in mind:

1. Lower resonant frequency transducers were used because of the attenuation at high frequency that results in a low signal to noise ratio, particularly for the S wave;
2. Acrylic (PMMA) is used as end caps (buffer) instead of aluminum in order to reduce the impedance jump at the buffer-sample interface and to further maximize the energy through the sample;
3. An aluminum frame with variable resistors is designed to measure the length change and at the same time to ensure alignment of the buffers as the sample is compressed.

Figure 6.9 shows the comparison of the waveforms produced by 1MHz P and S ceramic transducers with those produced by lower frequency transducers. The P wave is reduced to 850kHz and S wave is reduced to 650kHz. Both waves propagated through a 28.75 mm typhon plastic sample. All experimental configurations were otherwise kept the same. As one can see, the lower frequency transducers yield larger amplitudes than standard 1MHz transducers, which is better for further calculation. Since even lower center frequency transducers were

not available, this pair of transducers were used in the later experiment.

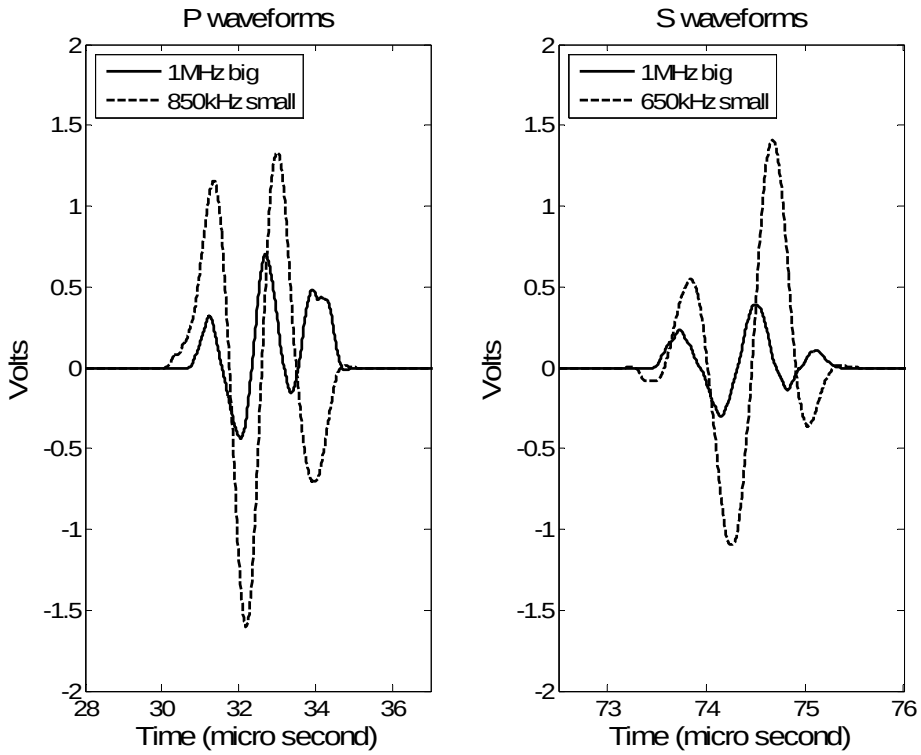

Figure 6.9 Comparison of signal quality from different transducers (the 1MHz and 850kHz P waves on the left panel and the 1MHz and 650kHz S waves on the right panel were propagated through a 28.75 mm typhon plastic sample)

The buffers were also changed in order to ensure a better impedance[3] match between the sample and buffers. Several commonly used plastics and metals in the lab were tested, and acrylic is finally chosen to perform later tasks. The density, velocities and impedances of these materials are listed in Table 6.2 below:

[3] Acoustic impedance is a material property defined by the product of compressional wave velocity and the material's density, with unit $N \cdot s/m^3$ or $Pa \cdot s/m$. It is important in the determination of acoustic transmission and reflection at different materials' boundary; the design of ultrasonic transducers; and assessing absorption of sound in a medium.

Table 6.2 Measured Impedance of Sample and Buffer Materials

	Density (g/cm^3)	Vp (km/s)	Vs (km/s)	Zp ($kg/m^2s \times 10^6$)
Sample	2.00	2.40	1.67	3.40
Acrylic	1.18	2.80	1.42	3.29
Grey Plastic	1.22	2.31	\	2.82
Delrin	1.35	2.35	\	3.17
Taphon	2.16	1.25	0.51	2.70
Aluminum	2.70	6.32	3.13	17.06
Brass	8.42	4.43	2.12	37.30

The acrylic used as buffer in later sections, has a density of 1.18 g/cm^3, which falls within the value of 1.17~1.20 g/cm^3 in literature (Rosato and DiMattia, 1991). The bulk and shear moduli calculated from velocities are 2.38 and 6.08 GPa for shear and bulk respectively and they comply with the wide range of data provided in the same source.

In order to move the buffer together with the sample due to sample length change under pressure, the buffer shape is also modified. Figure 6.10 shows the schematic acrylic buffer in the new design. Conventional aluminum buffer requires a groove to house O-ring in the purpose of sealing the sample. In these length changing measurements, an additional lip bump is designed to transmit the pressure from the apparatus (will be discussed) to the sample. Figure 6.11 shows the materialized buffer pair.

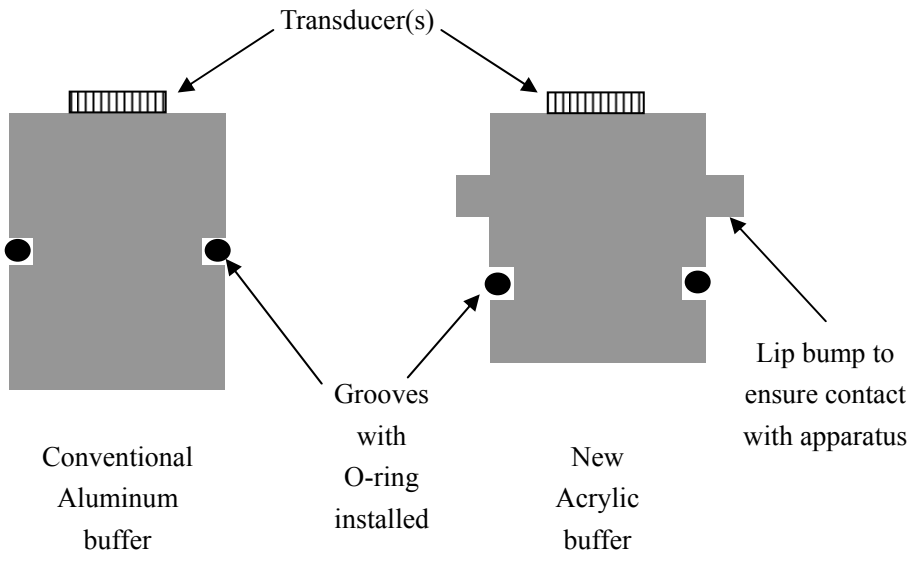

Figure 6.10 Comparison of conventional and new buffer caps

Figure 6.11 New buffer caps – acrylic with additional lip bump design

A new apparatus is also designed to measure the length change as the confining pressure varies. As shown in Figure 6.12, 3 plates form the body of this apparatus, with three rods rigidly fixing the top and bottom plates in such a way that only the middle plate is allowed to slide along the rods. Installed also are three variable resistors (position sensors) between the moving and the bottom plates. The moving plate will slide according to the change in the length of the sample. Hence these variable resistors display this length change in the form of varying resistance. After collecting the data, the varying resistance is converted back to the length change provided an appropriate calibration relation is known.

During the preparation process, the weakly consolidated sample is put in a plastic pipe to further ensure the moving path of the buffer is well aligned when pressure changes, and then the sample together with the plastic pipe is wrapped in a flexible hose (Tygon®) to prevent leakage of the confining fluid into the sample. Lastly, the whole pack is installed between the top and moving plates, and the system is ready to put into pressure vessel to take measurements. A actual picture showing this setup is in Figure 6.13.

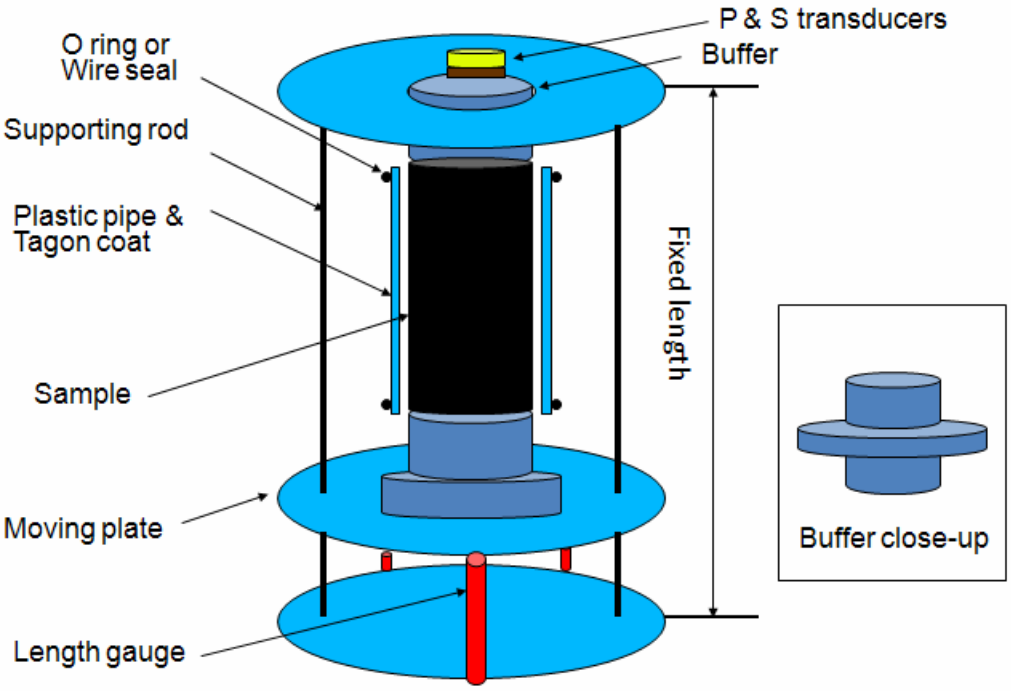

Figure 6.12 New apparatus design scheme

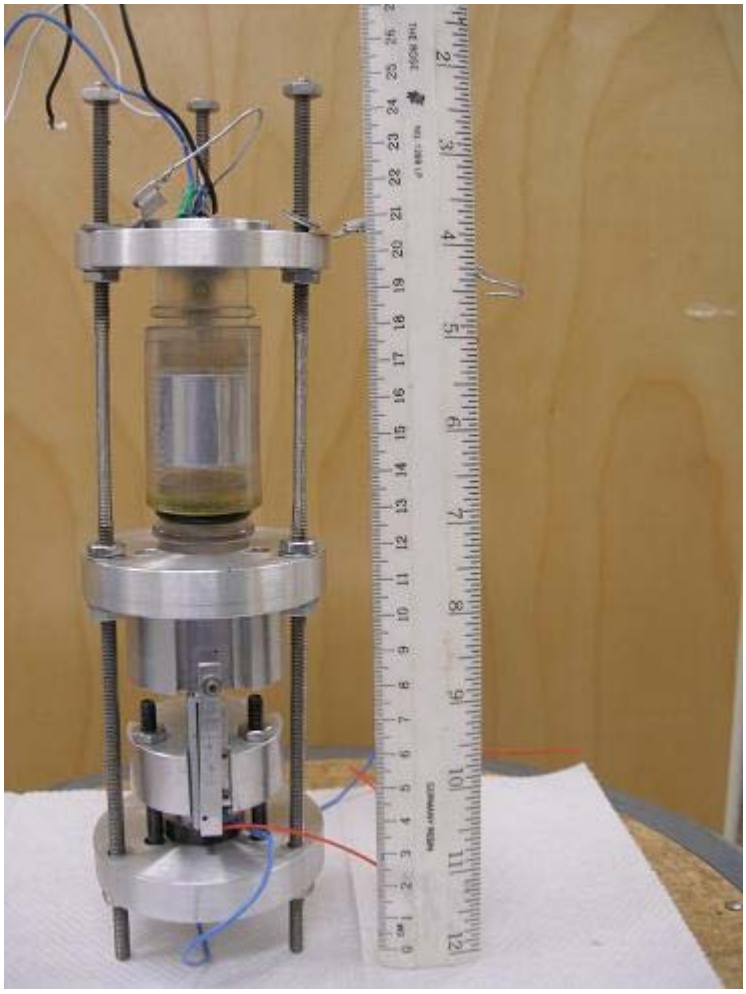

Figure 6.13 Photograph of the apparatus (an aluminum sample is used for photo taking purpose)

6.5 Calibration

The experiment equipments include a high voltage pulse generator (Model 3) and a digitizing oscilloscope (Gagescope Model 400-586-203). The pulse generator produces a fast-rising (25ns), 200 V square wave that is used to activate the transmitter. Activated by this pulse, the transmitter generates compressional or shear mechanical waves (vibrations) centered at the resonant frequency of the ceramic. This signal propagates through the sample and is received at the other end. The waveform displayed on the screen is sampled at an interval of 8 nanoseconds. The "average" channel shows the final average waveform of 256 progressively stacked records to reduce random noise. Data is then recorded digitally by the oscilloscope.

Below, the calibration of newly designed system is divided into two parts:

1. Calibration of the transducer-buffer pairs, and
2. Calibration of the position sensors

6.5.1 Calibration of Transducer-Buffer Pairs

Before measuring real samples, one always needs to calibrate the buffer caps to understand how they will behave during the experiment. But for oil sands, the impedance between sample and an aluminum buffer is too large that a significant fraction of the energy is reflected. Therefore, acrylic was employed to ensure a better match.

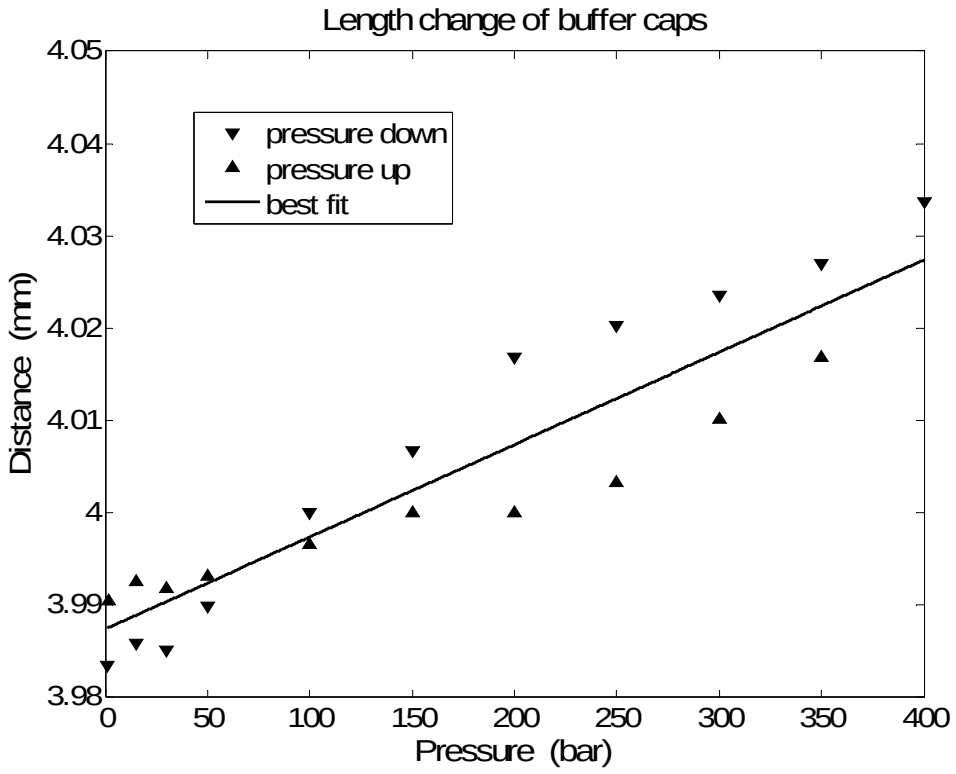

Figure 6.14 Calibration of end cap length change as a function of pressure (The up-pointing triangles represent pressure increasing while the down-pointing triangles stand for pressure decreasing. This symbol definition is assumed in later text without restatement)

Unlike the stiffer aluminum buffer caps, acrylic has low elastic moduli and therefore the change in its length under pressure may have influence on calculation. Figure 6.14 shows the calibration of this change. The triangles that point up represent the pressure increasing portion of the cycle while the down-pointing triangles stand for pressure decreasing (This symbol definition will be assumed in later text without restatement). The total length change adds up to only 0.1% of the original buffer length of 30.00 mm (up to 400 bars of hydrostatic confining pressure). Since such a small deviation does not affect the result much, this change in buffer length is instead considered as part of the overall change in

the transit times.

The travel time in acrylic buffers also varies as pressure changes in part due to the change in length but more principally due to the increased modulus of the acrylic with pressure. In Figure 6.15, a linear relation is found between P wave travel time and pressure (length of buffer is assumed to be constant):

$$t_p = 23.5090 - 0.0022\ p \qquad 6.2$$

where p is pressure in bars and t_p is the P wave travel time in micro seconds.

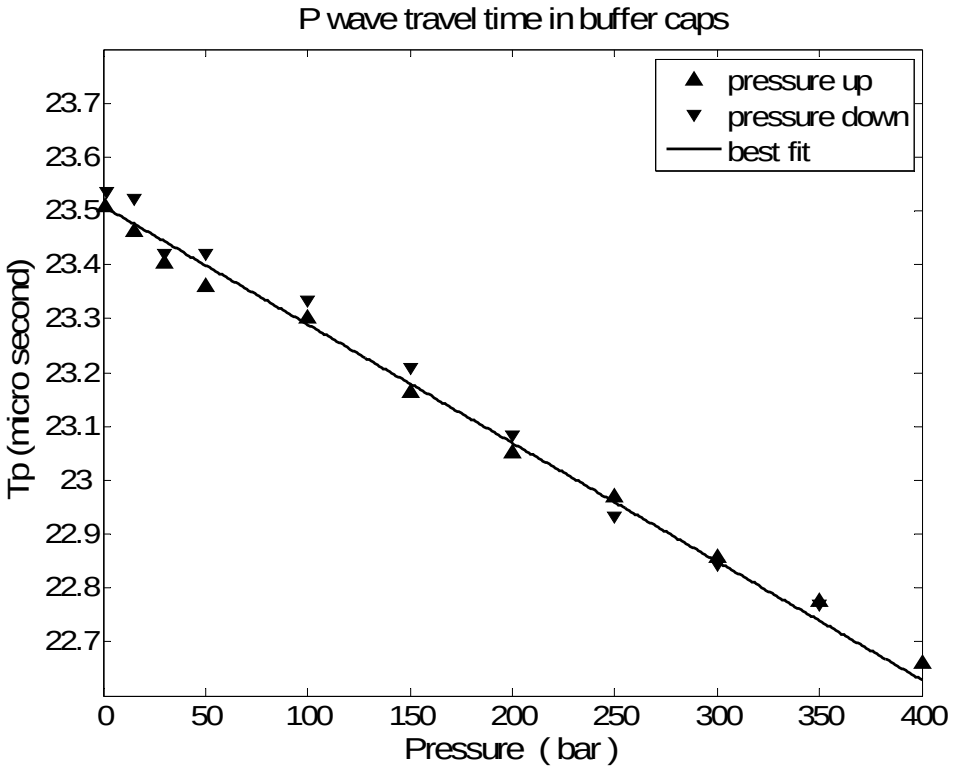

Figure 6.15 Calibration of end cap travel time as a function of pressure (P wave)

The same calibration is also carried out for the S wave, shown in Figure 6.16. The relation is formulated as:

$$t_s = 44.9960 - 0.0027\ p \qquad 6.3$$

where ts is the S wave travel time in micro second and p is pressure in bars.

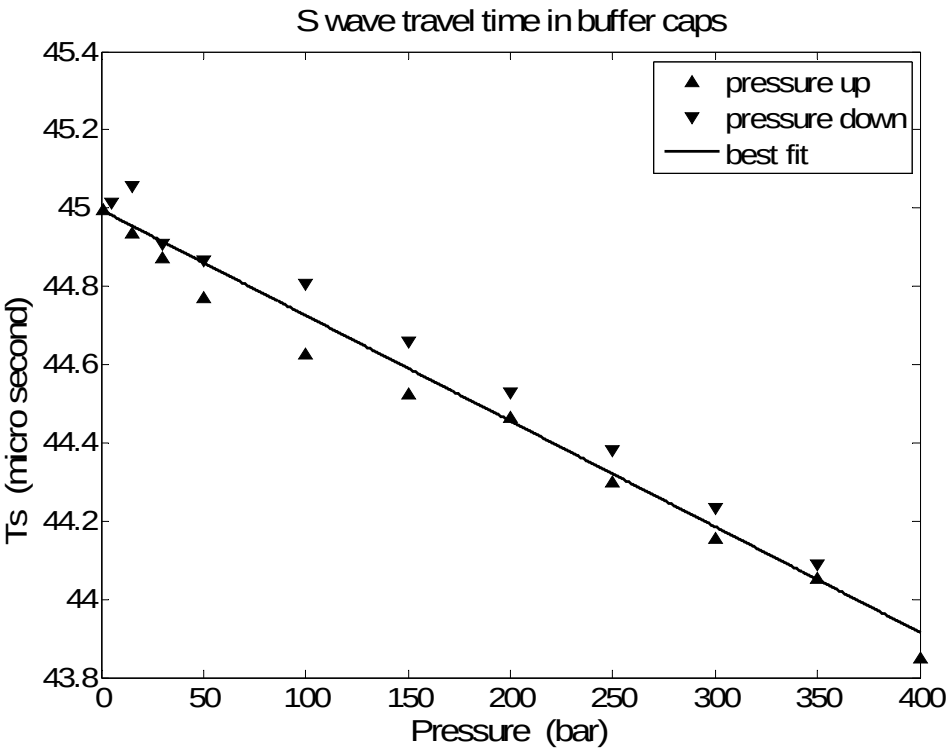

Figure 6.16 Calibration of end cap travel time as a function of pressure (S wave)

A maximum of 3.8% change in the P wave travel time is observed while the S wave gives a 2.5% maximum as pressure ranges from 0 to 400 bars. This change is also small but not insignificant. However, in order to ensure an accurate calculation, this travel time change in buffers must be compensated in later calculation.

6.5.2 Calibration of Position Sensors

Position sensors are often in nature variable resistors. The sensors used here are usually used in digital cameras to measure the movement of lenses and these are easily available and surprisingly inexpensive. The model used here is Panasonic EVAJG with a maximum resistance of 10 kOhm (shown in Figure 6.17).

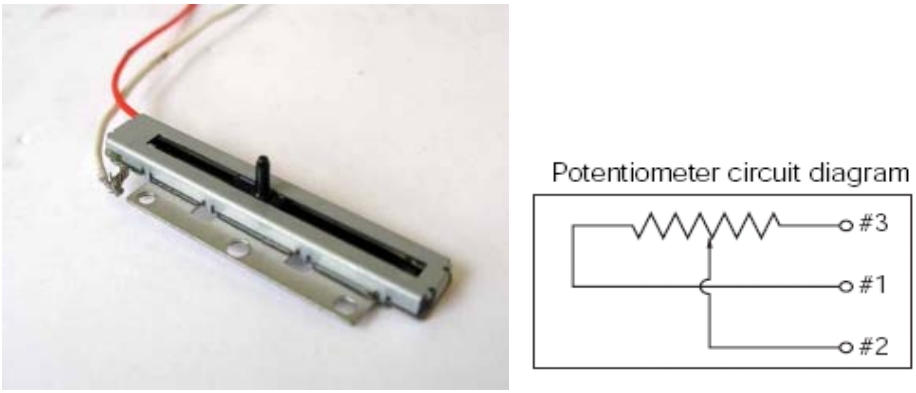

Figure 6.17 Position sensors (left panel: real picture, right panel: scheme of circuit, showing the floating foot as #2)

With the floating foot (or hold) #2 hooked to the moving plate of the apparatus and the body of the sensor installed on the fixed plate, the travel distance between two plates can be measured by simply reading the resistance between feet #2 - #3 or #2 - #1 (measured by a HP multimeter). As the floating hold moves, however, the resistance changes not only with travel distance but also pressure due to deformation of resisting material. Therefore, the parameters from the manufacturer (provided only as function of distance at atmospheric pressure) must be revised to serve the purpose of this study. In a word, the calibration carried out here tests the relation between resistance, position and pressure using

an empirical formula:

$$R = C_0 + C_1 pd + C_2 p + C_3 d \tag{6.4}$$

where R is resistance in kOhm, p is pressure in bars and d is the position in millimeters. Any higher second order terms are assumed to be zero, with cross term reserved as a test.

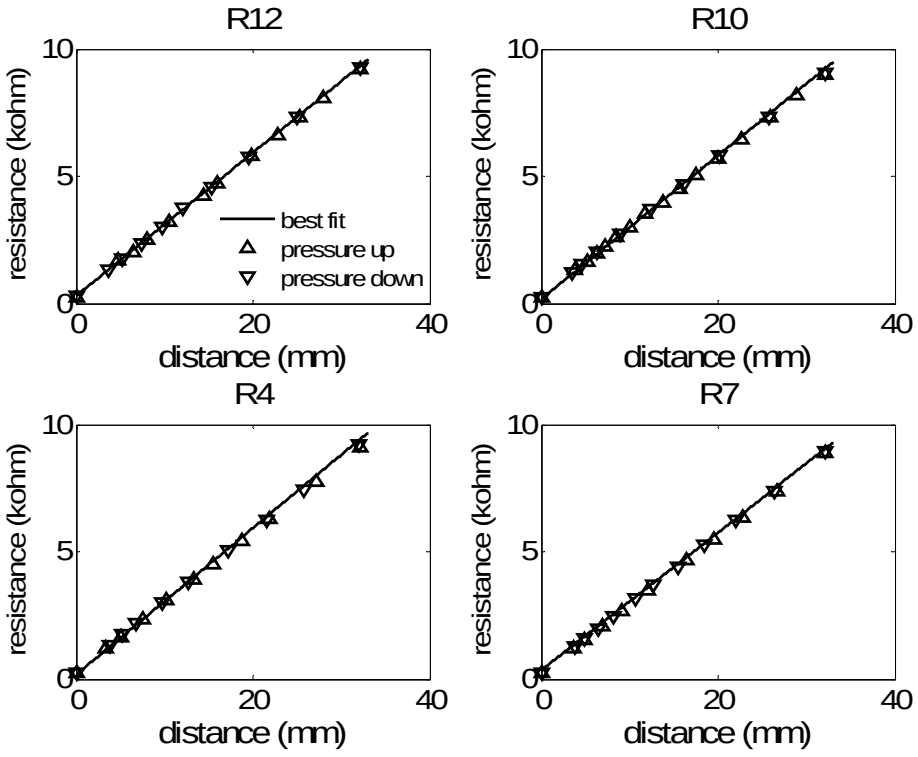

Figure 6.18 Resistance of R4, R7, R10, R12 before and after pressurization as a function of travel distance

Shown in Figure 6.18 and 6.19 are the calibration tests for resistors R4, R7, R10, R12. To find out full parameter profiles (C_0, C_1, C_2, C_3), the calibration is first carried out by measuring resistance as a function of the travel distance (measured by an electronic digital caliper as accurate as 0.01 mm at 1 atm). The

results are shown in Figure 6.18. Little deviation from linearity is observed, which means resistance maintains a good linearity with travel distance as provided by the manufacturer.

After this, the position sensors are put into the pressure vessel to test its response as pressure increases from 0 bar to 200 bars and back to 0 bar (pressure measured by gauge with collaboration with hand driven intensifier). This process was repeated at 3 different travel distances (during each process, travel distance is fixed by placing two rigid bars that constrains the floating foot of the resistor from moving). The results are shown in Figure 6.19, each line represents the best fit of measurements at a given travel distance.

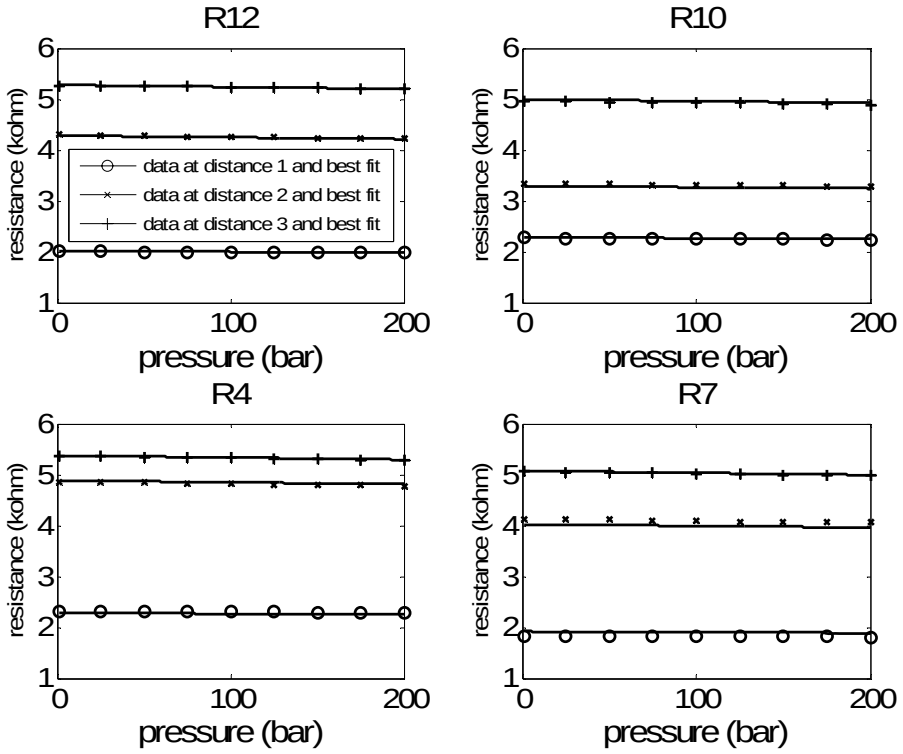

Figure 6.19 Resistance of R4, R7, R10, R12 at different travel distances as a function of pressure. Each line represents the best fit of measurements at a given travel distance.

Then, the final step is to repeat step one of testing the resistance as a function of travel distance, but after pressurization. This is to confirm that no damage was made during pressurization. Since little deviation from linearity is observed, the resistors are believed undamaged after pressurization (Shown in Figure 6.18 by down-pointing triangles).

To sum up the results in the calibration of the position sensors, linearity in response is observed in both the pressurization and the travel distance tests. No measurable hysterisis was found. The deviation from linearity (best fit linear line) is well within 5%, which fits quite well with the manufacturer's parameters.

According to the results from the lab and the manufacturer, linearity holds over a wide range. Consequently, C_1 is zero. C_0, C_3 can be calculated in steps 1 and 3 of the test mentioned above. C_2 can also be found in step 2. The different position sensors tested here have very close values for C_1, C_2 and C_3, while C_0 varies. This indicates that the quality of these position sensors is good and that they would behave consistently during the experiment.

The full expressions of resistance as a function of both pressure and travel distance are shown as below:

$$R_{12} = 0.2901 - 0.0001\,p + 0.2814\,d \qquad 6.5$$

$$R_{10} = 0.1655 - 0.0000\,p + 0.2822\,d \qquad 6.6$$

$$R_{4} = 0.1694 - 0.0001\,p + 0.2881\,d \qquad 6.7$$

$$R_{7} = 0.3243 - 0.0000\,p + 0.2713\,d \qquad 6.8$$

where d is in millimeters, p in bars, and resistance in kOhm. Since the uncertainty of pressure is 5 bars, and that of resistance is less than 5%, the total uncertainty in measuring length with these sensors is estimated to be less than 0.5 mm.

6.6 Analysis Methodology

To calculate P and S velocities as a function of frequency, a technique called *spectral decomposition* is employed. Two recorded waveforms produced by transmission through different lengths of samples were windowed and filtered. Then waveforms were taken FFT (Fast Fourier Transform), and phase velocities were determined by calculating the phase difference $\Delta\phi$ from the unwrapped phase spectra (Figure 6.20b):

$$\Delta\phi(\omega) = \phi_2(\omega) - \phi_1(\omega) \tag{6.9}$$

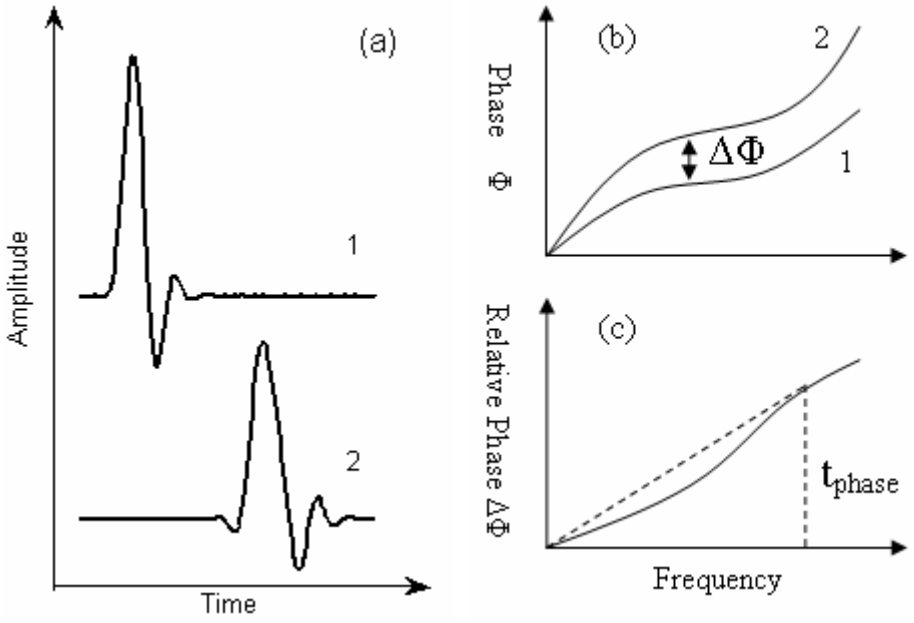

Figure 6.20 Illustration of the calculation of phase velocity

Such a relative measurement eliminates measurement of the initial phase of the source. The phase lag time between observations is,

$$\Delta t_{phase}(\omega) = \Delta\phi(\omega)/\omega \tag{6.10}$$

with the phase velocity equal to (Winkler and Plona, 1982):

$$V_{phase}(\omega) = (x_2 - x_1)/\Delta t_{phase}(\omega) \tag{6.11}$$

Attenuation coefficients are found by taking the spectral ratio of two Fourier transformed amplitude spectra. If we denote a Fourier transformed amplitude spectrum (after Yin, 1993):

$$A(\omega, x_i) = S(\omega)D(\omega)\exp\left[-\alpha(\omega)x_i\right](1-R^2) \tag{6.12}$$

where $S(\omega)$ is the amplitude spectrum of the outgoing pulse produced by the transmitter, $D(\omega)$ is the amplitude response spectrum of the receiver, $\alpha(\omega)$ is the frequency dependent attenuation coefficient of the sample to be determined, and x_i is the distance from source. In this case, it is the sample length and *R* is the reflection coefficient at the buffer-sample interface.

By taking the spectral ratio on two amplitude spectra obtained from two samples of different lengths, the attenuation coefficient can be calculated:

$$\alpha(\omega) = -\ln\frac{A(\omega, x_2)}{A(\omega, x_1)} \Big/ (x_2 - x_1) \tag{6.13}$$

Finally, quality factor Q can be calculated from phase velocity and attenuation coefficient (Equation 2.4).

In a real case, simply calculating α from two waveforms does not constrain the error. Therefore, a series of samples of different length are tested, and α is

found by fitting a straight line through data points that are calculated by each pair of the waveforms.

If one rewrite Equation 6.13 into :

$$Y = -ln\left[\frac{A(\omega, x_2)}{A(\omega, x_1)}\right] = \alpha(\omega) \bullet (x_2 - x_1) \qquad 6.14$$

Obviously, α can be determined by the slope of a natural log Vs $\Delta x = x_2 - x_1$.

Theoretically speaking, this methodology can be applied to any frequency. However, only a limited frequency band around the resonant frequencies carry most of the energy, and thus the information. Therefore, this spectral ratio method is applied only to a specific frequency band (0.6~1.4 MHz in this study) which covers the primary peaks in both P and S wave spectra.

Shown below is an illustrative study of the attenuation coefficient of acrylic. The reason of testing the methodology on acrylic is that they have very close impedance with oil sands. One would expect a realistic case (oil sands, for instance) to display a much lower modulus and more scattering due to the presence of different phases (air, oil and sand). This test is done via a traditional setup (1MHz transducers with aluminum buffer but with no length detecting apparatus).

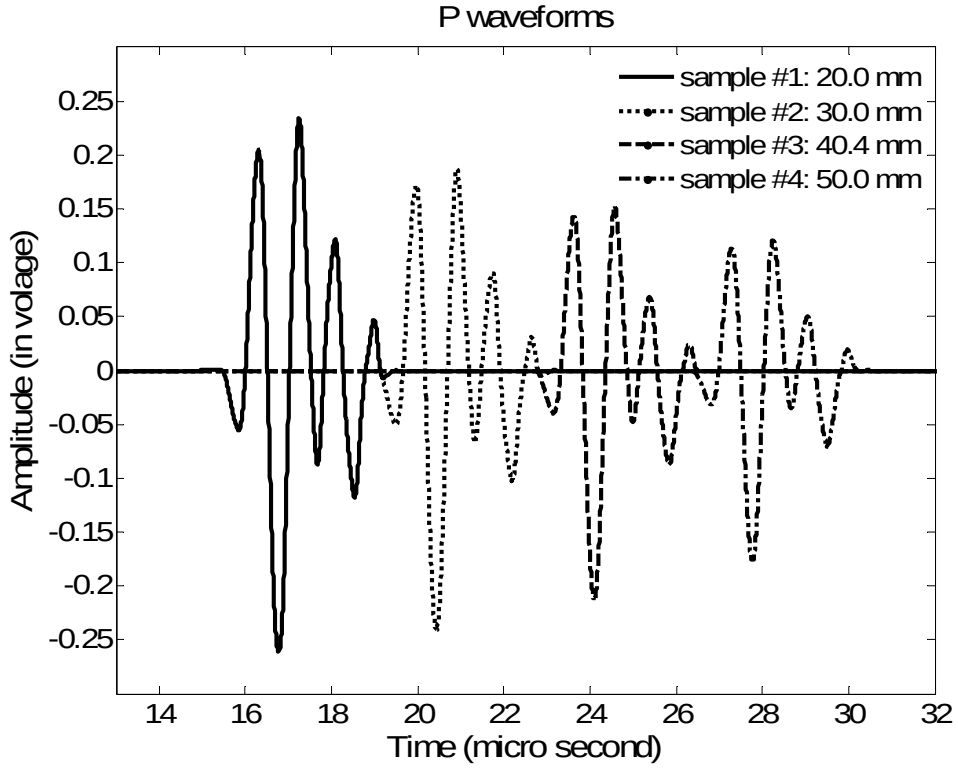

Figure 6.21 P waveforms through acrylic samples of different increasing lengths

In Figure 6.21, a series of P waveforms were obtained through four acrylic samples with lengths of 20.0 mm, 30.0 mm, 40.4 mm and 50.0 mm. As clearly shown, the waveform character is consistently maintained, but with a decay in amplitude (phase shift is not as obvious as S wave in Figure 6.25) as the sample length increases. The corresponding amplitude spectra of these waveforms are shown in Figure 6.22. A consistent decrease in amplitude is observed as expected. However, the peak of spectra is centered at 1.095 MHz (average of the four peaks), which is slightly different from the nominal piezoelectric ceramic resonant frequency. This is likely arises from the fact that the transducer resonant frequency results from both the buffer, the ceramic, and the damping material combination. During the construction of these transducers, silver paint, epoxy glue and backing materials are cemented to the transducer, which may alter the

resonant frequency. Therefore, in calibration, one can see a shift from the nominal center frequency of 1MHz with the new center considered as the characteristic frequency of the entire system, including transducer and all that is attached to it. The α calculation is based on the amplitude at this new characteristic frequency.

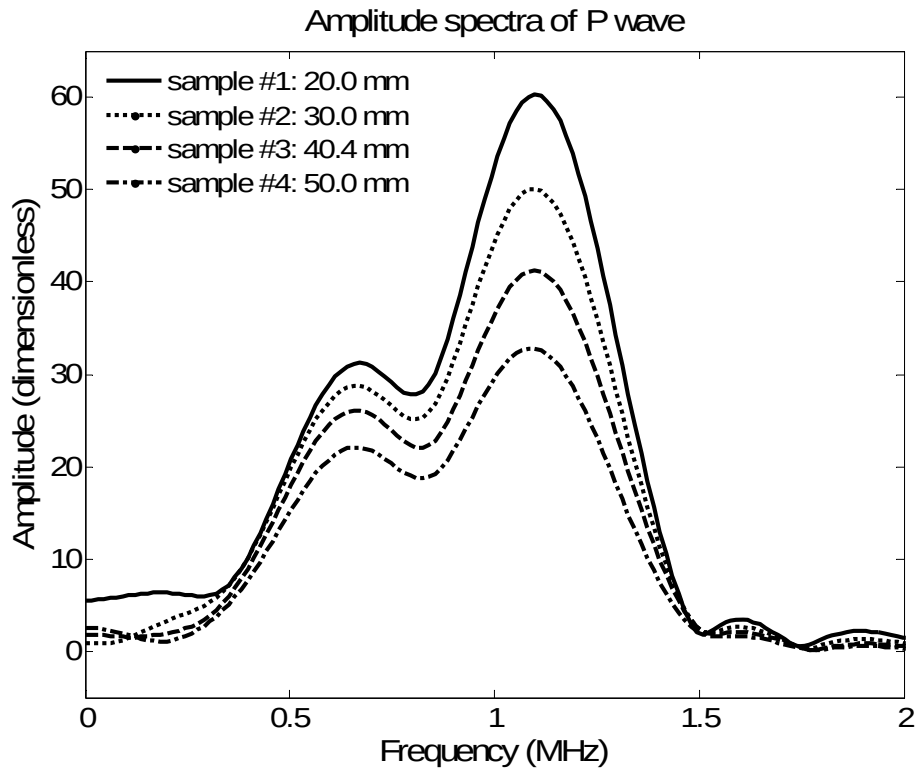

Figure 6.22 Amplitude spectra of P waveforms (primary peak is considered at 1.095 MHz for all four curves)

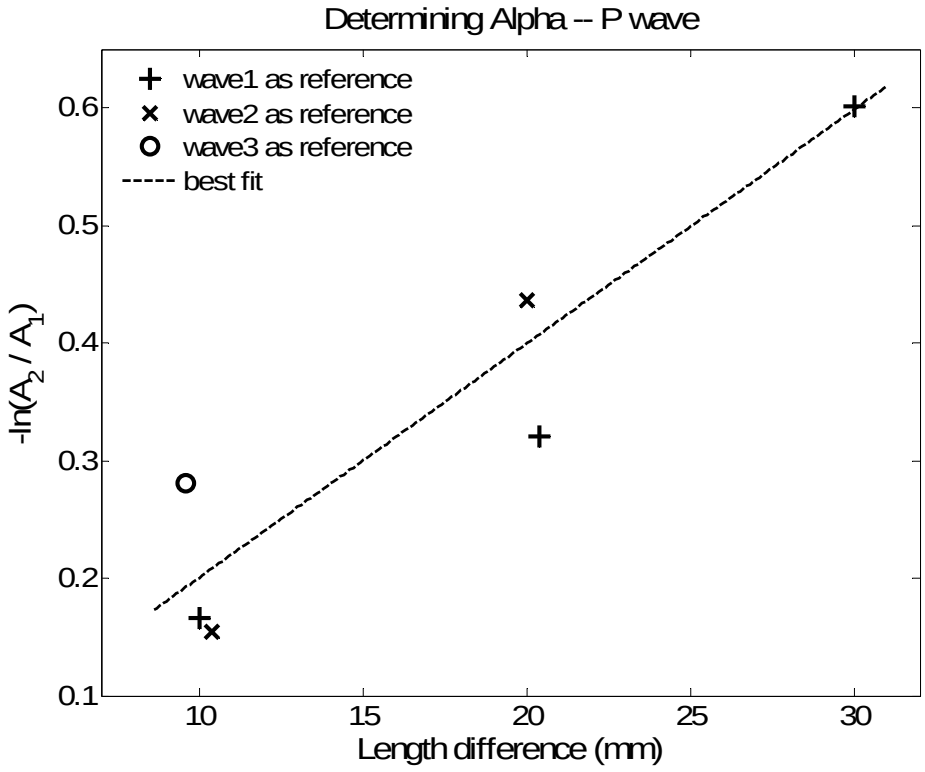

Figure 6.23 Curve fitting among 6 pairs of waveforms to find α_p of P wave (shown is for dominate frequency only, 1.095 MHz in this case. In legend, "wave1 as reference" represents spectral ratio between wave2/wave1, wave3/wave1 and wave4/wave1, the same nomenclature applies to the rest)

In Figure 6.23 , α_p is calculated only at the center frequency as an example. Adapting Equation 6.14 to a realistic case in the lab, spectral ratio of two waveforms' amplitude spectra can be written as:

$$Y' = -Ln\left[\frac{A(\omega, x_2)}{A(\omega, x_1)}\right] = \alpha(\omega)\cdot(x_2 - x_1) + Int \qquad 6.15$$

where *Int* is the intercept which is expected to be a small number, and is not of the interest here. The result for the P wave at 1.095 MHz is:

$$\alpha_p = 19.91 \ (/\text{m}) \qquad 6.16$$

And the error in α_p is calculated by the maximum and minimum slopes, which yield numeric values of 15.82 and 23.99 in this case.

An extended calculation of P wave attenuation coefficient α_p and its error in a frequency band of 0.6~1.4 MHz is shown in Figure 6.24 b. The P wave velocity is calculated from only two waveforms (with sample length 20 mm, 30 mm) and Q_p are calculated from Equation 2.4 with error propagated from α_p (Figure 6.24 a, c). As one can see, in the frequency band around the characteristic frequency from 0.6 MHz to 1.4 MHz, the phase velocity V_p presents only 0.5% variation, which indicates that dispersion is small. This is beneficial when this type of acrylic is used as buffer for its small degree of dispersion. The attenuation coefficient α_p increases with frequency and reaches a peak at 1.221MHz. This increasing trend with a limit is in agreement with the bulk viscosity incorporated viscoelastic model. However, since the bulk / shear viscosity ratio of acrylic is unknown, and the simulation done in section 5.3 incorporates only 4 elements, a realistic interpretation of relating simulation results and lab measurements is not feasible to perform now. At current knowledge, one could expect a fitting model with more complicated configuration as might be suggested by a Wuenschel (1965) type model composed of many elements with a distribution of relaxation times.

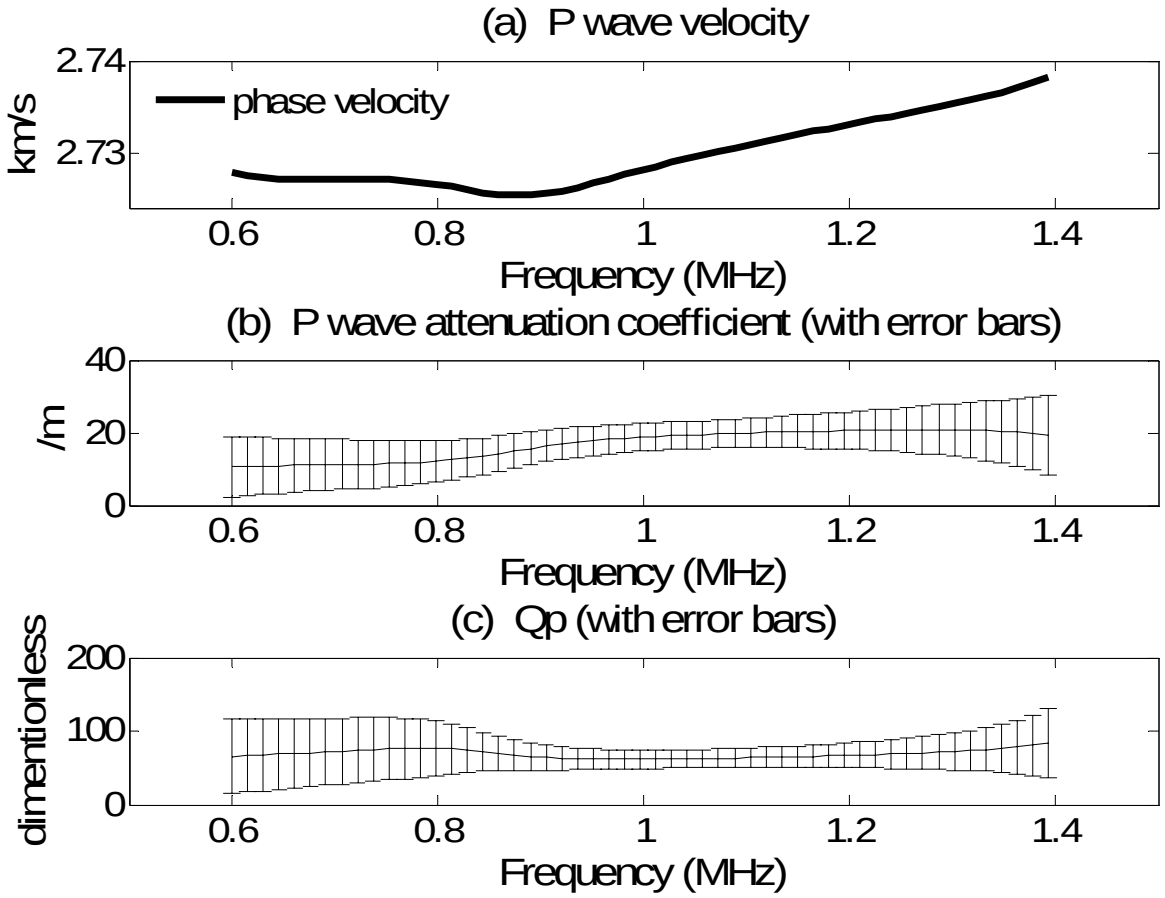

Figure 6.24 P wave velocity, attenuation coefficient and quality factor

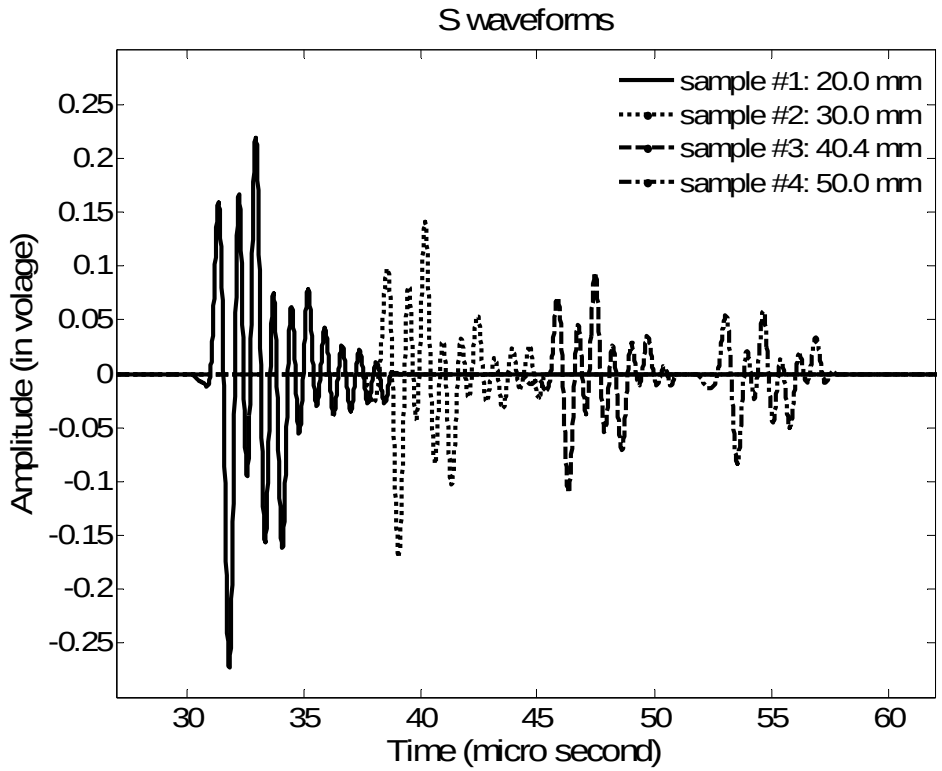

Figure 6.25 S waveforms through acrylic samples of different increasing lengths

A similar analysis is carried out for the S wave observed on the same samples with a variety of lengths. Shown in Figure 6.25 are the waveforms. As one can see, higher order of ringings disappear as sample length increases. This indicates that the S wave is more easily attenuated than the P wave. Other than amplitude decay, phase shift is more obvious (i.e. longer travel time, transform between peak and trough). This is not surprising as the S wavelengths are much shorter and the phase shift is necessarily greater for a similar propagation distance.

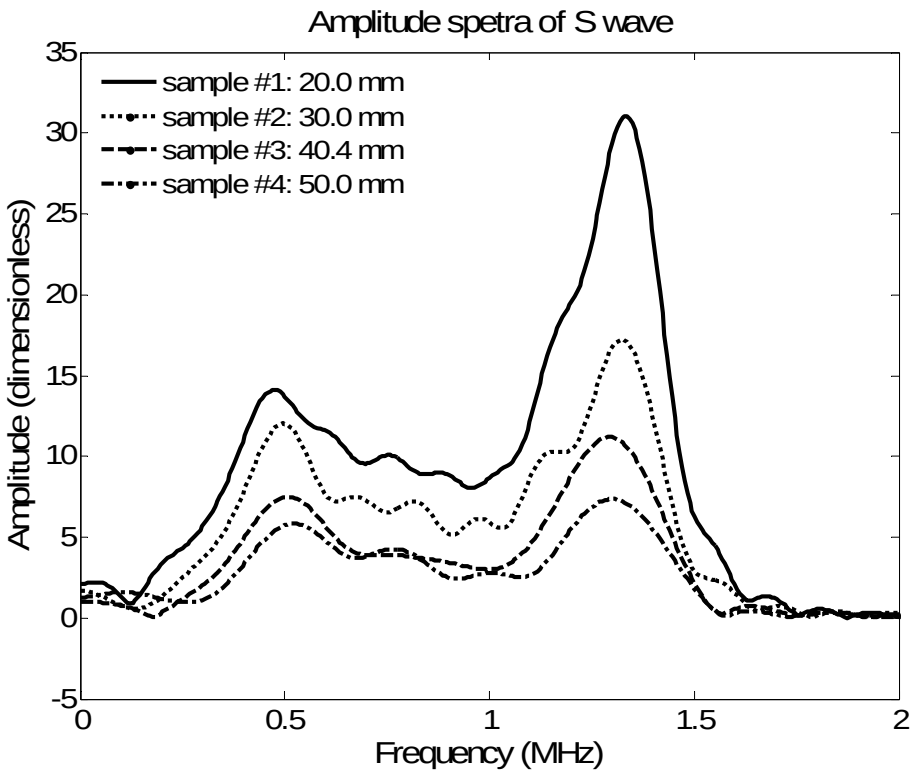

Figure 6.26 Amplitude spectra of S waveforms

The S wave amplitude spectra are also calculated in Figure 6.26. For the same reason as the P wave, the center frequency is shifted to 1.312 MHz, and the primary and secondary amplitude peaks lose contrast when sample length increases. These facts undermine the quality and accuracy of S wave compared to P wave.

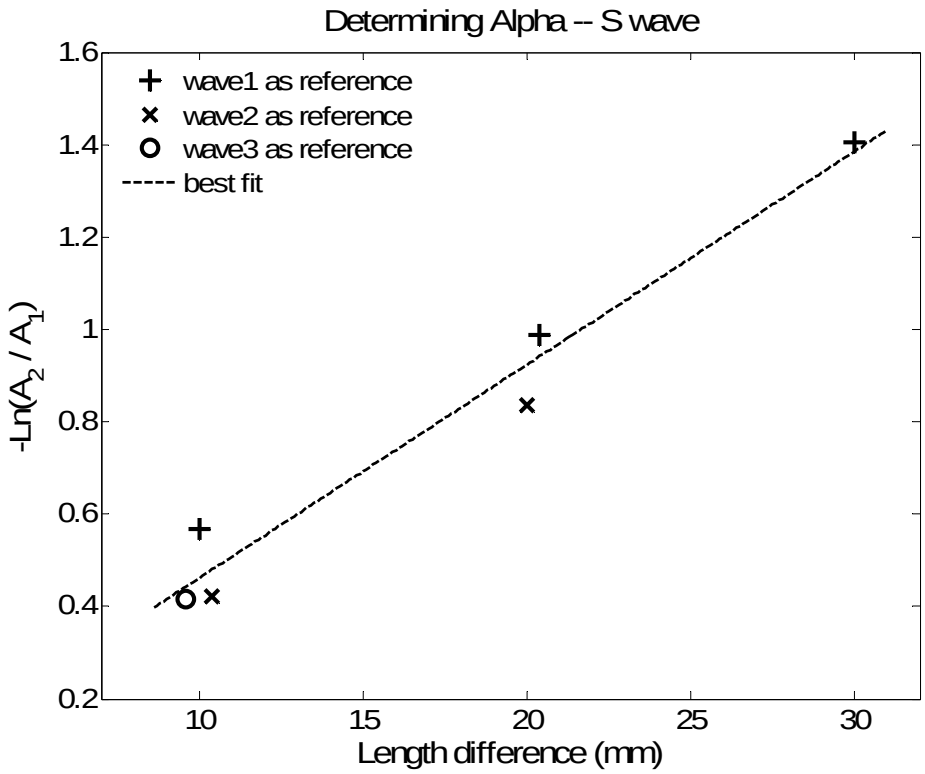

Figure 6.27 Curve fitting between each pair of waveforms to find alpha of S wave (shown is for dominate frequency only, 1.312 MHz in this case)

As is did to the P wave, the attenuation coefficient of S waves is found for the shifted center frequency of 1.312 MHz as an example (Figure 6.27):

$$\alpha_s = \quad 46.16 \ \ (/\text{m}) \qquad 6.17$$

with minimum and maximum slopes 30.55 and 56.76 at the same frequency. This calculation is extended to 0.6 MHz ~ 1.4 MHz in Figure 6.28 b.

The S wave velocity V_s and quality factor Q_s are calculated from the first two traces (with sample length 20 mm, 30 mm) and plotted in Figure 6.28 a, c. In the frequency band around the center peak, the phase velocity still does not vary much (1.5% variation), the values are nearly half of the P wave velocity. This indicates again that dispersion is small over this frequency range for both P and S waves. α_s increases until it reaches a local peak of 52.78 /m at 1.111 MHz. Q_s shows a complicated curvature, with minimum of 47.88 at 1.111 MHz (coincides with α_s peak), and maximum of 75.27 at 1.233 MHz which is close to

characteristic frequency 1.312 MHz.

The above P and S wave results outline the method of calculating attenuation coefficient in a complex experimental environment. The analysis of a real sample with similar impedance should follow a similar routine. The results on a real oil sand are expected to display lower signal quality and higher signal noise ratio. The S wave is usually more difficult to measure than the P wave.

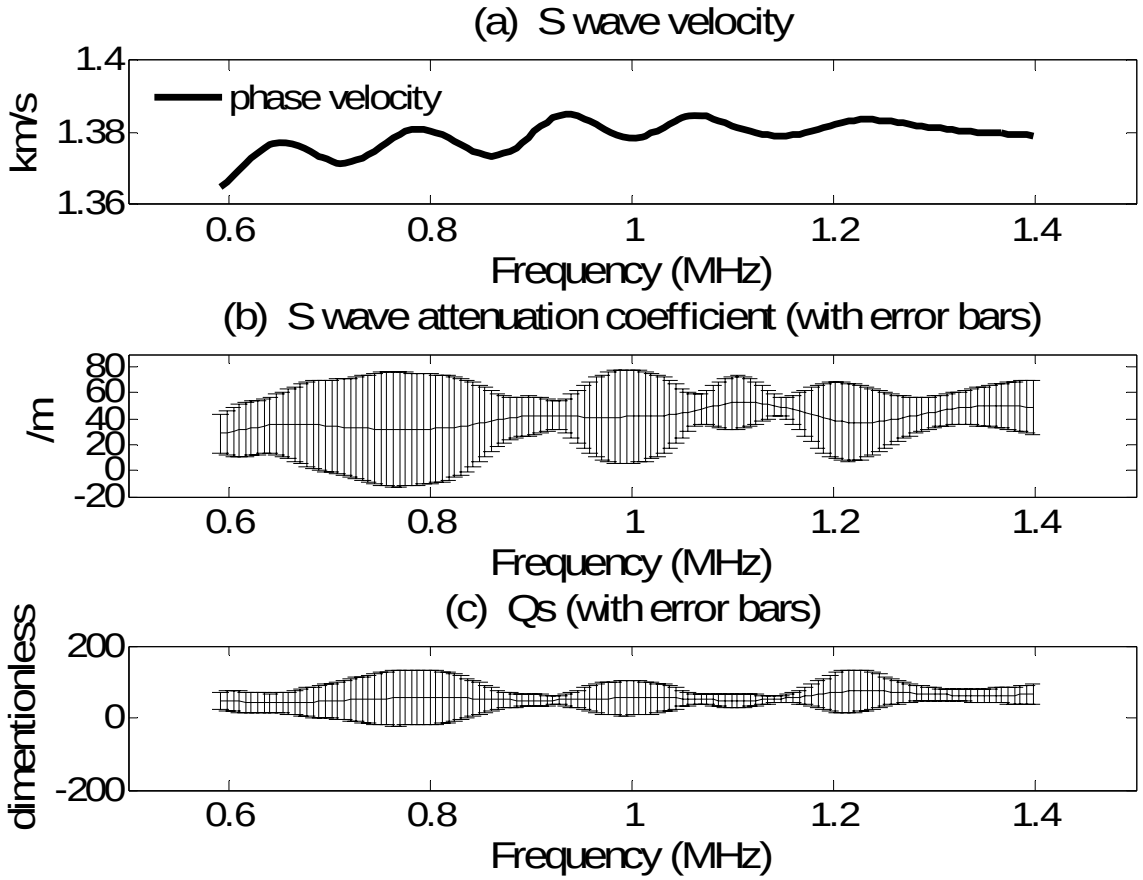

Figure 6.28 S wave velocity, attenuation coefficient and quality factor

Chapter 7
Sample Characterization and Preparation

In this chapter, the real rock samples measured are described. The first two samples consist of weakly consolidated sandstones taken from core and ore , the third sample is reconstituted oil sand material. The characterization includes SEM imaging, bulk and grain density measurements and mercury porosimetry.

7.1 Geological Background of Samples

Sandstone and oil sand materials used in this study were taken from cores obtained during drilling of the Bakken formation of west-central Saskatchewan. This formation is geologically the same as that called the Exshaw formation in Alberta that was deposited over a period spanning the end of the Devonian and the beginning of the Mississippian periods. Interestingly, a rich organic shale that lies at the bottom of this formation has recently been dated by to be 358 ± 10 Ma by University of Alberta researchers using a novel Re-Os technique (Creaser et al., 2002) Figure 7.1 shows the stratigraphic column focused this time period with the Alberta and Saskatchewan equivalent names. The age is further constrained by an underlying volcanic tuff dated to 363 ± 0.4 Ma.

This formation is actively being produced using a variety of production techniques (Lines et al., 2005, Lines and Daley, 2007) that include cold production and enhanced oil recovery. As such, this material will be of interest in future studies.

This material represents oil free and oil saturated sands of this formation, the depths and the well locations from which the samples were obtained is given in Table 7.1. It must be pointed out, however, that there are often many problems with core that would need to be accounted for. The problems with the saturated material include poor consolidation that increases the propensity for drilling induced damage, and the loss of the more volatile components. The loss of volatiles can in some cases produce a high degree of damage during depressurization as gases exsolve from the pore liquids (Wong and Maini, 2007).

Table 7.1 Depth of Samples

Sample	Depth (meter)	Length of sample (mm)
R010 a	825	17.00
R010 b	825	42.00
Reconstituted oil sand	826.40-827.90	22.40

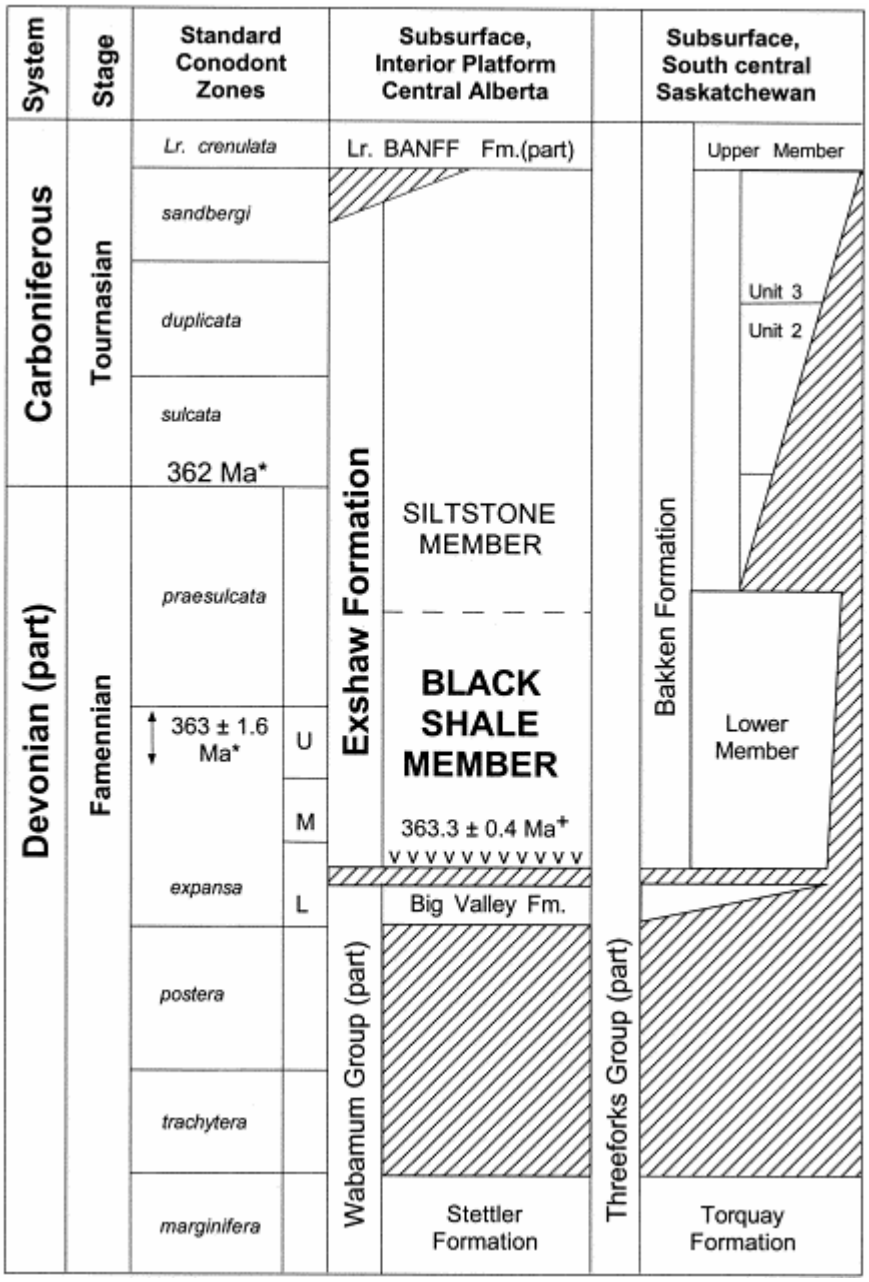

Figure 7.1 Western Canada Sedimentary Basin stratigraphy from central Alberta and south central Saskatchewan from Creaser, et al., (2002) with the permission of Elsevier Ltd.

7.2 SEM scans

In order to better understand the grain structure of samples under study, SEM photos was taken on both unwashed and washed oil sand samples and sandstones.

SEM is abbreviation for the Scanning Electron Microscope which makes use of electrons as detector to create high resolution image of specimen surface. By shooting a series of electrons across the specimen, SEM is able to detect and image closely spaced microscopic features at high magnification. These microscopic features are usually too small to be detected and imaged by conventional light based microscope, and this advantage results in SEM's wide use in material science.

Most SEM instruments require conductivity on the surface of the specimen. This is achieved by coating the specimen with thin film of gold powder in vacuum. During SEM imaging, an electron gun emits a beam of electrons through a series of scan lenses in a column, in this way, the beam is focused on a very fine spot on the specimen. At the end of the column, a set of scanning coils are set to control the focus position of the beam, by tuning the coils, these detector electrons can move on the surface of the specimen and eventually collect enough information to create an image. As the electron beam (primary electrons) hits each spot on the specimen, secondary electrons are scattered from the specimen surface. These electrons are collected and accounted for by a detector and sent to an amplifier. The final image is developed from the number of electrons scattered from each spot on the specimen's surface. Because an electron beam instead of multichromatic light is used for imaging, all images are rendered in black and white with white areas representing intense scattering of electrons.

In this thesis, SEM is used to inspect the surface of the sandstone and oil sand samples. Features such as grain shape and size, grain surface, grain-grain contact, pore space and viscous materials trapped within are all within the scope of interest. SEM was done in the Earth and Atmospheric Science department at the University of Alberta.

7.2.1 SEM of washed oil sand sample

Figure 7.2 is an image of washed oil sand sample showing clearly the sparse aggregation. Sand grains maintain their physical shapes and are isolated from each other; the sands that have contact with others are due to remnant oil or clay. Grain shape varies and size is between 50 – 200 micro-meters approximately. The boundary (edge of the grain) is distinguishable, but since it's washed, the undisturbed state of grain-grain contact and pore space is not able to be interpreted at the moment.

Figure 7.3 is an enlarged image showing several individual grains. A "clean" grain is observed in the middle of the image, while others with less distinguishable grain boundary are wrapped with oil or clay to a certain extent.

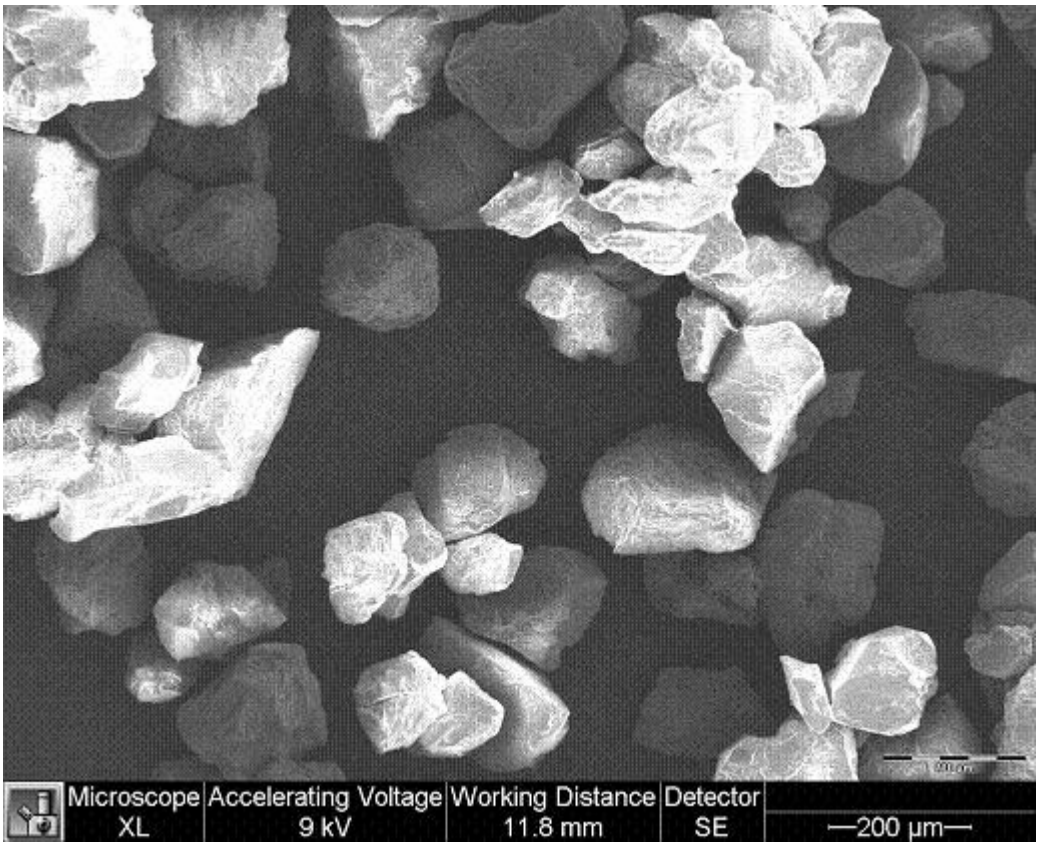

Figure 7.2 SEM of reconstituted (washed) oil sand sample (1433×1075 μm^2 viewing area)

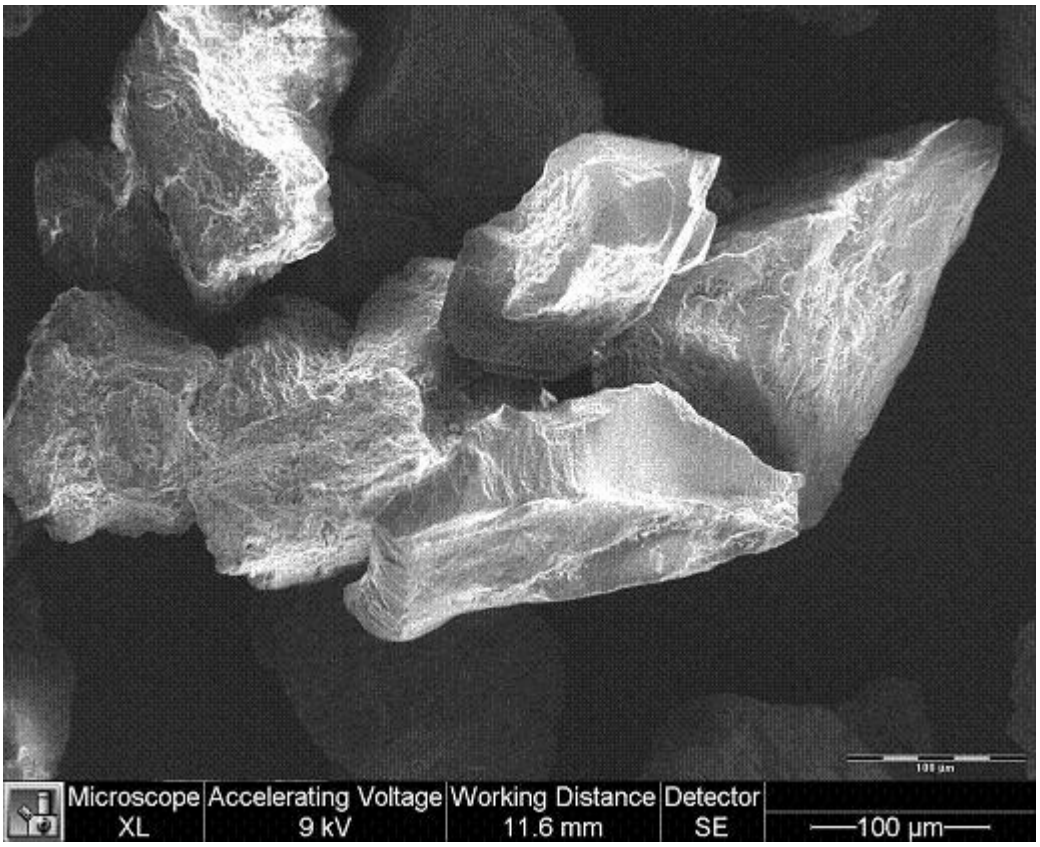

Figure 7.3 SEM of reconstituted (washed) oil sand sample at high resolution (573×431 μm^2 viewing area)

7.2.2 SEM of unwashed oil sand sample

The reconstituted oil sand sample is shown in Figure 7.4. Compared to Figure 7.2, the adjacent sand grains are tightly aggregated, forming clusters with different pore distribution. Higher resolution image is shown in Figure 7.5, as one can observe, sand grains are not apparent after saturation; only the oil wrapped bulk envelope is seen. After a large portion of the pore space is filled with oil, the grain – grain interaction that dominates the sample's attenuation mechanism is expected to give way to the multi-phase (air, oil, solid frame) interaction or largely the highly viscous part of the aggregate.

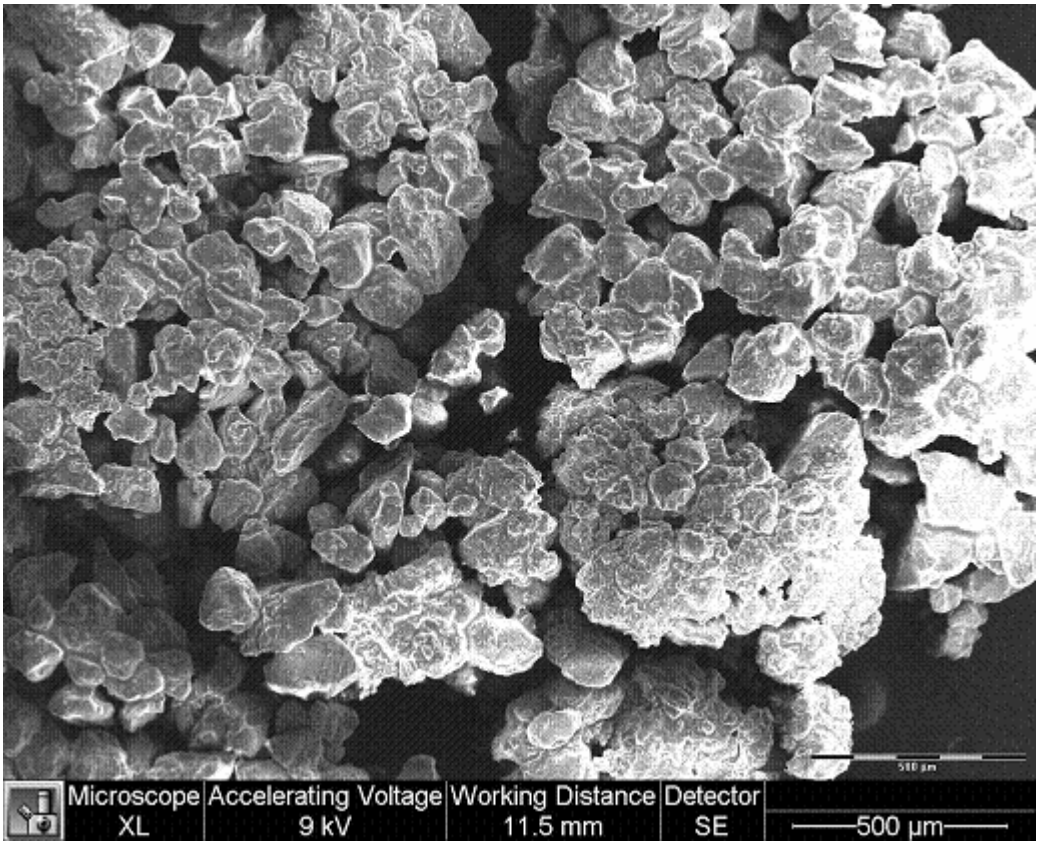

Figure 7.4 SEM of Reconstituted (unwashed) oil sand sample (2389×1792 μm^2 viewing area)

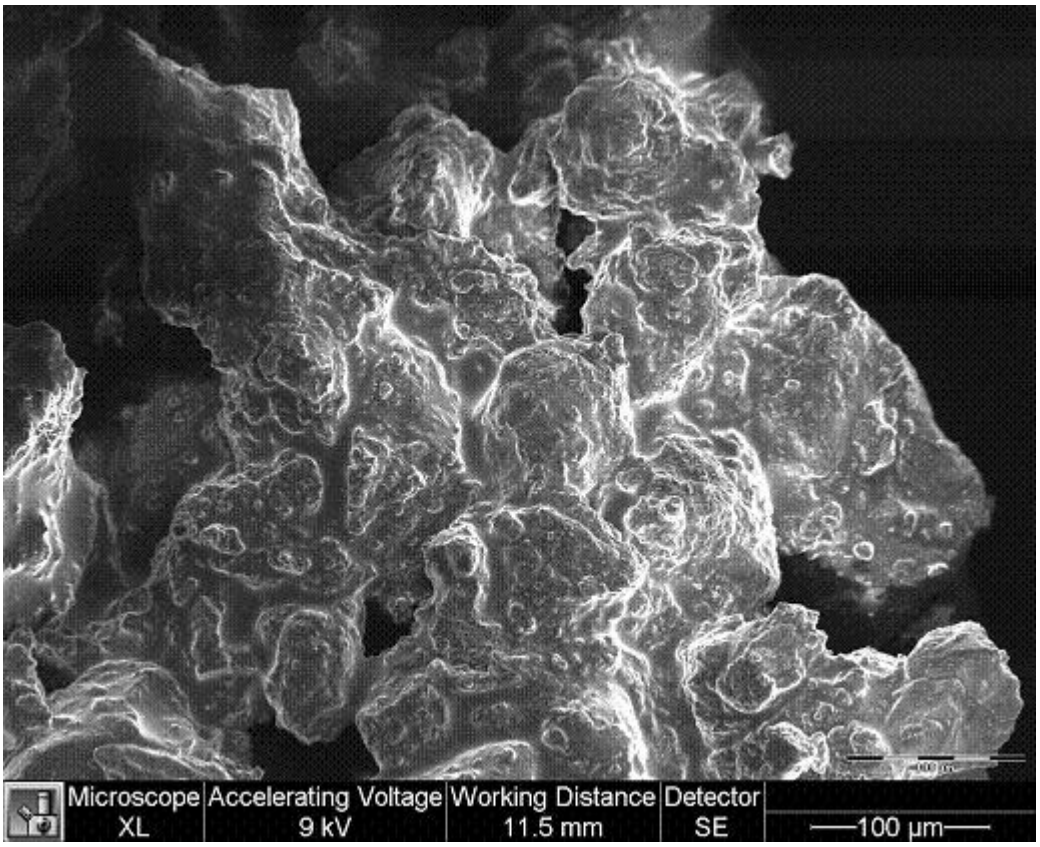

Figure 7.5 SEM of Reconstituted (unwashed) oil sand sample at high resolution (573×431 μm^2 viewing area)

7.2.3 SEM of Sandstone Sample

Sandstone sample R010 is shown in Figure 7.6 and Figure 7.7. Different size of chunks that form this sandstone can be observed. The pore space in this sample varies and a certain amount of them are expected to be closed under pressure. Chunks of R010 is more tightly bounded together compared to washed oil sands (Figure 7.2), and its attenuation mechanism mainly results from the solid frame, instead of viscous phase (e.g. unwashed oil sand, Figure 7.4).

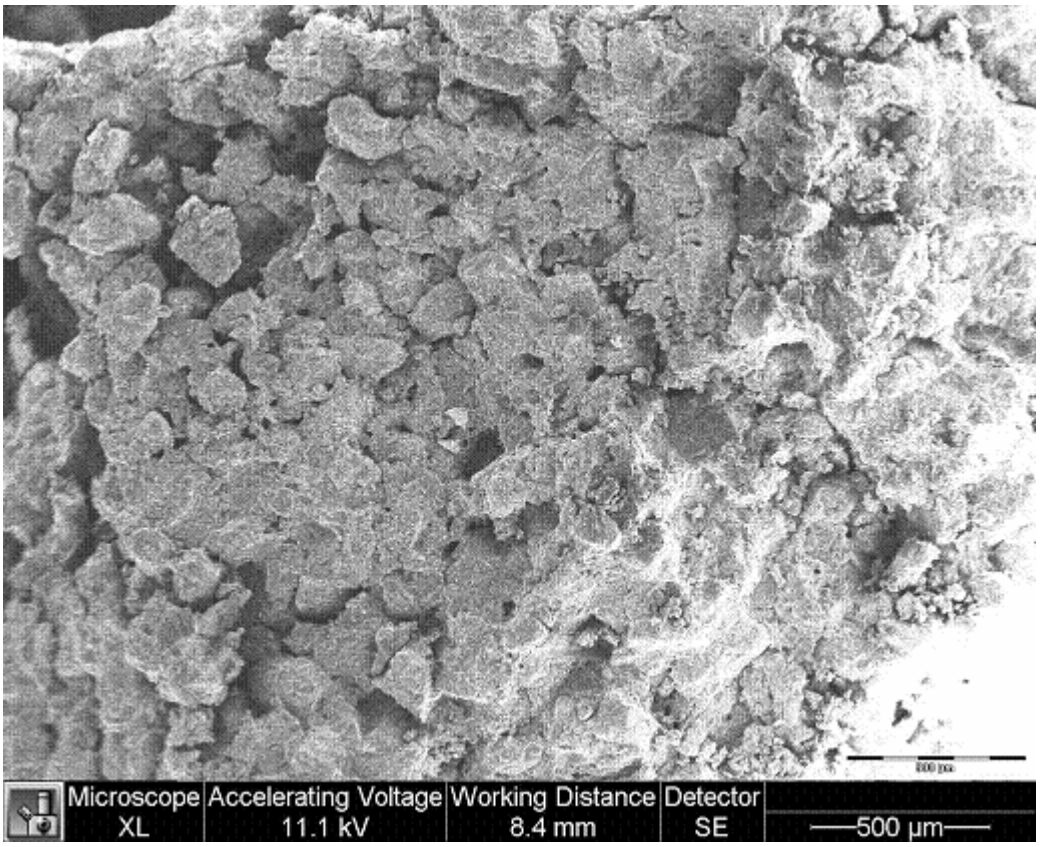

Figure 7.6 SEM of sandstone sample R010 (2866×2150 μm^2 viewing area)

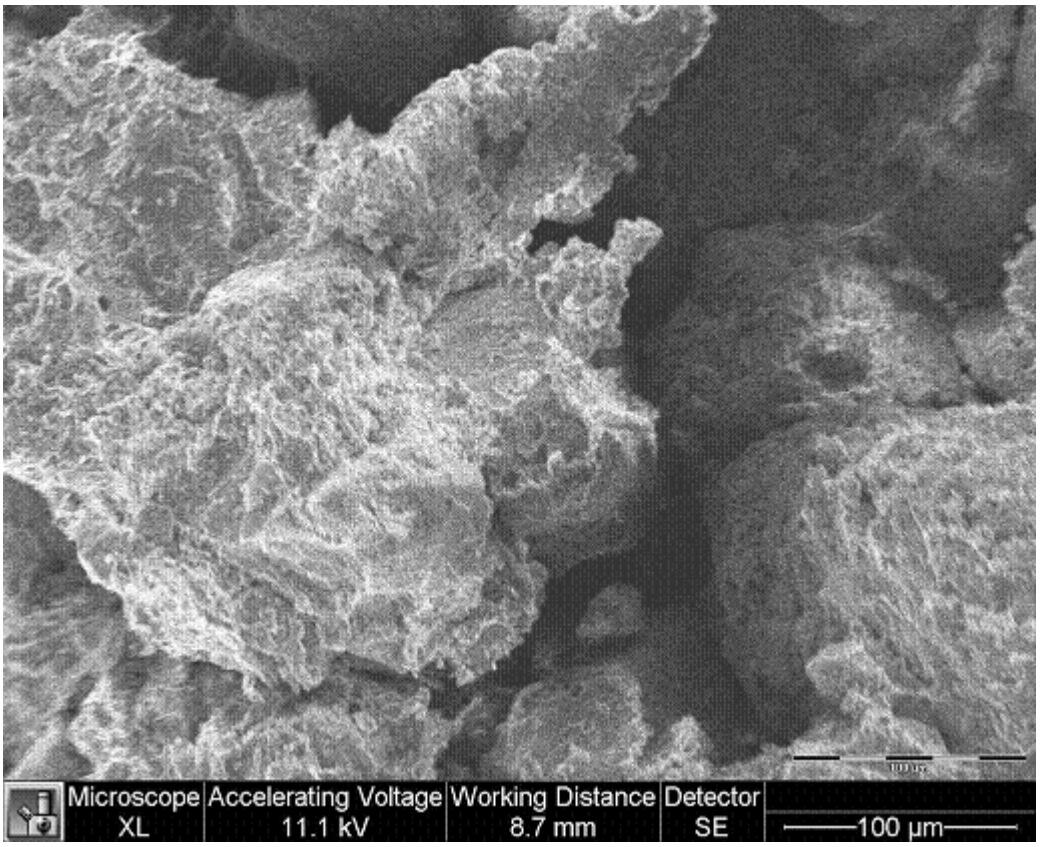

Figure 7.7 SEM of sandstone sample R010 at high resolution (441×331 μm^2 viewing area)

7.3 Densities and Porosity Measurements

7.3.1 Definition

The grain density ρ_g (or skeletal density) is defined by the ratio of the dry mass to the matrix volume:

$$\rho_g = m_d / V_s \tag{7.1}$$

where m_d is dry mass of the sample, V_s is the solid matrix volume of the rock. The grain density is essentially the average density of the solid matrix. For porous media, it is obtained when the measured volume excludes the pores', microcracks', as well as the void spaces between grain particles.

The bulk density ρ_b (or envelope density) can be calculated when aforementioned pore / void spaces are included in the volume measurement. It is therefore, defined by the ratio of the dry mass to its envelope volume:

$$\rho_b = m_d / V_e \tag{7.2}$$

where m_d is dry mass of the sample, V_e is the envelope volume.

The bulk porosity φ is defined as the ratio of the volume of void space to envelope:

$$\phi = V_p / V_e = (V_e - V_s) / V_e \tag{7.3}$$

where V_p is the pore and any other void volume, V_s is the solid matrix and V_e is the envelop volume.

7.3.2 Densities and Porosity Measurement on R010

For solid sandstone sample R010, a mercury porosimeter (AutoPore IV® by Micromeritics®, Figure 7.8) was used to measure pore related features such as porosity, densities and pore structures. By applying different levels of pressure up to 413 MPa (60,000 psi) to a sample immersed in mercury, different size of pores can be detected with an intrusion curve (Brakel, 1981).

Figure 7.8 Mercury porosimeter (AutoPore IV® by Micromeritics®)

Mercury porosimetry is based on the capillary law governing liquid penetration into small spaces. For non-wetting liquids such as mercury, the penetration can be expressed by the Washburn equation (Washburn, 1921), assuming that all pores of the material are cylindrical and connected:

$$D = -\frac{4}{P}\gamma\cos\theta \qquad 7.4$$

where D is the pore diameter, P is the applied pressure, γ is the surface tension of mercury (485 dyne/cm = 0.485 N/m at 25 ºC, Nicholas et al, 1961) and θ is the contact angle of mercury. This pressure – pore diameter relation is plotted in log scale in Figure 7.9.

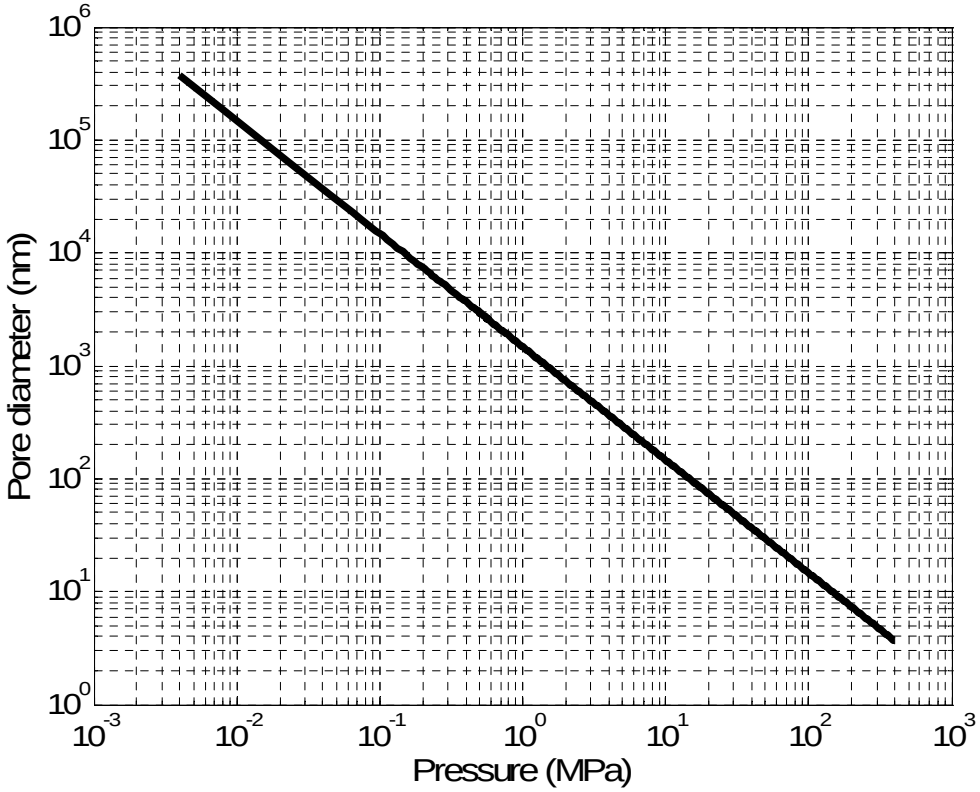

Figure 7.9 Detectable pore throat diameter as mercury pressure increases

As the intrusion pressure increases, mercury is injected into smaller and smaller pore spaces. As is shown in Figure 7.9, the smallest pore size that can be detected by this instrument is approximately 2~3 nm. Although the pores in the real rocks are irregular and are rarely cylindrical, this equation is often used to provide a practical description of pore structure. More accurately, *D* is essentially a measure of the pore throat dimensions which the pressure must overcome in order to push the mercury through.

The cumulative volume of mercury $V_{Hg}(P)$ penetrating the pores is measured progressively as a function of applied pressure. The pore structure of the sample can be estimated by this cumulative intrusion curve (Figure 7.10). During analysis of sample R010, the pore size corresponding to each pressure is calculated from the volume of mercury filled in these pores. Further, by taking the derivative of the cumulative volume of mercury, some features of the proportion of the porosity at a given range of pore dimension was rendered. This is called the incremental intrusion curve via:

$$\partial V'_{Hg} = \frac{dV'_{Hg}}{dP}\Delta P \qquad 7.5$$

where ΔP is the increment of pressure. This curve reveals the relative distribution of the porosity that is intruded at a certain pore dimension.

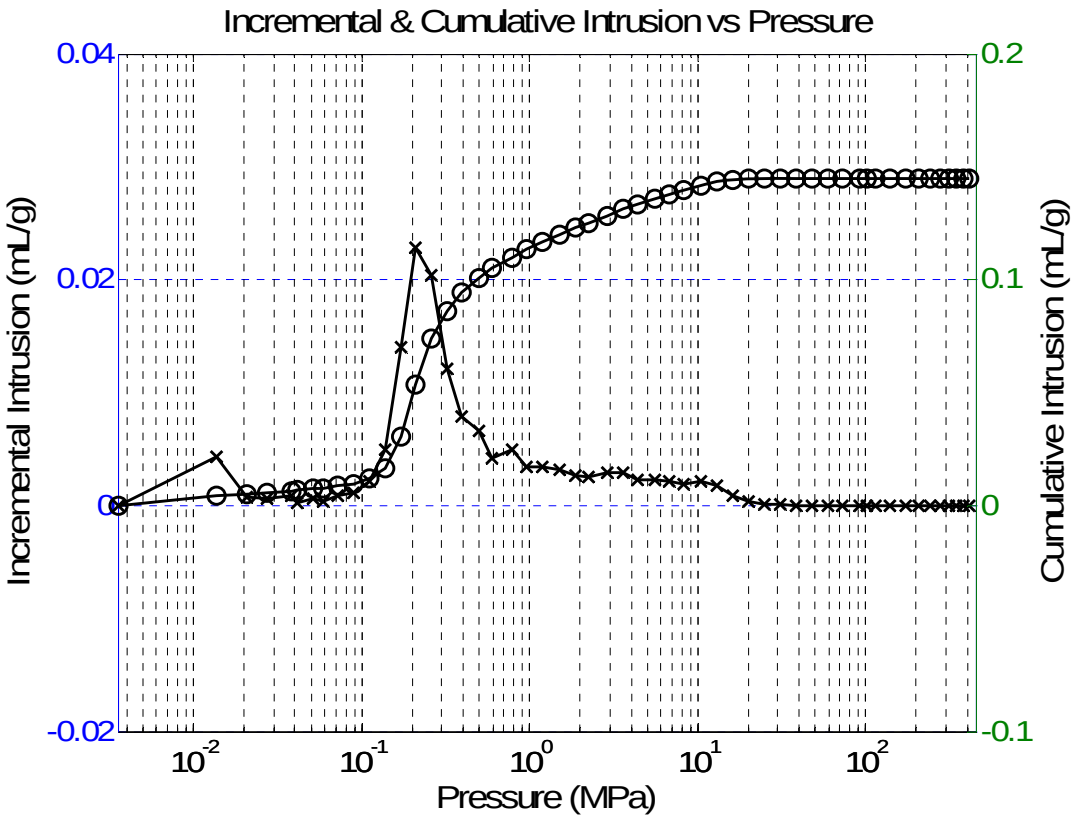

Figure 7.10 Incremental and cumulative mercury intrusion of sandstone R010 as a function of pressure

On the cumulative intrusion curve in Figure 7.10, when pressure is below 0.1 MPa, only 8% porosity has been intruded. This corresponds to larger pores with high cavity to throat ratio (D > 15 μm). When pressure increases from 0.1 to 10 MPa, 90% of the porosity has been intruded. This means a pore distribution from 0.15 to 15 μm forms the major pore structure in this sample. Above 10 MPa, only 2% of the porosity is intruded, indicating a very small amount of tiny pores (D < 0.15 μm). On the incremental intrusion curve, one can find the highest incremental rate at pressure approximately 0.2 MPa, which roughly corresponds to a pore size of 6 μm. This data supplements cumulative intrusion described major pore distribution (0.15 ~ 15 μm), with a dominating pore size around 6 μm. The full data set of mercury intrusion is included in Appendix 1.

The porosity of the sample can also be estimated on the basis of the cumulative volume of mercury injected. However, this will not be the total porosity as only the void space of sufficient dimensions that has been intruded by mercury at the peak pressure will be detected. Nevertheless, it does provide an additional estimation of the porosity of the sample. Errors may lie in the occluded porosity (i.e. those isolated pores not connected in any way to the pore network), which will not be included. And some large pores which can only be accessed via small pore throats maybe missed as well.

The results for sandstone sample R010 are tabulated below:

Table 7.2 Porosimetry Parameters and Results

	Value	Unit
Intrusion Data Summary		
Bulk Density at 0.0035 MPa	1.8756	g/mL
Skeletal Density	2.5766	g/mL
Porosity	27.2047	%
Minimum Pressure	0.0007	Mpa
Maximum Pressure	413.6854	Mpa
Total Intrusion Volume	0.145	mL/g
Pore Structure Summary		
Median Pore Diameter	4.868	μm
Average Pore Diameter	1.0311	μm
Total Pore Area	0.563	m^2/g
Hg Parameters		
Contact Angle	130.00	ºC
Hg Surface Tension	485.00	dynes/cm
Hg Density	13.5335	g/mL

7.3.3 Grain Density Measurement on Oil Sand

For oil sand samples, they are consolidated with either heavy oil or bitumen, therefore to measure its density and porosity in Mercury porosimeter is not feasible. Problem arises from the sand's loose shape that could stuck small diameter pipes in the instrument. Therefore, only the grain density is measured in this section.

Figure 7.11 Helium Multipycnometer (by Quantchrome Instruments, model # MVP-D160-E) for grain density measurement

In order to measure the grain density of oil sand, a Helium Multipycnometer (by Quantchrome Instruments, model # MVP-D160-E) was employed. The principle of this instrument is to measure the pressure change between vacuumed sample and Helium saturated sample, thus the matrix volume is determined by the difference of the two. The grain density is then simply the ratio between the measured dry mass of the solid and this matrix volume.

In operation, a reservoir of Helium gas at known pressure and temperature is connected to a voided and calibrated volume that contains the porous sample. The combined volume available to the Helium is the sum of the original reservoir plus the voided volume less that of the solid matrix of the porous medium. Hence, the matrix volume (V_s, or solid volume) of the sample can be determined from the pressure changes before and after the displacement through PVT equations. The grain density is then simply the ratio between the measured mass of the solid and this grain volume defined by Equation 7.1.

The average grain density of reconstituted oil sand tested under room temperature is 2.00 g/cm^3. Releted parameters used in determining grain densities of both oil sand samples are provided in Appendix 2.

7.4 Sample Preparation

7.4.1 Conventional Preparation of R010

The full core samples are too large in size for lab measurements, therefore, reshaping of core samples are usually needed. For R010, two samples (short sample as R010a and long sample as R010b) are first machined into cubic-like shape, and then worn into cylindrical shape. Top and bottom surfaces are finely flattened to ensure parallelism. The final state of samples are shown in Figure 7.12.

Figure 7.12 Sample R010 with an AA battery as reference (R010a at right hand side while R010b at left hand side)

The P and S wave transducers are adhered on lead foil with silver paint and the foil is then glued on the samples with epoxy. The transducers are installed

separately (Figure 6.6) as discussed in section 6.3. These sandstone samples can be brittle, and the transducers will not be firmly installed with a buffer in between. Hence, in order that the sample is under a minimum disturbance, and can be fastened on both ends, the transducers were installed without a buffer and the whole sample package was then sealed using a urethane putty (Figure 7.13). This is achieved by a cylindrical mold which is larger than the sample package: the sample package is suspended to ensure it locates in the center of the mold, then putty is poured into the mold with no damping material added. The chemical compound of the putty consists of Flexane™ 80 Liquid (Resin and Curing Agent at a ratio of 100:29.87). After curing (usually overnight), the sample is sealed within this coating of urethane with only the wires exposed to connect to the pulser and the oscilloscope. It might be important to note that these two samples maintain the shape – they did not fall apart. Again, the P and S transducers used in this experiment have center frequencies at 850 Hz and 650 Hz, respectively. The confining pressure applied is up to 200 bars.

Samples after preparation are shown in Figure 7.13 with the interior settings showing in Figure 7.14.

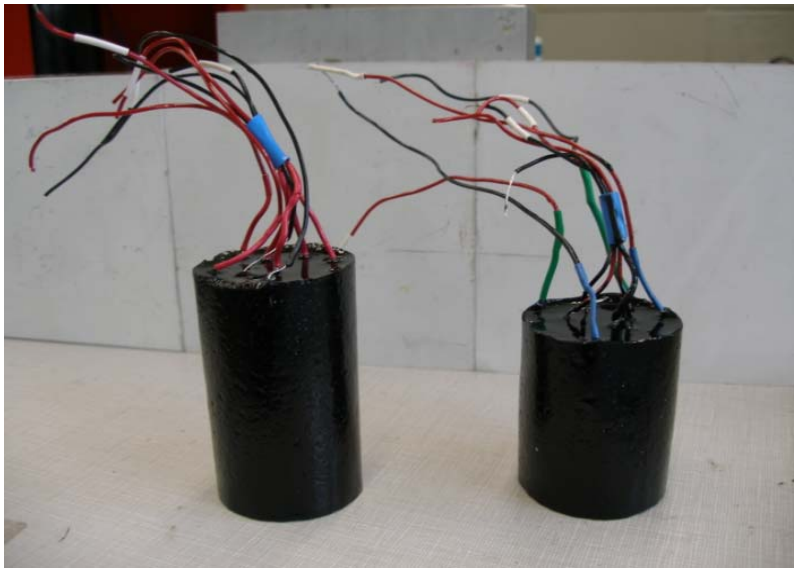

Figure 7.13 Photo of both sandstone samples after preparation (R010a at right hand side while R010b at left hand side)

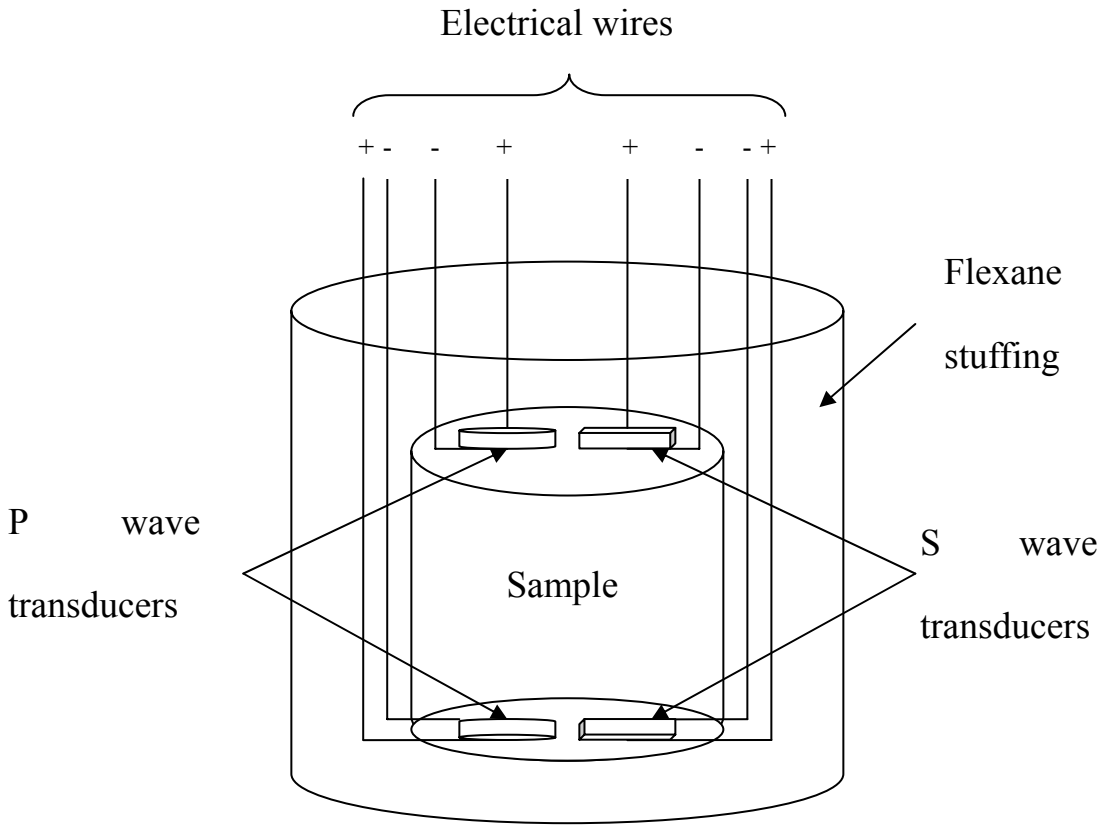

Figure.7.14 Schematic interior settings of samples R010 a / b after sealing

7.4.2 New Preparation of Oil Sand Sample

The second set of samples studied were oilsand which are much more compressible. Therefore, the conventional method fails. In this thesis, a methodology first used by Wuenschel (1965) is modified to adapt to the oilsand samples. First, a plastic pipe (inner diameter of 1 inch) is used to core the sample. One end of the pipe is sharpened in order to drill down; once drilling is completed, then both top and bottom disturbed parts are removed, leaving only the originally saturated part within (Figure 7.15 top right corner). This sample is then placed in a flexible tube (Tygon®) and transducer-buffer pairs described in the previous chapter are installed at both ends (850 kHz for P wave and 650 for S wave, installed in a stack). O-rings and metal clamps are used together with the flexible tubing to ensure perfect sealing. After sealing, the sample piece is then installed in the newly designed length detecting apparatus (Figure 6.13) along the guided rods.

The apparatus was then placed in a pressure vessel and velocity measurements were made up to 25 MPa. This pressure corresponds roughly to the expected *in situ* overburden lithostatic stress on these samples at depths of 830 meters below the surface.

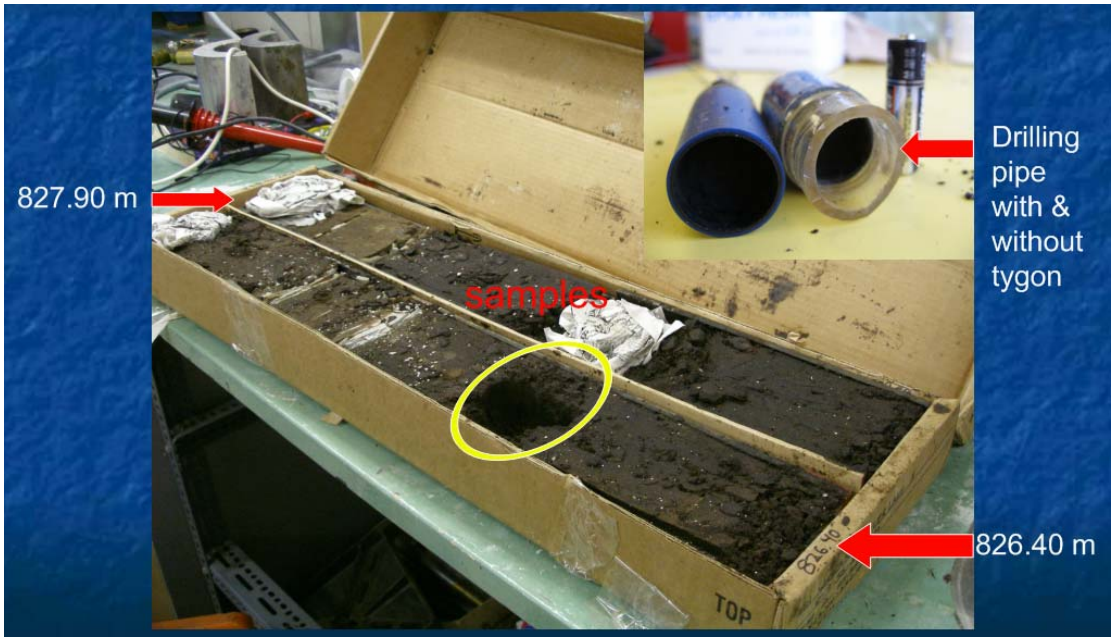

Figure 7.15 Plover lake oil sand section and sample preparation

Chapter 8
Experimental Results and Discussion

8.1 Velocities of Sandstones as a Function of Pressure

Porosity has a large influence on seismic velocity but what is not as well understood is that this porosity leads to a pressure dependence. As such, it is important to try to understand what the velocity might be under different in situ condition. This could be very important in the context of time lapse seismology where changes in the pore fluid pressure will influence the seismic velocity. Velocity variation is always to the interests of geophysicists. Because in the process of oil production, changes of effective pressure in the reservoirs can lead to changes of seismic velocity, layer thicknesses, and fractures in the reservoir sands, rocks and the overburden layers. The understanding of how saturated and less saturated rocks respond to confining pressure can provide important information in interpreting the velocity anomalies in the drilling process and the time shift of time-lapse data.

Under such practical settings, studies have performed on the variation of seismic velocities as a function of confining pressure. Results show that the seismic velocities and the elastic moduli are highly dependent on the differential pressure (i.e. the difference between the confining stress and the pore fluids pressure. Carlson and Gangi, 1995; Khaksar et al., 1999).

Unless the sample is damaged during pressurization, the ultrasonic velocity – pressure relation follows a common trend. The velocity increases rapidly as

confining pressure increases from zero, this is similar to compaction in the upper crust. Then, as the intra- and inter-granular micro-cracks or some small aspect ratio pores close, the rate of velocity change slows. Most micro-cracks are closed above a certain confining pressure. If pressure decreases at this point, the micro-cracks often do not immediately restore to their original volume. As a consequence, on depressurization the velocity does not drop to the original level during the pressurization. And this is why a hysteresis cycle is observed in laboratory.

In this work, the velocity was measured as a function of pressure on three core samples described in the previous chapter. For the less saturated samples R010a, b, the waveforms of both compressional and shear are plotted as a function of confining pressure, shown in figures below.

Figure 8.1 and 8.2 are P and S waves of short sample R010a, while Figure 8.3 and 8.4 are P and S waves of long sample R010b. As shown, short sample yields some signal even at low pressure, while long sample only yields satisfactory results at high pressure. This is partially because of the higher attenuation, and partially because of a natural fracture in the middle of the long sample (observable in Figure 7.12), which undermines the contact of grains at low pressure, thus, the sample is not compact enough to let wave transmit through. The arc-shaped iso-phase is obviously seen, indicating velocity change as pressure varies.

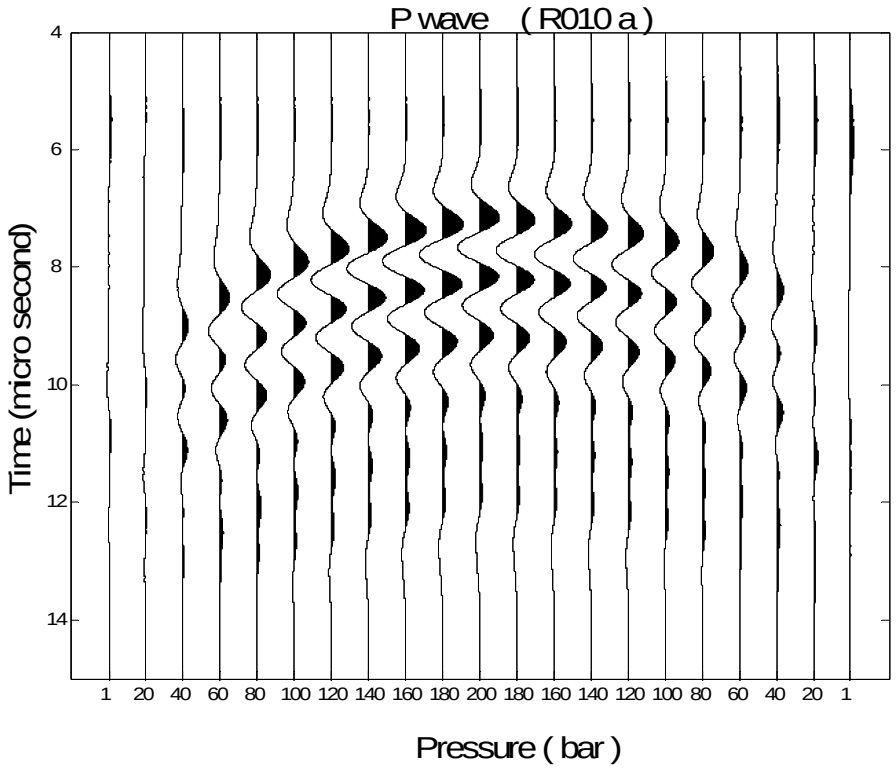

Figure 8.1 Observed P waveforms for sample R010a over a pressure cycle

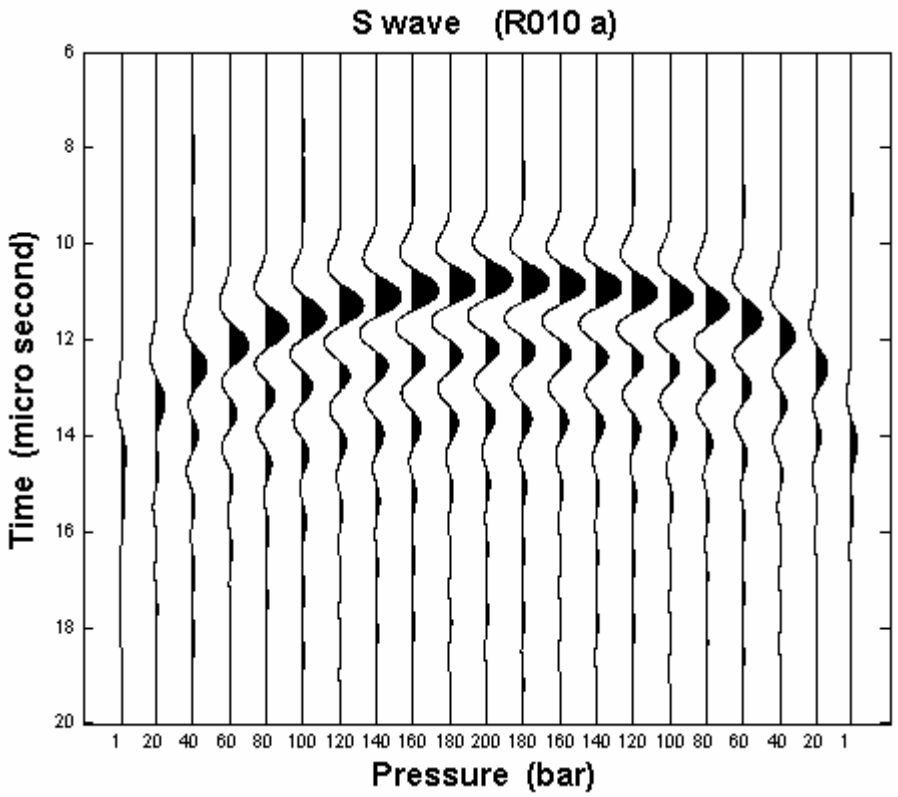

Figure 8.2 Observed S waveforms for sample R010a over a pressure cycle

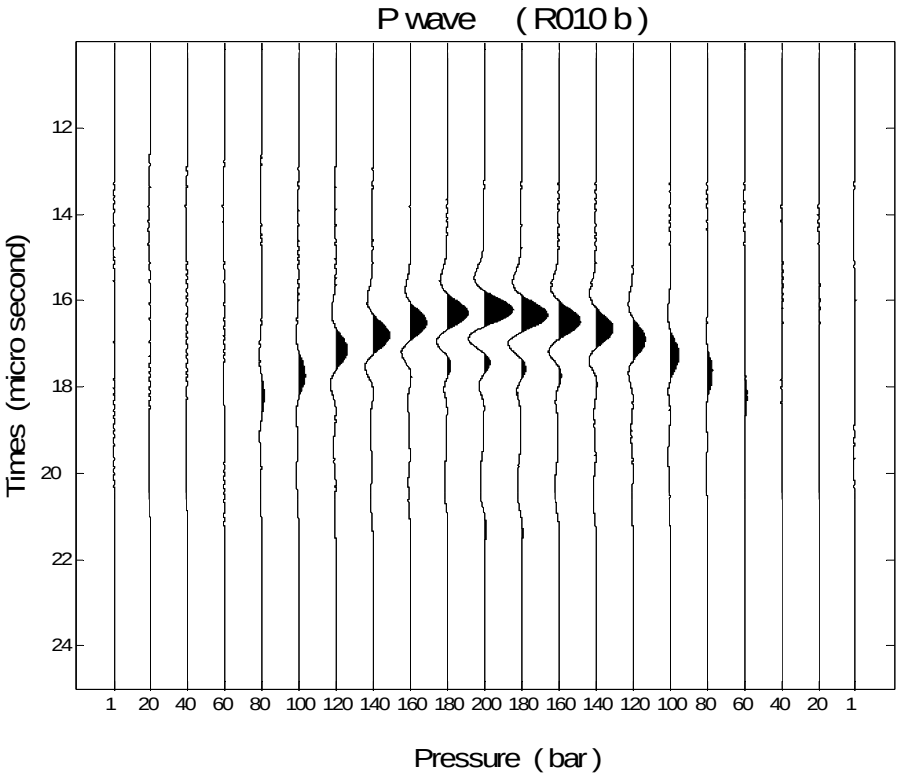

Figure 8.3 Observed P waveforms for sample R010b over a pressure cycle

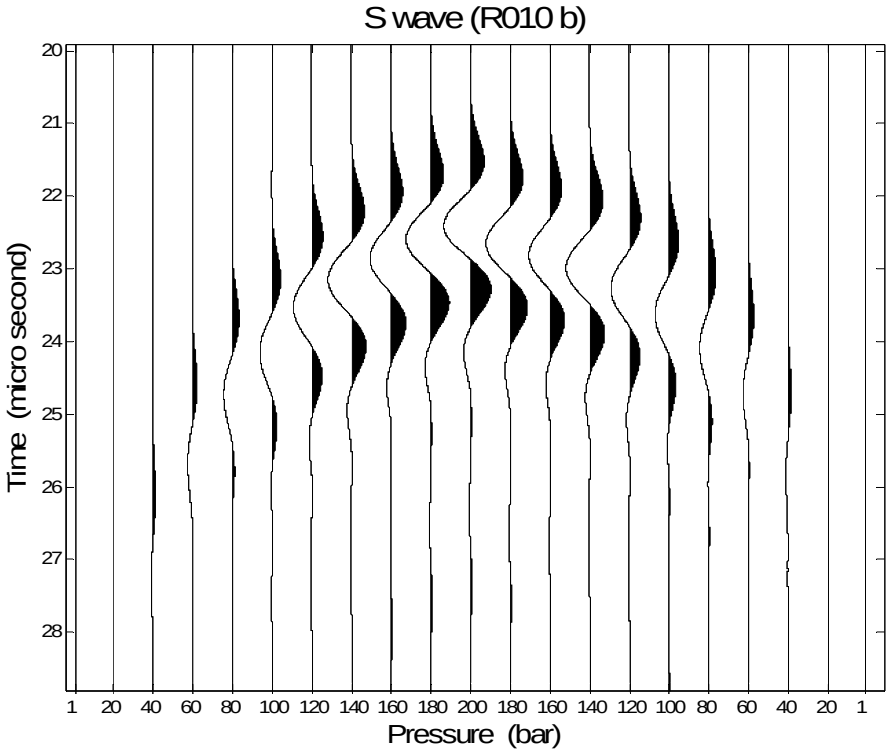

Figure 8.4 Observed S waveforms for sample R010b over a pressure cycle

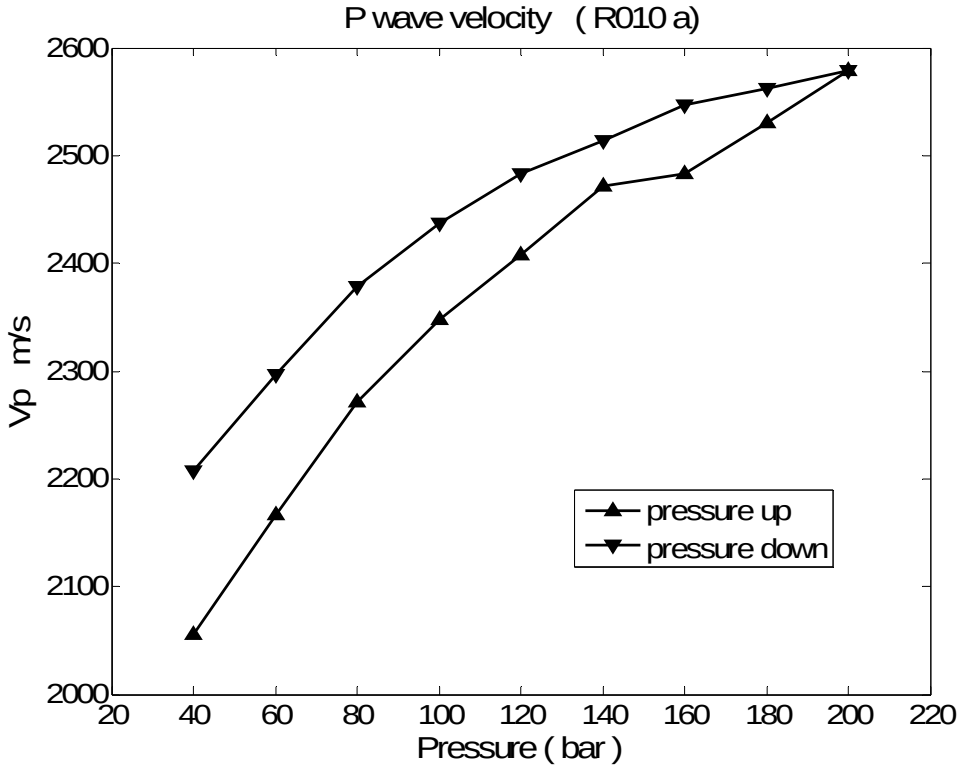

Figure 8.5 P wave velocity of R010a over a pressure cycle

In Figure 8.5 and 8.6, V_p V_s of short sample R010a are plotted as a function of pressure starting from 40 bars. An obvious hysteresis trend is observed, for both waves, which means compaction due to pressure plays a dominant role in moduli enhancement and thus shortens the travel time.

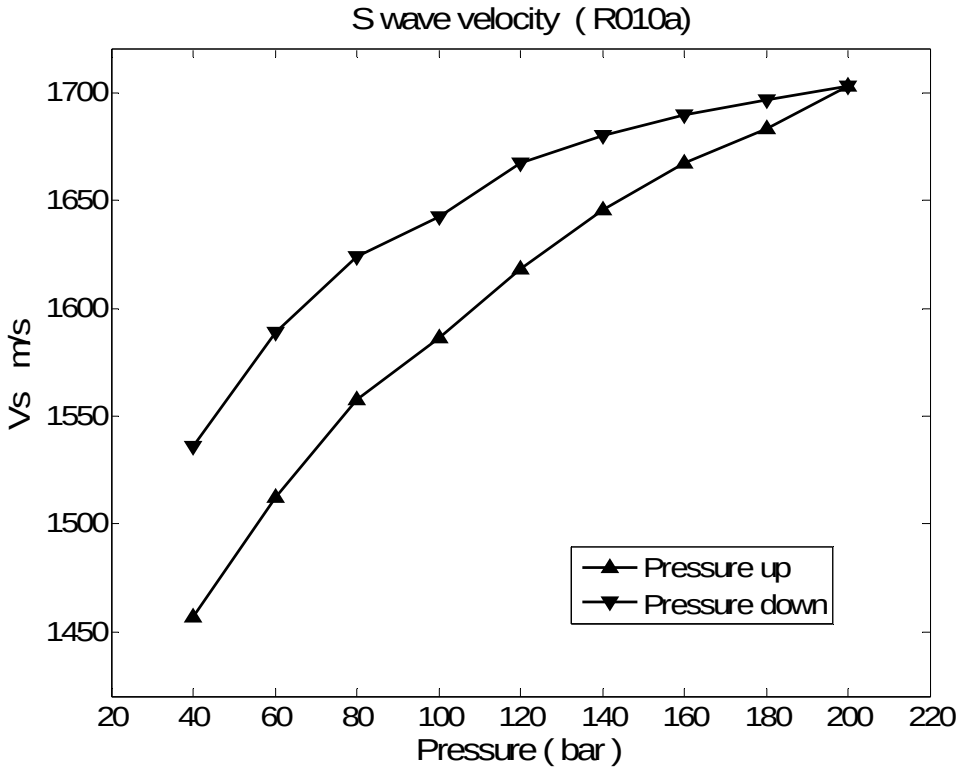

Figure 8.6 S wave velocity of R010a over a pressure cycle

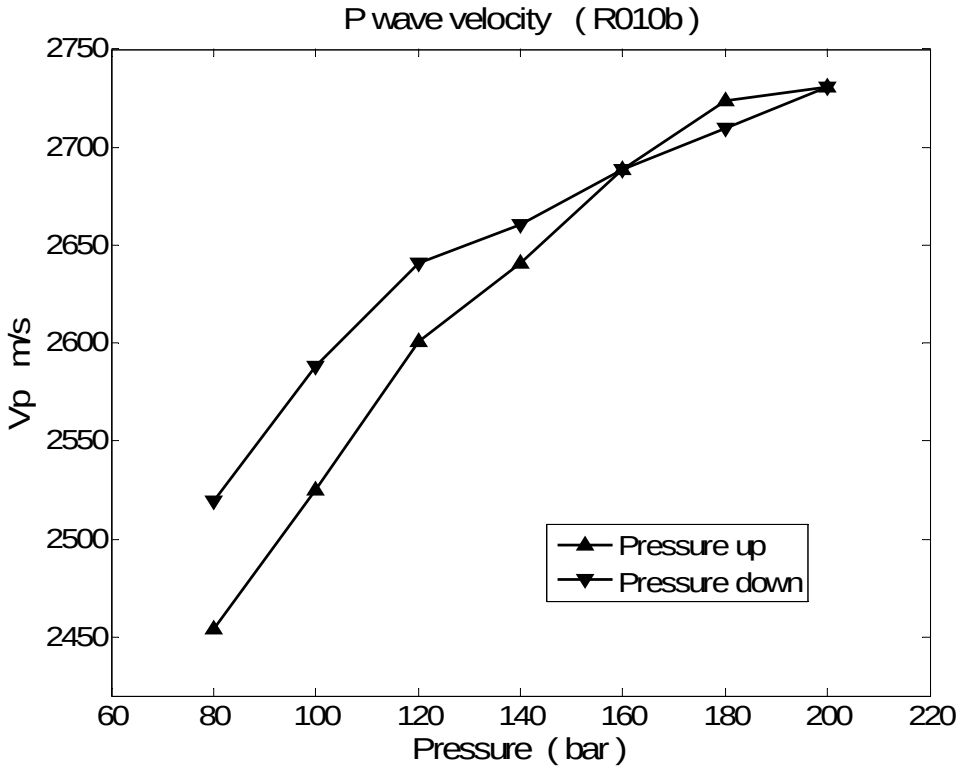

Figure 8.7 P wave velocity of R010b over a pressure cycle

However, for long sample R010b in Figure 8.7 and 8.8, due to low signal quality at low pressure, the V_p V_s curves are plotted starting from 80 bars. Unexpectedly, the velocity hysteresis curves show overlapping at high pressure. Moreover, contrary to tradition remnant high velocity when pressure drops from the peak, V_p drops even lower than the value during pressurization (Figure 8.7, at 180 bars). This is possibly explained by the fracture in the long sample (Figure 7.12). When pressure increases to 180 bars, the fracture is closed due to consistent stress increase, but when pressure drops to the same level, the fracture may open in a sudden, therefore a low velocity is resulted. Below this level, pressure released micro-crack space may counteract the effect from fracture opening, hence, V_p is brought back to a higher level than pressurization values.

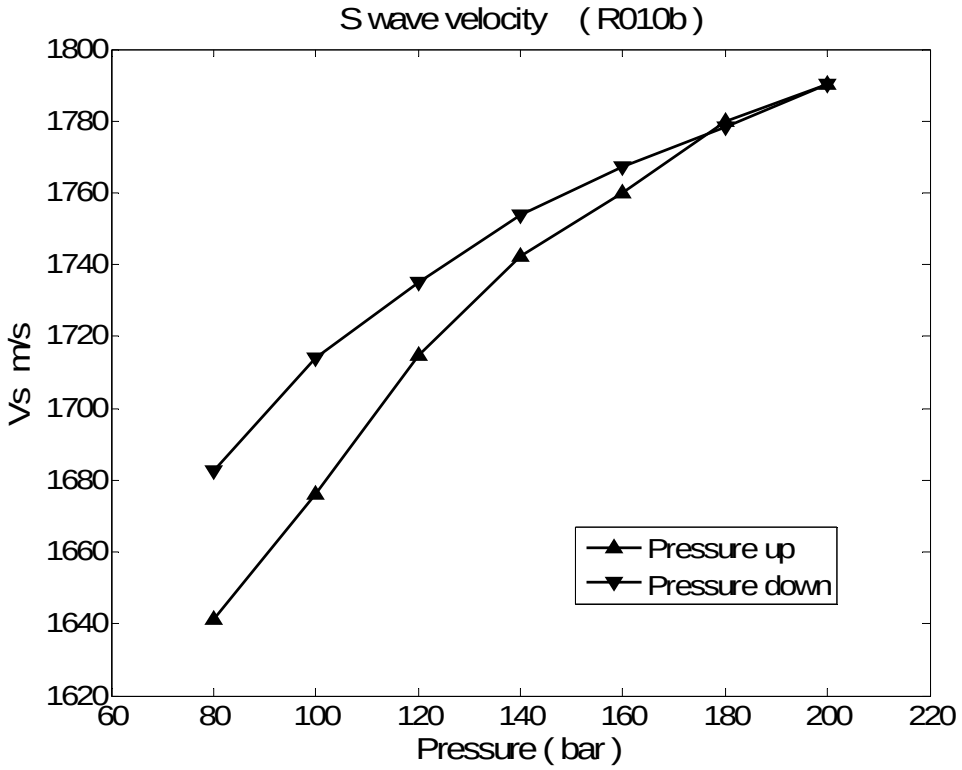

Figure 8.8 S wave velocity of R010b over a pressure cycle

Alternatively, the sample may have been damaged by the pressure that was applied. The damage would result in new micro-cracking and hence lower the velocity.

8.2 Velocities of Reconstituted Oil Sand as a Function of Pressure

Unfortunately, it was not possible to properly sample an undamaged oil sand sample in this study. As such, the new system was tested using reconstituted oil sand material. Tests on undamaged material will have to await future studies.

The attenuation in this material is severe. Shown in Figure 8.9 are two P waveforms. The solid line represents the input signal (through two delrin buffers), and the dashed line represents the received waveform through a 50 mm glass beads sample (as well as buffers). The first waveform has been reduced to one tenth of its original amplitude. As is clearly shown, waveforms are much more attenuated that the spiky pattern is not well retained, the wave period is stretched and amplitude is decreased significantly. Under such circumstance, the acquisition of good quality waveform is a difficult task, particularly for the S wave, whose signal quality is usually worse than that of the P wave. At low pressure (less than 100 bars), there may be no distinguishable signal even for P wave. To increase confining pressure could improve signal-noise ratio, thus yields some signal. But for S wave, measurements are carried out under a high pressure of 200 bars, however, the signal is still not seen from the oscilloscope. This may be due to the low signal-noise ratio, and also could be a low energy transmission problem (most energy may be reflected back instead of transmitting through).

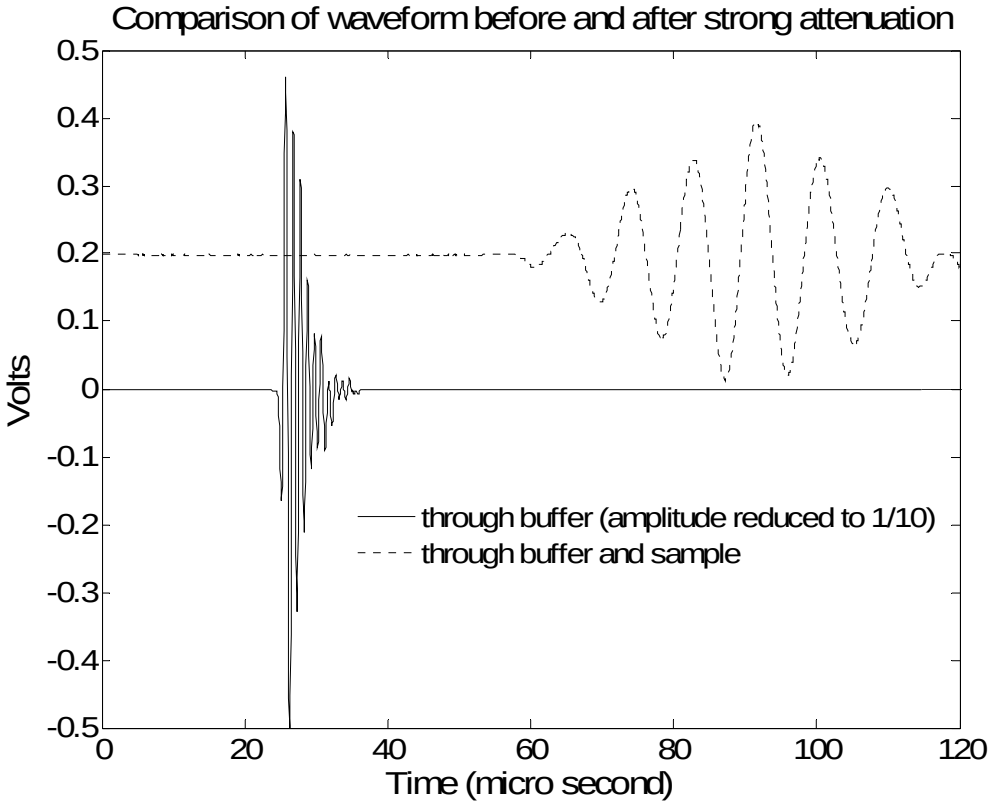

Figure 8.9 Comparison of original and attenuated P waveforms (Delrin buffers are used to propagate signal through a 50 mm glassbead sample. Note that the waveform through only buffers - solid line - is reduced to 1/10 of its original amplitude for display purpose, and the attenuated waveform is plotted 0.2 Volt up for the same sake)

To address the S wave problem, the newly designed apparatus with acrylic buffers is employed. The settings of the acquisition system is listed in Table 8.1. With this system, both P and S waves were obtained in a depressurization process (pressurization process is done without recording because no signal was obtained at low pressure. To test the system in an efficient manner, the confining pressure was raised to 250 bars to check if signal propagates through. Therefore only depressurization process is available in this study).

Table 8.1: Settings of pulser for a 22.4 mm reconstituted oil sand sample

Pulser Parameters	P wave	S wave
PRF	5	5
Gain	45	45
Highpass filter	1 MHz	0.3 MHz
Lowpass filter	out	10 MHz
Energy level	4	4
Damping	0	0

Shown below in Figure 8.10 are the P waveforms and Figure 8.11 are the S waveforms as pressure drops from 250 bars to 50 bars.

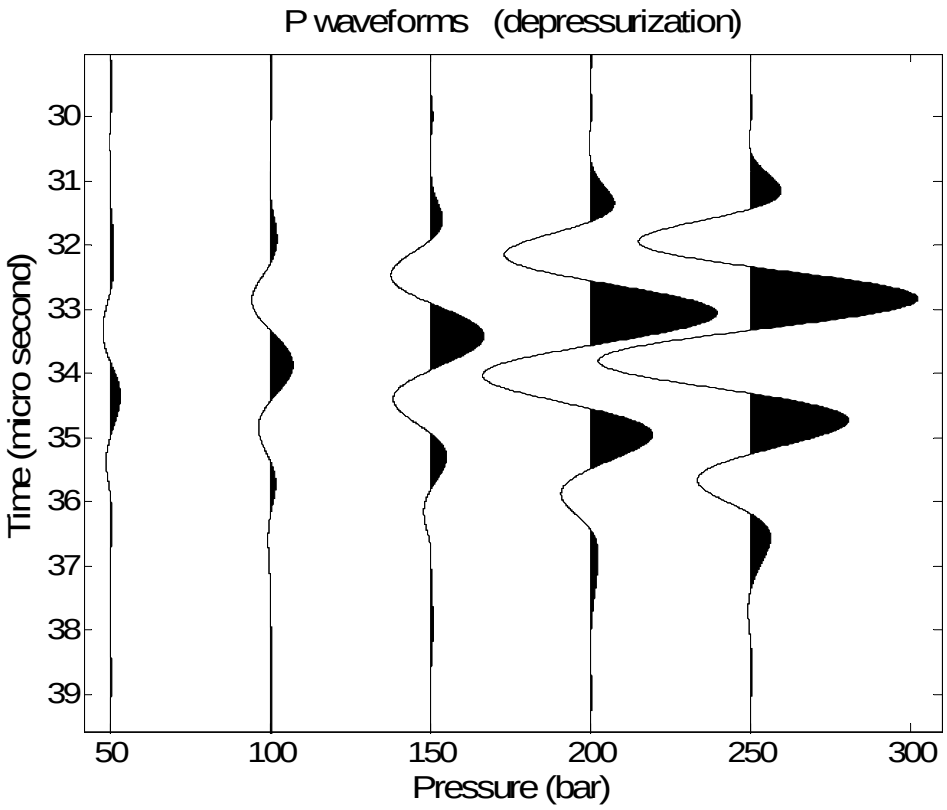

Figure 8.10 P waveforms of reconstituted oilsands (data were obtained in a depressurization process)

The P waveforms (Figure 8.10) display an obvious dependence on the confining pressure. The amplitude and travel time both change in an expected manner. This means during the depressurization process, the opening of pores and cracks dominates the modulus and density change. The results match the classic pressure dependency mechanism. However, for the S waveforms (Figure 8.11), the travel time follows the way predicted by such mechanism, but amplitude does not. It decreases from 150 bars to 50, but increases as pressure drops from 250 bars to 150. This is unexpected and the reason is not known.

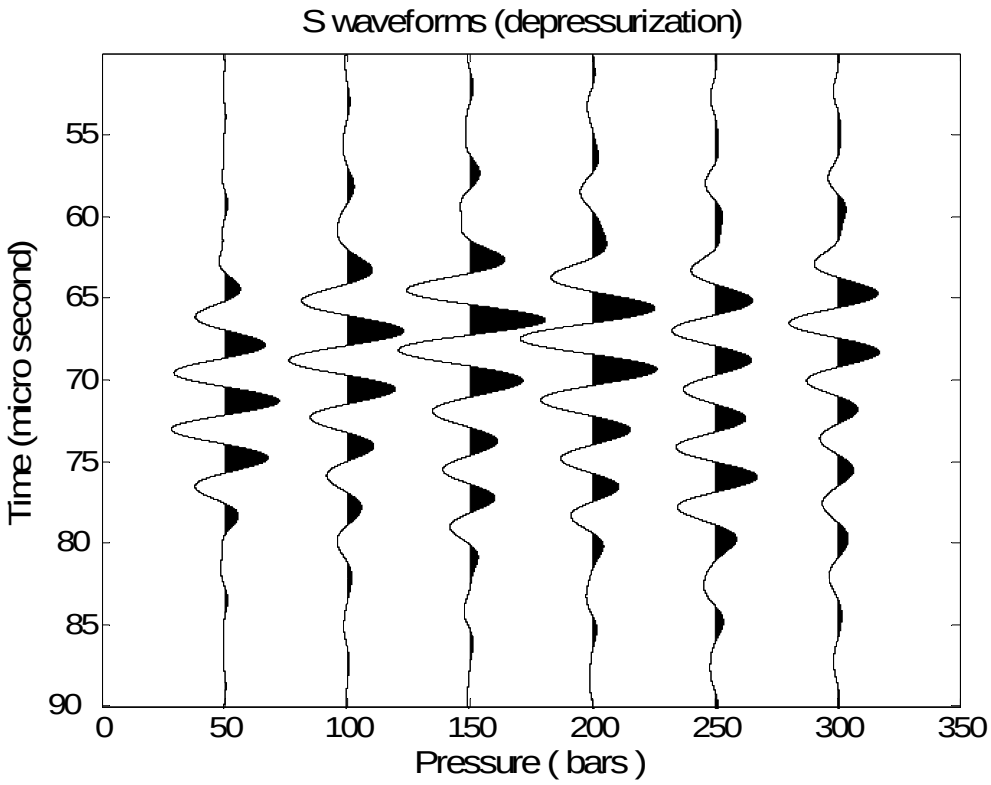

Figure 8.11 S waveforms of reconstituted oilsands (data were obtained in a depressurization process)

At this stage, a theory of comprehensive concerns is not proposed yet, so the study is limited to wave velocity variation only. In Figure 8.12, the pressure introduced length change is presented as well as density change. As one can see, pressure drop at low pressure level forms the major portion of length change. Sample length (represented by hollow triangles) restores from 20.69 mm to 22.4mm with a decrease of pressure from 50 bars to room pressure. When pressure drops from 250 to 50 bars, it was expected that length increases due to pressure released pore opening, but it is not the observation in this experiment. Sample length increases for unknown reason though the variation is only 0.4%. Density change is also shown, which is calculated by:

$$V_i = V(1-\Delta L_i/L)^3 \qquad 8.1$$

$$\rho_i = m / V_i \qquad 8.2$$

where sample volume V = 11.34 cm^3, original length L =22.4 mm and mass m = 21.12 grams.

This assumes that the sample compresses isotropically and that the linear strain is given by $\Delta L / L$.

The bulk modulus can be calculated by:

$$K = -\frac{pL}{3\Delta L} \qquad 8.3$$

And the result for oil sand is 2.18x10^7 Pa

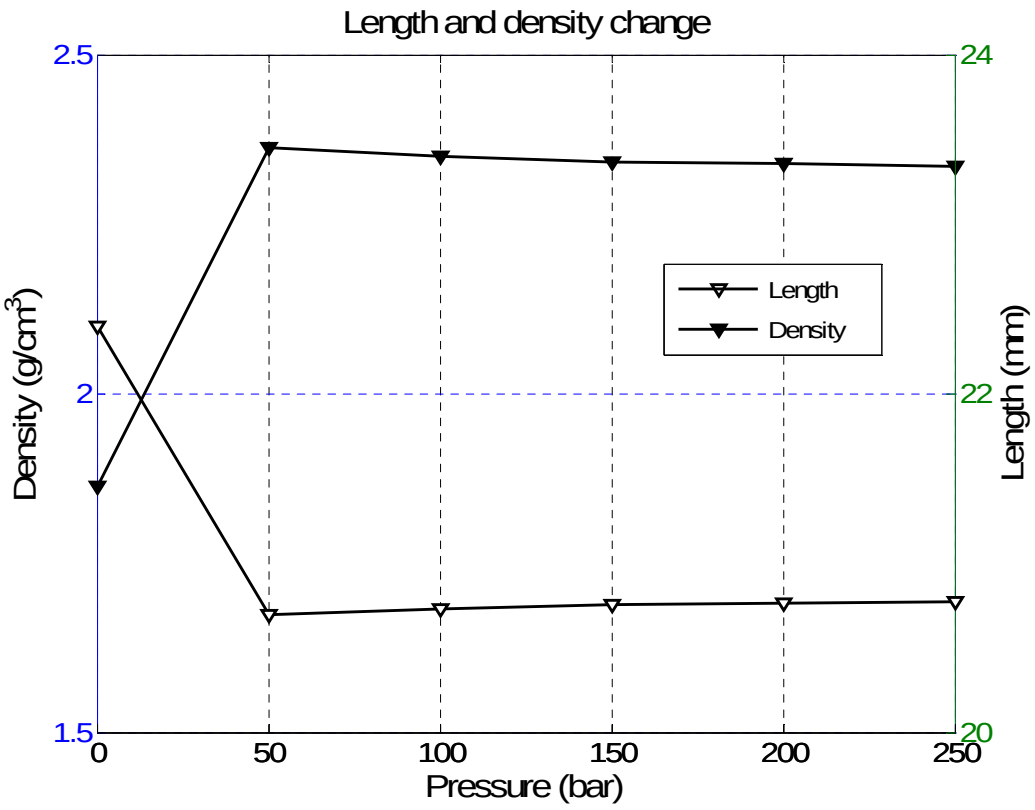

Figure 8.12 Length and density change as pressure drops from 250 bars

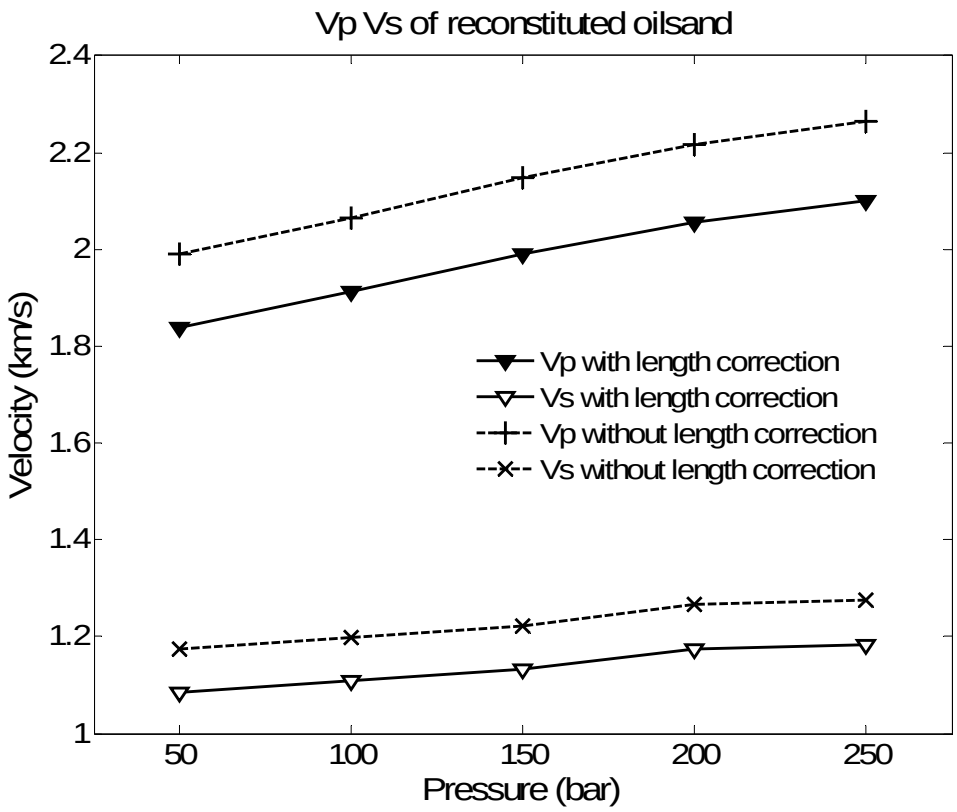

Figure 8.13 P and S wave velocities of reconstituted oil sand calculated with / without length correction

Velocities of oil sand are calculated with and without correction to sample length according to data in Figure 8.10 – 8.12. The results are shown in Figure 8.13. As expected, V_p decreases with decreasing pressure, it ranges from 2.10 km/s at 250 bars to 1.84 km/s at 50 bars. For S wave, the velocity ranges from 1.18 km/s at 250 bars to 1.08km/s at 50 bars. Velocities without length correction is also plotted in dashed lines. It is obvious that the length change reduces the velocity values, therefore, a length reading without monitoring the change will result in greatly exaggerated velocities. The error introduced by ignoring the length change in these highly compressible materials is about 8%.

Chapter 9
Conclusions and Recommendations

9.1 Summary of Work in This Thesis

In this work, a review of deformation behaviors of viscoelastic materials is presented as an opening. The concepts and physical mechanisms of seismic attenuation and dispersion are reviewed thereafter, followed by laboratory techniques and review of measurements. The knowledge gaps in the literature are then summed up in the end of Chapter 2 and are always the concerns throughout the entire thesis.

In order to address these problems, basic theories of elasticity, viscoelasticity and wave propagation are reviewed with an emphasis on commonly ignored bulk viscosity. Viscoelastic models are reviewed in Chapter 3 and are upgraded to dynamic cases with both viscosities incorporated via relaxation theory.

Frequency dependent simulations are made on 5 seismic attenuation models and soon expanded to viscoelastic models with focus on the effects of both shear and bulk viscosities on the P and S wave velocities and attenuation.

The first 5 chapters form the major body of the theoretical work in this thesis, and serve as the source and basis for the experimental part. In the second part of this thesis, from chapters 6 to 8, laboratory protocol, techniques, design and measurements are presented. This part has a direct linkage to recent development of unconventional reservoirs because the highly viscous phases (e.g. heavy oil, bitumen) in such reservoirs hinder the production, thus the properties and characteristics of high viscosity fluids saturated earth materials are increasingly

interesting and necessary.

However, the lab work is done with frustration, because S wave in highly saturated samples is usually not available either in the field or the laboratory. Therefore, preliminary research on how to get S wave signal through an oil sand sample is the major concern on current agenda. As detailed in Chapter 6, with modifications made on buffer material, transducers and most importantly a new apparatus allowing length change detecting, the S wave is available under an advanced rock physics laboratory setting, although signal quality and other issues require further investigation.

Other than the oil sand, two sandstone samples were tested via a conventional technique and apparatus. The results comply with classical mechanisms as a comparison of oil sand's unexpected outcome.

Material characterization of these samples covers microscopic SEM imaging, densities and porosimetry. Calibrations of newly introduced length detecting sensors were performed, which yield satisfactory accuracy. Spectral decomposition was applied to acrylic samples of increasing lengths as a preliminary study of attenuation and dispersion in highly attenuating media. Ultrasonic compressional and shear velocities as functions of confining pressure were calculated for sandstone and oil sand samples with length correction applied to the latter.

The work endeavors to provide preliminary simulation of highly attenuating fluids with focus on its frequency dependency, viscosities induced mechanisms via a relaxation approach. Laboratory advances was also proposed in the length detecting apparatus and other modifications to measurement techniques with which the S wave signal is acquirable to make up the gap in the literature. Future work is still needed to further develop the theoretical model in order to apply to real cases; laboratory development could be facilitated by improving the S wave

quality with modification to the apparatus and also signal processing algorithms.

9.2 Conclusions from Theoretical Simulation

The purpose of simulation is to theoretically illustrate the effects of viscosities on attenuation and dispersion in viscoelastic materials, and it is done on a frequency dependent basis. Therefore, the results may have implications towards the use of ultrasonic laboratory measurements in the interpretation of seismic frequency measurements.

Five commonly used seismic attenuation models proposed in literature fall into a similar pattern. Velocities predicted by such models show a power law increasing trend (Figure 5.2), while attenuation coefficient is almost linear increasing function of frequency, especially at seismic band. The quality factor Q display either a nearly constant or a increasing function of frequency (Figure 5.3). In all 5 cases, Q values are high, mostly above 75 except power law model at low frequency. Further simulation based on Azimi's 2^{nd} law yields dispersed waveforms, the amplitude decay spectra and phase shift as a typical case of solid rocks.

When fluids are involved, attenuation in such materials is simulated with assumption that they are in a state that viscoelasticity theory is applicable. S wave behavior and shear modulus are simulated to illustrate the effects of shear viscosity. Figure 5.7 shows that viscosity is a very important factor that causes intrinsic attenuation in viscoelastic materials. Decreasing viscosity shifts shear modulus, phase velocity and dissipation to lower frequency. These variables remain a constant at viscosity and frequency extremes, while change greatly at intermediate viscosity. Attenuation is surprisingly high at seismic band, this explains why there is almost no shear wave observed in exploration. While at

ultrasonic band, attenuation is low and keeps a constant invariable with frequency.

Regarding P wave behavior in viscoelastic materials, another viscosity is introduced: bulk viscosity. Shown in Figure 5.9 – 5.12 is the bulk viscosity effects simulated by Burger's model. The results show that bulk viscosity has considerable effects on P wave attenuation and dispersion. The order of magnitude of bulk-shear viscosity ratio defines the attenuation / dispersion law. The evolution of V_p and Q_p take on an dual-relaxation pattern, with $\zeta = \eta$ serving as a divider, while $\zeta = 0$ gives traditional single-relaxation relationship. Higher bulk viscosity enhances V_p and Q_p in one relaxation frequency band, while at the rest frequency band, curves merge into a certain limit. At high bulk viscosity, curves merge together at high frequency, while at low bulk viscosity, curves merge at low frequency extreme.

9.3 Conclusions from the Laboratory

Laboratory measurements are done with both traditional approach (on sandstone samples) and a new approach (on an oil sand sample) proposed in Chapter 8.

For sandstone samples, the travel time and velocity have a strong dependency on confining pressure. Increase in pressure will result in a shorter travel time, therefore an increased velocity. While decrease from pressure peak will undo the increased portion in velocity but not completely, which makes the pressure-velocity plot display a hysteresis shape. Short sample yields better results, while long sample's anomalies could be a result from fracture in the middle of the sample or the fracture by pressure.

For oil sand sample, a new protocol is proposed to improve signal quality. This protocol includes lower center frequency transducers, acrylic buffer (end cap) and a length detecting apparatus. S waveforms were obtained with proposed

protocol and apparatus, which proved the feasibility of acquiring S wave signal with pulse through-going technique. P wave velocity decreases with decreasing pressure, which ranges from 2.10 km/s at 25 MPa to 1.84 km/s at 5 MPa. For S wave, the velocity ranges from 1.18 km/s at 25 MPa to 1.08 km/s at 5 MPa.

However, at this stage, signal quality is still an unsettled problem. P waveforms show expected behavior, but S waveforms show discrepancy in amplitude change. This phenomenon is not well understood and further investigation is required.

The attenuation and dispersion in oil sands (and other materials with highly viscous fluid saturation) is an ongoing topic. Because different phases are involved, the fundamental principles and lab measurements need to be adapted. This work focus on frequency dependency and viscosities, particularly bulk viscosity which is ignored in most studies in this field. The aim of building a preliminary framework for both theoretical simulation and laboratory measurements is served, thus future research would be facilitated.

9.4 Recommendations

Based on the simulation and laboratory measurements mentioned above, several improvements could be made in the future:

A more complicated model may be considered, to model multi-phase system in a more realistic manner. One could integrate basic models (with a spectra distribution of relaxation times, Bhatia, 1985) to fit the laboratory measurements. By doing this integration, the adaptability of viscoelastic models could be enhanced, and in this way, the attenuation and dispersion in a more practical circumstance can be interpreted.

A circumference gauge may be necessary in measuring the diameter change

during (de)pressurization. This value is crucial in cases where Poisson's ratio is high. The introduction of this gauge would increase the accuracy in determining the density change as pressure varies.

Length of plastic buffer could be reduced. As a result, more energy would go into the sample instead of absorbed in the buffer. But a minimum length should kept to distinguish signal from RF electromagnetic noise at very short arrivals.

A pre-amplifier is recommended since the maximum load (200volt) of the transducers is still higher than the current applied voltage. This is to improve the signal – noise ratio as low amplitude could be buried in background noise when compaction level is low.

A positioning slot or hook is recommended to ensure the parallelism of the S wave transducers so that transducers could be installed appropriately and at the same time, eliminate potential rotation during (de)pressurization.

Methods should be employed to distinguish external attenuation (such as scattering, spherical spreading, etc) in order to ensure high level of energy transmission. Green and Cooper's paper (1991) could be a starting point.

For oil sand samples, as shown in the SEM, sand grains are wrapped by oils, which makes the homogenous hypothesis no longer valid. In this case, scattering on sand grains may play an important role regarding extrinsic attenuation. For intrinsic attenuation from viscoelastic point of view, a more detailed model in structure is recommended. References can be found on models of viscosity of suspected particles or spheres in Roscoe's paper in 1952 or Sudduth's paper in 1993.

Bibliography

Aki, K., and Richards, P.G., 1980, Quantitative seismology, theory and practice, W.H. Freeman Co.

Azimi, S.A., Kalinin A.V., Kalinin V.V. and Pivovarov B.L., 1968, Impulse and transient characteristics of media with linear and quadratic absorption laws. Izv. Earth Physics, 42-54.

Baechle, H. T., Weger, R. J., and Eberli, G. P., 2005, Changes of shear moduli in carbonage rocks: implications for Gassmann applicability, The leading edge, 507-510.

Barnes, H.A., Hutton, J.F., and Walters, K., 1989, An introduction to rheology, 46-51, Elsevier.

Batzle, M., B. Zadler, R. Hofmann, and D. Han, 2004, Heavy oils-seismic properties, 74th Annual International Meeting, SEG, Expanded Abstracts, 1762–1765.

Beggs, H.D. and Robinson, J.R., 1975, Estimating the viscosity of crude oil systems: Journal of Petroleum Technology, 27, 1140-1141.

Beyer, R.T., and Letcher, S.V, 1969, Physical ultrasonics: Academic Press

Bhatia, A.B., and R. N., Singh, 1986, Mechanics of deformable media: Adam Hilger, Bristol and Boston, University of Sussex Press.

Bhatia, A.B., 1967, Ultrasonic Absorption: Oxford, the Clarendon Press.

Biot, M. A., 1956, Theory of propagation of elastic waves in a fluid-saturated

porous solid: I. Low frequency range: Journal of the Acoustical Society of America, 28, 168-178.

Biot, M. A., 1956, Theory of propagation of elastic waves in a fluid-saturated porous solid: II. higher frequency range: Journal of the Acoustical Society of America, 28, 179-191.

Biot, M. A., 1962, Mechanisms of deformation and acoustic propagation in porous media, Journal of Applied Physics, 33, 1482-1498.

Bourbie, T., Coussy, O., and Zinszner, B., 1987, Acoustics of porous media, Gulf Publishing.

Brakel, V. J., 1981, A Special Issue Devoted to Mercury Porosimetry, Powder Technology, 29, 1-209.

Brennan, B.J., and Stacey, F.D., 1977, Frequency dependence of elasticity of rock – Test of seismic velocity dispersion, Nature, 268, 220-222.

Brodnyan, J. G., Gaskins, F. H., Philippoff, W., and Thelen, E., 1960, The Rheology of asphalt. III. Dynamic mechanical properties of asphalt, Transactions of the Society of Rheology, 4, 279–296.

Browne, M.T., and Pattison, J.R., 1957, The damping effect of surrounding gases on a cylinder in longitudinal oscillations, British Journal of Applied Physics, 8, 452-456.

Burfoot, J.C., 1967, Ferroelectrics: An introduction to the physical principles, D.Van Nostrand Company LTD.

Cady, W.G., 1964, Piezoelectricity: An introduction to the theory and applications

of electromechanical phenomena in crystals, Dover Publications, Inc.

Carcione, J.M., 2006, Energy balance and fundamental relations in dynamic anisotropic poro-viscoelasticity, Proceedings of the Royal Society of London Series, (A-Mathematical Physical and Engineering Sciences), 457, 331-348.

Carlson R. L., and Gangi, A. F., 1985, Effects of cracks on the pressure dependence of P wave velocities in crystalline rocks: Journal of Geophysical Research, 90, 8675-8684.

Christensen, R.M., 1982, Theory of viscoelasticity: An introduction, Academic Press.

Cole, K.S., and Cole, R.H., 1941, Dispersion and absorption in dielectrics: I. Alternating current characteristics. Journal of Chemical Physics, 9, 342-351.

Creaser, R. A., Sannigrahi, P., Chacko, T., and Selby, D., 2002, Further evaluation of the Re-Os geochronometer in organic-rich sedimentary rocks: A test of hydrocarbon maturation effects in the Exshaw Formation, Western Canada Sedimentary Basin, Geochimica Et Cosmochimica Acta, 66, 3441-3452.

Dickinson, E. J. and Witt, H. P., 1974, The dynamic shear modulus of paving asphalts as a function of frequency, Transactions of the Society of Rheology, 18, 591–606.

Dvorkin, J., Mavko, G. and Nur, A., 1995, Squirt flow in fully saturated rocks: Geophysics, 60, 97-107. Gassmann, F., 1951, Uber die elastizitat poroser medien: Verteljahrsscrift der Naturforschenden Gesellschaft in Zurich, 96, 1-23.

Ferry, J.D., 1980, Viscoelastic properties of polymers, John Wiley & Sons, Inc.

Futterman, W.I., 1962, Dispersive body waves, Journal of Geophysical Research, 67, 5279-5291.

Gassmann, F., 1951, Elasticity of porous media: Uber die Elastizitat poroser Medien:Vierteljahrsschrift der Naturforschenden Gesselschaft in Zurich, 96, 1-23.

Green, D. H., Cooper, R.F., and Zhang S. 1990, Shear wave diffraction loss for circular plane-polarized source and receiver, Geophysical. Research. Letters，17, 12 2097-2100.

Green, D. H., and Wang, H.F., 1991, Shear wave diffraction loss for circular plane-polarized source and receiver, Journal of Acoustical Society of America, 90(5), 2696-2704.

Green, D.H., Wang, H.F. and Bonner, B.P., 1993, Shear wave attenuation in dry and saturated sandstone at seismic to ultrasonic frequencies, Journal of rock mechanics and mining sciences & geomechanics abstracts, 30, 7, 755-761.

Greenwood, M. S. and Bamberger, J. A., 2002, Measurement of viscosity and shear wave velocity of a liquid or slurry for on-line process control, Ultrasonics, 39, 623-630.

Griggs, D.T., Turner, F.J., and Heard, H.C., 1960, Deformation of rocks at 500 degrees and 800 degrees C, Rock Deformation, Geological Society of America Memoir, 79, 39-104.

Griggs, D.T., 1954, Deformation of rocks at 500 degree C, 5000 atmospheres pressure, Geological Society of America bulletin, 65,12, 1258-1258.

Gurin, M.E., and Herrera, I., 1965, On dissipation inequalities and linear viscoelasticity, Quarterly of applied Mathematics, 23, 3, 235.

Han, D-H., Liu, J., and Batzle, M., Measurement of shear wave velocity of heavy oil, Society of Exploration Geophysicists Conference, Expanded abstract, 2005, 1-4.

He, T., 2006, P- and S-wave velocity measurement and pressure sensitivity analysis of AVA response, Master of Science thesis, University of Alberta.

Herzfeld, K.F., and Litovitz, T.A., 1959, Absorption and dispersion of ultrasonic waves: Academic Press.

Hsu, T.R., Gong, Z.L., Sun, N.S., and Chen, G.G., 1988, A technique for the measurement of mechanical damping characteristics of oil sands, AOSTRA Journal of research, 4, 95.

Jackson, D.D., 1969, Grain boundary relaxations and the attenuation of seismic waves, Ph.D thesis, M.I.T.

Jones, T. D., 1986, Pore Fluids and Frequency-Dependent Wave-Propagation in Rocks, Geophysics, 51, 1939-1953.

Khaksar, A., Griffiths, C. M., and McCann C., 1999, Compressional- and shear-wave velocities as a function of confining stress in dry sandstones: Geophysical Prospecting, 47, 487-508.

Kingery, W.D., 1959, Property measurements at high temperature, New York, Wiley.

Kolsky, H., 1953, Stress waves in solids, Oxford University Press.

Kolsky, H., 1956, The propagation of stress pulses in viscoelastic solids, Philosophical Magazine, 1, 693-710.

Kramers, H.A., La 1956, diffusion de la lumi`ere par les atomes, Collected Scientific Papers. Amsterdam: North-Holland, (in French).

Krönig, R. de Laer, 1926, On the theory of dispersion of x-rays, Journal of the optical Society of America., 12, 547–557.

Kundu, K.P., and Cohen, I., 2001, Fluid Mechanics, Elsevier Academic Press.

Kundu, K.P., 1990, Fluid Mechanics, Academic Press.

Lay, T., and Wallace, T.C., 1995, Modern global seismology, Academic Press Inc.

Lesueur, D., Gerard, J.F., Claudy, P., Letoffe, J.M., Planche, J. P., and Martin, D., 1996, A structure-related model to describe asphalt linear viscoelasticity, Journal of Rheology, 40, 5, 813-836.

Liggett, J.A., 1994, Fluid Mechanics, McGraw-Hill Inc.

Lines, L. R. and Daley, P. F., 2007, Seismic detection of cold production footprints in heavy oil extraction, Journal of Seismic Exploration, 15, 333-344.

Lines, L. R., Zou, Y., Zhang, A., Hall, K., Embleton, J., Palmiere, B., Reine, C., Bessette, P., Cary, P., and Secord, D., 2005, V_P/V_S characterization of a heavy-oil reservoir, The Leading Edge, 24, 1134-1136.

Llewellin, E.W., Mader, H.M., and Wilson, D.R., 2002, The rheology of a bubbly liquid, Proceedings of the Royal Society London A,, 458, 987-1016

Malvern, L. E., 1969, Introduction to the Mechanics of a Continuous Medium. Prentice Hall, Englewood Cliffs, NJ.

Mavko, G.M., 1980, Velocity and attenuation in partially molten rocks, Journal of geophysical research, 85, 5173-5189.

Mavko and Nur, 1979, Wave attenuation in partially saturated rocks, Geophysics, 44, 161-178.

Mavko, G.M., 1979, Frictional attenuation: An inherent amplitude dependence, Journal of Geophysical Research, 84, 4769-4776.

Molyneux, J.B., and Schmitt, D.R., 2000, Compressional-wave velocity in attenuating media: a laboratory physical model study, Geophysics, 65, 4, 1162-1167

Molyneux, J. B., and Schmitt, D. R., 1999, First break timing: Arrival onset times by direct correlation: Geophysics, 64, 1492-1501.

Nguyen, N.T., Lethiecq, M., Karlsson, B., and Patat, F., 1996, Highly attenuative rubber modified epoxy for ultrasonic transducer backing applications, Ultrasonics, 34, 669-675.

Nicholas, M. E., Joyner, P. A., Tessem, B. M., and Olson, M. D., 1961, The effect of various gases and vapors on the surface tension of mercury: Journal of Physical Chemistry, 65(8), 1373-1375.

Nicolas, A., 1986, Principles of rock deformation, D.Reidel Publishing Company.

Nussenzveig, H.M., 1972, Causality and dispersion relations (Mathematics in science and engineering Vol.95), series editor, Academic Press, New York.

O'Connell, R. J., and Budiansky, B., 1978, Measures of dissipation in viscoelasti media, Geophysics Review Letters, 5, 5-8.

Pelselnick. L., Liu, H.P., and Harper, K.R., 1979, Observations of details of hysteresis loops in Westerly granite, Geophysical Research Letters, 6, 693-696.

Peselnick, L., and Zietz, I., 1959, Internal friction of fine grained limestones at ultrasonic frequencies, Geophysics, 24, 285-296.

Piccirelli, R and Litovitz T.A. ,1957, Ultrasonic shear and compressional relaxation in liquid glycerol, Journal of Acoustical Society of America, 29, 9, 1009-1018.

Ranalli, G., 1987, Rheology of the earth, Allen & Unwin Inc.

Rosato, D.V., and DiMattia, D.P., 1991, *Designing with plastics and composites,* New York: Van Nostrand Reinhold.

Roscoe, R., 1952, The viscosity of suspensions of rigid spheres, British Journal of Applied Physics. 3, 267–269 .

Schreiber, E., Anderson, O.L., and Soga, N., 1973, Elastic constants and their measurement, McGraw-Hill Book Co., Inc., New York.

Spetzler, H., and Anderson, D.L., 1968, The effect of temperature and partial melting on velocity and attenuation in a simple binary system, Journal of Geophysical Research, 73, 6051-6060.

Spinner, S., and Tefft, W.E., 1961, Method for determining mechanical resonance frequencies and for calculating elastic moduli from these frequencies, American society for testing and materials, 61, 1221-1238.

Standard test method for laboratory determination of pulse velocities and ultrasonic elastic constants of rock, ASTM standard, D2845.

Stein, S., and Wysession, M., 2003, An introduction to seismology, earthquakes, and earth structure, Blackwell Pub.

Strick，E., 1967. The determination of Q, dynamic viscosity and transient creep curves from wave propagation measurements, Geophysical Journal of the Royal Astronomical Society, 13, 197-218.

Sudduth, R. D., 1993, A generalized model to predict the viscosity of solutions with suspended particles. I., Journal of Applied Polymer Society, 48, 25–36 .

Tittmann, B.R., Clark, V.A., Richardson, J., and Spencer, T.W., 1980, Possible mechamism for seismic attenuation in rocks containing small amounts of volatiles, Journal of Geophysical Research, 85, 5199-5208.

Tompkins, M.J., and Christensen, N.I., 2001, Ultrasonic P- and S- wave attenuation in oceanic basalt, Geophysical Journal International, 145, 172-186.

Toksoz, M.N., Johnston, D.H., and Timur, A., 1979, Attenuation of seismic waves in dry and saturated rocks: I. Laboratory measurements, Society of Exploration Geophysics, 44, 681-690.

Tressler, J. F., Alkoy, S., and Newnham, R. E., 1998, Piezoelectric Sensors and Sensor Materials, Journal of Electroceramics, 2:4, 257-272,

Truell, R., Elbaum, C., and Chick, B., 1969, Ultrasonic methods in solid state physics, Academic Press.

Trusler, J. P. M., 1991, Physical Acoustics and Metrology of Fluids: Adam Hilger, Bristol, Philadelphia and New York.

Ursin, B., and Toverud, T., 2002, Comparison of seismic dispersion of and attenuation models, Stud. Geophys. Geod., 46, 293-320.

Viyanant, C., Rathje, E.M., and Rauch, A.F., 2007, Creep of compacted recycled asphalt pavement, Canadian Geotechnical Journal, 44, 687-697.

VonKarman, T., the propagation of plastic deformation in solids, 1950, Journal of applied physics, 21, 10, 987-994.

Walsh, J.B., 1966, Seismic wave attenuation in rock due to friction, Journal of geophysical research, 71 (10), 2591-2604.

Walsh, J.B., 1968, Attenuation in partially melted material, Journal of geophysical research, 73(6), 2209-2218.

Walsh, J.B., 1968, New analysis of attenuation in partially melted rock, Journal of geophysical research, 74(17), 4333-4340.

Washburn, E. W., 1921, Note on a method of determining the distribution of pore sizes in a porous material, Proceedings of the National Academy of Science, 7, 115-116.

Wang, Z., Nur, A.M., and Batzle, M.L., 1990, Acoustic velocities in petroleum oils, Journal of Petroleum Technology, 192-200

Wang, Y. H., and Guo, J., 2004, Modified Kolsky model for seismic attenuation and dispersion, Journal of Geophysics and Engineering, vol. 1, pp. 187-196.

Wang, Z., and Nur. A., Seismic and acoustic velocities in reservoir rocks: Theoretical and model studies, Society of Exploration Geophysics, 2, 1-35.

Waters, K. R., and Hoffmeister, B. K., 2005, Kramers-Kronig analysis of attenuation and dispersion in trabecular bone, Journal of the Acoustical Society of America, 118, 3912-3920.

Webb, S., 1997, Silicate melts: relaxation, rheology, and the glass transition, Reviews of Geophysics, 35, 191-218.

White, J.E., 1975, Computed seismic speeds and attenuation in rocks with partial gas saturation, Geophysics, 40, 224-232.

White, J.E., 1965, Seismic waves: Radiation, transmission and attenuation, McGraw-Hill Book Co., Inc.

Winkler, K.W., and Plona, T.J., 1982, Technique for measuring ultrasonic velocity and attenuation spectra in rocks under pressure, Journal of geographical research, 87, B13, 10776-10780.

Winkler K. W., 1986, Estimates of velocity dispersion between seismic and ultrasonic frequencies: Geophysics, 51, 183-189.

Winkler, K., Nur, A., and Gladwin, M., 1979, Friction and seismic attenuation in rocks, Nature, 227, 528-531.

Wolf, K., Mukerji, T., and Mavko, G., 2001, Attenuation and Velocity Dispersion Modeling of Bitumen Saturated Sand, Stanford Rock Physics Laboratory,

SEG/New Orleans 2006 Annual Meeting

Wong, R. C. K. and Maini, B. B., 2007, Gas bubble growth in heavy oil-filled sand packs under undrained unloading, Journal of Petroleum Science and Engineering, 55, 259-270.

Wood, A.B., 1946, A textbook of sound : being an account of the physics of vibrations with special reference to recent theoretical and technical developments, G. Bell and Sons.

Wuenschel, P.C., 1965, Dispersive body waves - An experimental study, Geophysics, 30, 539-551.

Wyllie, M. R. J., Gregory, A. R., and Gardner, G. H. F., 1958, An experimental investigation of factors affecting elastic wave velocities in porous media: Geophysics, 23, 459-493.

Yin, H., 1993, Acoustic velocity and attenuation of rocks, isotropy, intrinsic anisotropy, and stress-induced anisotropy: Ph.D. Thesis, Stanford Univ.

Zhang, Y., and Guo, G, 2000, Molecular dynamics calculation of the bulk viscosity of liquid iron–nickel alloy and the mechanisms for the bulk attenuation of seismic waves in the Earth's outer core, Physics of The Earth and Planetary Interiors, 122, 289-298

Zener, C., 1948, Theory of strain interaction of solute atoms, 1948, Physics Review, 74, 6, 639-647.

Zimmer, M. A., 2003, Seismic velocities in unconsolidated sands: measurements of pressure, sorting, and compaction effects, Ph.D dissertation, Stanford University

Appendix 1:
Mercury Porosimetry of Sample R010

Pressure (MPa)	Incremental Intrusion (mL/g)	Cumulative Intrusion (mL/g)
0.00351958	0	-2.38E-08
0.0137083	0.00427111	0.00427108
0.0206053	0.000706908	0.00497799
0.0274694	0.000632484	0.00561047
0.0377668	0.000915232	0.00652571
0.0412409	0.000245546	0.00677125
0.0515466	0.000587851	0.0073591
0.0584254	0.000334835	0.00769394
0.0721233	0.000840826	0.00853476
0.0893343	0.00119055	0.00972531
0.11012	0.00215044	0.0118758
0.137618	0.004911	0.0167868
0.172028	0.0140635	0.0308503
0.206581	0.0228212	0.0536715
0.261053	0.0203955	0.074067
0.322229	0.0121599	0.0862269
0.39572	0.00793624	0.0941632
0.49913	0.00666899	0.100832
0.598516	0.00419198	0.105024
0.777201	0.00494246	0.109967
0.950913	0.00346421	0.113431
1.19536	0.00344953	0.11688
1.49633	0.00320938	0.12009
1.85248	0.00268375	0.122773
2.25019	0.00252281	0.125296
2.87601	0.00289586	0.128192
3.56444	0.00292546	0.131118
4.39922	0.00228004	0.133398

Pressure (MPa)	Incremental Intrusion (mL/g)	Cumulative Intrusion (mL/g)
5.49061	0.00228558	0.135683
6.79957	0.00211966	0.137803
8.2677	0.0018833	0.139686
10.3277	0.00214013	0.141826
13.0706	0.00178124	0.143608
16.1834	0.000834598	0.144442
19.9636	0.000414171	0.144856
24.7869	0.000125425	0.144982
30.934	6.13E-05	0.145043
38.5049	-3.03E-09	0.145043
47.4551	-3.03E-09	0.145043
59.179	-3.03E-09	0.145043
72.949	-3.03E-09	0.145043
90.8649	-3.03E-09	0.145043
101.886	-3.03E-09	0.145043
112.906	-3.03E-09	0.145043
137.68	-3.03E-09	0.145043
172.301	-3.03E-09	0.145043
206.733	-3.03E-09	0.145043
240.988	-3.03E-09	0.145043
275.377	-3.03E-09	0.145043
309.829	-3.03E-09	0.145043
344.269	-3.03E-09	0.145043
378.733	-3.03E-09	0.145043
413.2	-3.03E-09	0.145043

Appendix 2
Grain Density Measurements of Oil Sand

Sample	p_1	p_2	V_c (cm^3)	V_r (cm^3)	V_p (cm^3)	m_c (g)	m_s (g)	ρ_g (g/cm^3)
Oil sand	17.024	5.575	28.825	11.588	5.028	4.86	14.87	1.99
(reconstituted)	17.052	5.578	28.825	11.588	4.988	4.86	14.87	2.01
Oil sand	17.095	5.262	28.825	11.588	2.766	4.86	11.2	2.29
(original)	17.025	5.238	28.825	11.588	2.749	4.86	11.2	2.31
	17.323	5.329	28.825	11.588	2.744	4.86	11.2	2.31

Comments:

1. The oil sand samples were taken from cores obtained during drilling of the Bakken formation of west-central Saskatchewan.
2. Grain density was measured on a Multipycnometer by Quantchrome Instruments, model # MVP-D160-E.
3. The formulas to calculate grain density are:

$$V_p = V_c - V_r(p_1 / p_2 - 1)$$
$$\rho_g = (m_s - m_c)/V_p$$

4. 3 Measurements were made on each sample, with one failed on reconstituted oil sand.